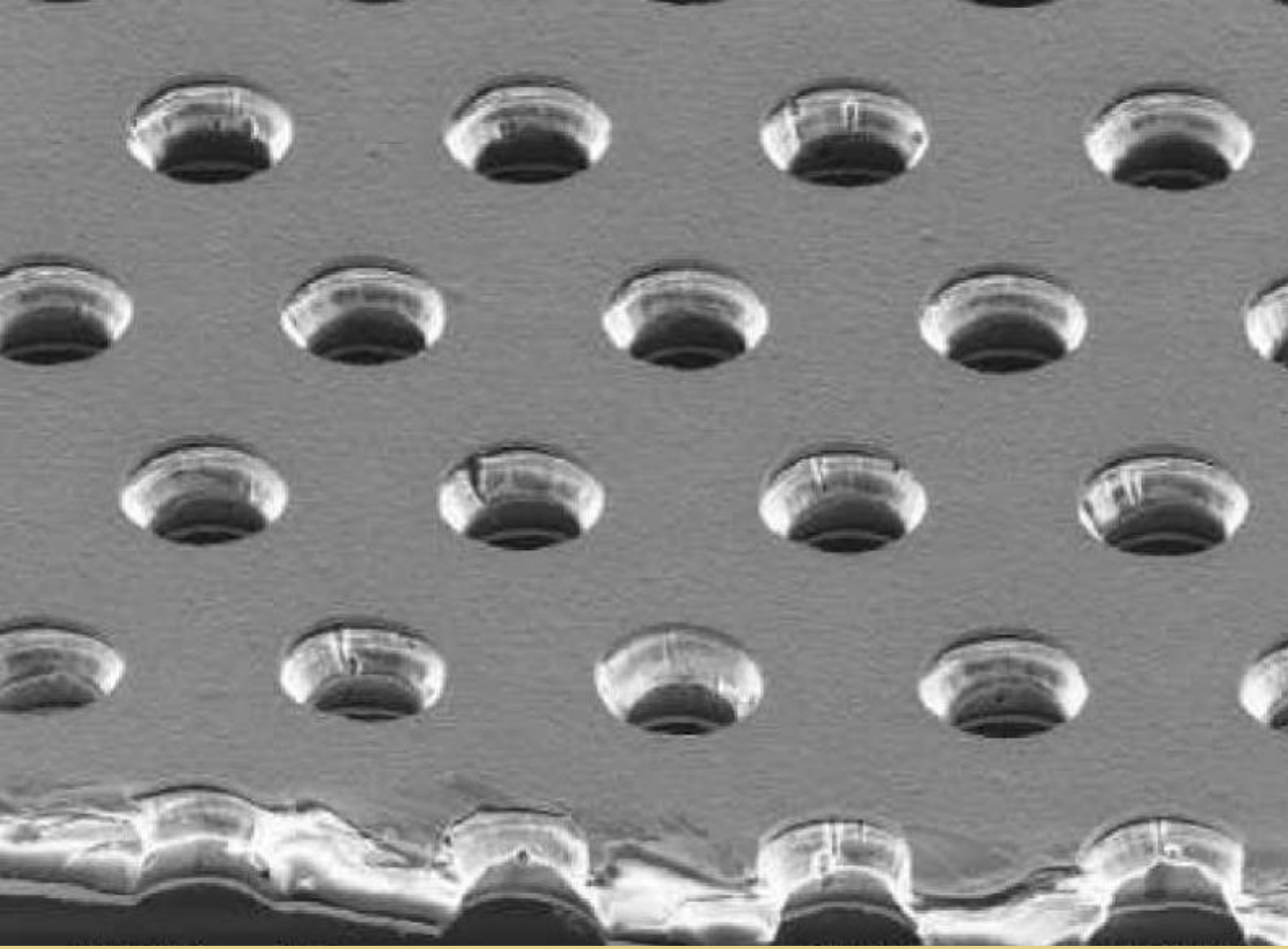

Vítor Xavier Pereira Carvalho

Large Area Cascaded Gas Electron Multipliers for Imaging Applications

Tese de mestrado em Física
Setembro de 2015

· U C ·

Universidade de Coimbra

Vítor Xavier Pereira Carvalho

Large Area Cascaded Gas Electron Multipliers for Imaging Applications

Dissertation submitted to
Faculdade de Ciências e Tecnologia da Universidade de Coimbra
for the Master's degree in Physics

under the supervision of

Dr. Fernando Domingues Amaro and Dr. Luís Fernandes

UNIVERSIDADE DE COIMBRA

Acknowledgements

Depois de três anos de investigação são imensos os agradecimentos a fazer a todos aqueles que de algum modo contribuíram para o sucesso do meu mestrado.

Gostaria de agradecer em primeiro lugar ao meu orientador Dr. Fernando Amaro e ao Dr. Hugo Natal da Luz pela enorme orientação, dedicação e amizade que demonstraram ao longo deste trabalho. Obrigado pela força e por todas as sugestões e conhecimento que partilharam comigo.

Ao Dr. Joaquim dos Santos por me ter acolhido no seu laboratório e me dar a oportunidade e os meios para avançar com a investigação que deu origem a esta tese de mestrado. Obrigado pelo apoio, confiança e conhecimento ao longo destes três anos.

Ao meu co-orientador, Dr. Luís Fernandes, pela revisão da tese.

A todos os colegas do Grupo de Instrumentação Atómica e Nuclear pela calorosa recepção e por fazerem do laboratório uma segunda casa. Um agradecimento especial à Cristina Monteiro, Elisabete Freitas, Emanuel Barata, Carlos Henriques, Paulo Gomes e Marcos Ball.

To Dr. Jamil Mir by the review of this thesis.

Aos meus amigos Daniel Mano, Pedro Borlido e Marina Jorge por me acompanharem desde sempre nesta luta que foi a licenciatura Física e posterior mestrado. Sem eles a estadia em Coimbra e a concretização desta tese não teria sido a mesma coisa.

Aos meus amigos de sempre, André, Amadeu, Tiago, Ricardo, Carlos, Iolanda e Patrícia pela enorme amizade, carinho, por me animarem nos tempos mais difíceis e por acreditarem sempre em mim, por vezes até mais que eu.

Aos meus pais e avós por todo o esforço que fizeram para que este momento se concretizasse.

E um especial agradecimento à minha irmã Sofia pelo carinho e disponibilidade, por acreditar em mim e estar sempre presente, nos melhores e piores momentos, ao longo da minha vida.

Abstract

In this work a simple X-ray imaging system using off-the-shelf electronics and simple reconstruction algorithms is described. Aiming this, two $100\ cm^2$ Gas Electron Multiplier (GEM) foils with a thickness of $100\ \mu m$ were used. These micropattern gaseous structures were immersed in a mixture of argon and carbon dioxide in a ratio of 70:30. Due to their thickness, these robust GEM foils were found to be more resistant to electric discharges when compared to standard GEMs.

The 2D imaging capability of the detector is explored using for that the resistive charge division method. Two different readouts are used in this work: one with an area of $50\ \times 50\ mm^2$ and other one with $100\ \times 100\ mm^2$.

The performance of the detector as an imaging detector is also characterized. X-ray images are shown and some descriptions of the physical processes involved are presented. The method used allowed counting each X-ray photon detected and yielding information about its interaction position and energy. Position resolutions below 2 mm were achieved with very good cost effectiveness. The detector is suitable to use in some X-ray imaging applications and may find an application as a proton beam monitor.

Resumo

Neste trabalho é descrito um sistema simples de imagem de raio-X que usa electrónica de uso comum e algoritmos de reconstrução simples. Para o efeito, foram usados dois GEMs (Gas Electron Multiplier) em cascata de $100\,cm^2$ e com uma espessura de $100\,\mu m$. Estas micro estruturas foram imersas numa mistura de árgon e dióxido de carbono num rácio de 70:30. Devido à sua espessura, estes GEMs robustos mostraram ser mais resistentes a descargas eléctricas comparativamente aos GEMs com espessura de $50\,\mu m$..

Foram utilizados dois eléctrodos de recolha de carga distintos: um com uma área de $50\,\times 50\,mm^2$ e outro com uma área de $100\,\times 100\,mm^2$.

O desempenho do detetor como sistema de imagem é também caracterizado. Deste modo, são apresentadas imagens adquiridas com raios-X que permite caracterizar a resposta do detector, bem como algumas descrições dos processos físicos envolvidos. O método utilizado permite a contagem de cada fotão de raio-X detectado e fornece informação acerca da posição onde se deu a interacção bem como da energia do fotão incidente. Foram conseguidas resoluções de posição inferiores a 2 mm compatíveis com o que é esperado com este tipo de gás, mostrando que este tipo de detector é uma boa opção em aplicações onde seja necessária uma resolução em energia razoável e uma resolução em posição da ordem dos mm.

Publicações no âmbito desta Tese de Mestrado

Poster Presentations:

“X-ray Imaging with GEM using 100 micro Thick Foils”, 15th iWoRiD International Workshop on Radiation Imaging Detectors, June 2013 Paris, France.

“Gain Characteristics of a 100 micro thick Gas Electron Multiplier (GEM)”, 17th iWoRiD International Workshop on Radiation Imaging Detectors, June/July 2015 DESY Hamburg, Germany.

"A robust large area X-ray imaging system based on 100 μm thick Gas Electron Multiplier (GEM)", 17th iWoRiD International Workshop on Radiation Imaging Detectors, June/July 2015 DESY Hamburg, Germany.

"A robust large area X-ray imaging system based on 100 μm thick Gas Electron Multiplier (GEM)", XIII Iberian Joint Meeting on Atomic and Molecular Physics (IBER2015), September 2015, Aveiro-Portugal.

In International Journals with Peer-Review

"Gain Characteristics of a 100 μm thick Gas Electron Multiplier (GEM)", J.A. Mir, H. Natal da Luz , X. Carvalho, C. D.R. Azevedo, J.M.F. dos Santos, F. D. Amaro, in preparation, to be submitted to JINST.

"A robust large area X-ray imaging system based on 100 μm thick Gas Electron Multiplier", F. D. Amaro, J.A. Mir, H. Natal da Luz , X. Carvalho, C. D.R. Azevedo, J.M.F. dos Santos, in preparation, to be submitted to JINST.

“X-ray imaging with GEMs using thick foils”, H. Natal da Luz, J. A. Mir, X. Carvalho and J.M.F. dos Santos.. Journal of Instrumentation, Volume 9, C06007, JUN 2014.

List of abbreviations

2D	Two-dimensional
3D	Three-dimensional
D-GEM	Double GEM
ESF	Edge spread function
FT	Fourier transform
FWHM	Full width at half maximum
GEM	Gas electron multiplier
GEM-MIGAS	Micro-induction gap amplifying structure
GIAN	Atomic and nuclear instrumentation group
GPSC	Gas proportional scintillation counter
HV	High voltage
LSF	Line spread function
MCA	Multichannel analyser
MPGD	Micropattern gaseous detector
MSGC	Microstrip gas counter
MTF	Modulation transfer function
MWPC	Multiwire proportional chamber
PCB	Printed circuit board
PMT	Photomultiplier tube
PSF	Point spread function
S-GEM	Single GEM
SNR	Signal-to-noise ratio
THGEM	Thick gas electron multiplier

Table of Contents

1. Introduction

The use of gas counters for radiation detection was introduced by Geiger in 1908. The classic gas counters were constituted basically by two electrodes where a potential difference is applied. The interaction of the ionizing radiation with the gas leads to the production of electron-ion pairs which drift in different directions due to the influence of the electric field. The charge flow induces a charge pulse that can be measured through appropriate electronics.

Over the following years a lot of effort was put in the development of gas detectors in order to supress some limitations and to improve their imaging capabilities. One big step in that direction was taken by Charpak in 1968 with the invention of the Multiwire Proportional Chamber. Despite their delicate and complex constructing procedure, they remain very appealing in large experiments and the era of the MWPCs lasted very long. In order to cope with the challenges foreseen for the new large Physics experiments, in the end of the eighties another breakthrough in the technology of gaseous detectors took place. The so-called Micropattern Gaseous Detectors (MPGD), fabricated with high precision microelectronic circuit board printing techniques, which allow etching much finer structures in polymeric substrata were introduced. In the end of the nineties the MICROMEGAS and the GEM were introduced by Geomataris and Sauli, respectively. These detectors will be described in detail in chapter 2.

The first detector that fits this category was the Gaseous Micro-Strip Detector, invented by Oed, consisting of an array of thin strips alternated with larger strips.

Since the microstructures are very reliable, they have undergone an impressive development over the past few years and are nowadays used in many experiments. High-energy physics experiments, astrophysics, neutron and proton detection and medical imaging are some examples of the MPGD applications.

Actually, the imaging capabilities of MPGDs have been well documented for GEMs [1] and Micro-Hole and Strip Plates [2] and other micropattern structures, using resistive charge division, delay lines or discrete electronics. The Gas Electron Multiplier (GEM) is the microstructure used in this work and has been successfully applied in Particle Physics among other fields. An example of GEM application is the Common Muon and Proton Apparatus for Structure and Spectroscopy (COM-PASS) experiment. This experiment held at CERN aimed to study the hadron structure and hadron

spectroscopy with high intensity muon and hadron beams. The CMS and ALICE experiments in the LHC are also undergoing upgrades for using GEMs in the Muon System and the Time Projection Chamber, respectively.

A standard GEM configuration consists of $50\ \mu m$ Kapton™ thick foil which is copper clad on both sides. The structure is perforated with a matrix of holes that typically have a diameter of $70\ \mu m$ in a $140\ \mu m$ hexagonal pitch. By applying a proper electrical field across the holes, due to the high field inside, it is possible to multiply electrons from a primary ionization cloud. This charge multiplication produces a charge signal proportional to the energy deposited in the detector by the ionizing radiation. The GEM can be operated in single mode or can be cascaded with a second or third GEM until a satisfactory signal-to-noise ratio (SNR) is achieved. Several GEMs configuration allows higher gain performances. In this dissertation a double configuration was used with a non-standard GEM made from a $100\ \mu m$ Kapton™ thick foil immersed in a mixture of Argon (70%) and carbon dioxide (30 %). Due to its two dimensional geometry, this microstructure exhibit a good solution whenever there are demands of large detection areas, such as the cases of particle beam monitors, large position sensitive detectors for X-rays and others.

Most of the imaging applications with MPGDs have made use of discrete channel readouts which allow obtaining very good spatial resolutions (order of hundreds of microns) for areas as large as $100\ cm^2$. However, a large drawback of these readouts is the fact that it requires a large number of channels, which implies an increased complexity of the electronic system. Another method can be used whenever a spatial resolution of the order of mm is required. The resistive charge division compares the amplitude of the signals at both ends of a resistive chain, determining the center of mass of the charge collected. The main advantage of this method is the reduction of the required electronics, because it only requires four amplification and shaping channels. However, this alternative is highly dependent on a good signal-to-noise ratio, which means that the GEMs have to operate at the highest gains possible, eventually too close to the spark limit. The unavoidable consequence of operating near to this limit is the increased probability of discharges that may result in permanent detector damage. The use of robust non-standard GEMs that are two-fold thicker than the standard ones, help to bypass this consequence since a higher discharge power is needed to cause a short circuit across the holes of the GEM.

The experiments described in this thesis were made aiming proton detection. However, since a proton source is not available in the laboratory, an X-ray source was used to produce the primary electron cloud. The X-ray tube and radioactive sources such as the ^{55}Fe are more practical to use and control in a laboratory. The main objective of this dissertation is to study the characteristics of the Gas Electron Multiplier (GEM) structures and to develop and investigate a detector, based on these microstructures, capable of working as imaging devices. The intrinsic 2D imaging capability of the detector allows one to obtain the position of each X-ray photon detected together with its energy. This thesis is divided in 5 chapters.

Chapter 1 is concerned with the introduction of the gaseous detectors and a brief historical account is given to highlight their evolution into micropattern arena.

Chapter 2 introduces the main aspects necessary to understand the physics behind the detectors and the experiments carried out in this work. In the first section, a brief summary of the more pertinent interactions of radiation with matter is given. The knowledge of these interactions is the first step to embrace the subject of particle detection and the instrumentation needed to accomplish it. The second section is a brief historical review of gaseous detectors, focusing on the main research work carried out since the Geiger-Müller counter until the Micropattern gaseous detectors invention. Most of the gaseous proportional detectors mentioned in this section are enriched with references of other research work carried out by others groups. The *second chapter* works as the state-of-the-art of this dissertation.

In chapter 3 the experimental setup is described. The detector setup as well as the imaging system setup is fully characterized. The first section focuses on describing the mechanical elements of the detector, from the support frame containing the GEMs to the X-ray tube. A detailed description of all the elements and instruments used is given. In the following section the electronic calibration is described. The charge calibration setup and the equations involved are referenced. The characterization of the imaging system setup was left for the third and last section. Here, some basic concepts to take in account in an imaging system based on resistive charge division and the limitations in the spatial resolution are described.

The experimental results and the first 2D images are shown in *chapter 4*. The performance of the detector, concerning charge gain and energy resolution, was investigated for an $Ar{:}\,CO_2$ $(70{:}\,30\,\%)$ gas mixture. The results are compared to the literature. Two different charge readouts were used: one with an area of $50 \times 50\ mm^2$

and other one with $100 \times 100\, mm^2$. The optimization of the drift, transfer and induction fields was made for both readouts. A gain and energy resolution map is presented. In the last section a comparison between the results obtained by the two different readouts is made.

In the conclusions, *chapter 5*, the main results achieved with this thesis are presented.

2. Gaseous detectors for ionising radiation

This chapter covers the basic reactions that occur when radiation interacts with matter and the effects produced by these processes. The knowledge of these processes is of main importance for experimental nuclear physicists. As it will be seen, these reactions and their consequences are the basis of all current particle detection devices. The evolution of gaseous detectors, from the discovery of the *Townsend* avalanche in 1901 until the development of *micropattern gaseous detectors* in late nineties, is also covered.

2.1. **Interaction of radiation with matter**

The operation of any radiation detector depends mostly on the manner in which the radiation to be detected interacts with the material of the detector itself.

The knowledge of the mechanisms by which radiation interacts and loses energy is essential on the gaseous detector field. Those interactions depend on the type of particle and on the gas mixtures. Therefore the first aspect to be taken into account when designing an ionising radiation detector is the kind of particles to detect. In this work, we are interested in the concept of proton beam imaging. But, since a proton beam is not available in our lab, X-rays were used as a source to produce the primary electron cloud. Regarding the particles involved in X-ray detection, it is imperative to understand how photons, electrons and heavy charged particles interact with matter.

The radiation can be classified as ionising and non-ionising radiation. The latter refers to electromagnetic radiation that does not have enough energy to remove an electron from an atom or molecule (ionization). Then, instead of producing charged particles when passing through the matter, the electromagnetic radiation has only sufficient energy to shift an outer electron to a higher energy state (excitation) or not to interact at all if the energy is not high enough. The ionizing radiation consists of highly-

energetic particles which have enough energy to remove one or more electrons from an atom or molecule.

The interaction of ionising radiation with matter is a complex subject which cannot be fully described in this thesis. Only the interactions required to understand the current work will be addressed.

2.1.1. X-Rays

Röntgen's studies in the late nineteenth and early twentieth centuries quickly established the penetrating nature of X-Rays [3]. Their potential for medical imaging was soon realized. X-rays are photons typically produced by atomic de-excitations.

In the Standard Model of particle physics, a photon is considered a fundamental particle that represents one quantum of electromagnetic energy. In that model the photon is assumed to have no rest mass. The relationship between the photon energy, E, and its frequency, υ, is given by:

$$E = h\upsilon \tag{2.1}$$

where h is the Planck constant.

There are two main types of energy transfer that may occur when X-rays interact with matter:

- Ionization, in which the incoming radiation causes the removal of an electron from an atom or molecule leaving the material with a net positive charge.
- Excitation, in which some of the X-ray's energy is transferred to the target material leaving it in an excited state.

The most important interaction processes of photons with matter are the photoelectric effect, the Compton scattering (including Thomson and Rayleigh Scattering) and pair production. Which process dominates is dependent on the mass absorption characteristics of the target (directly related to the atomic weight, Z) and on the energy of the X-rays. Figure 2.1 shows the predominant regions for each effect as a function of the photon energy and the atomic number of the absorber.

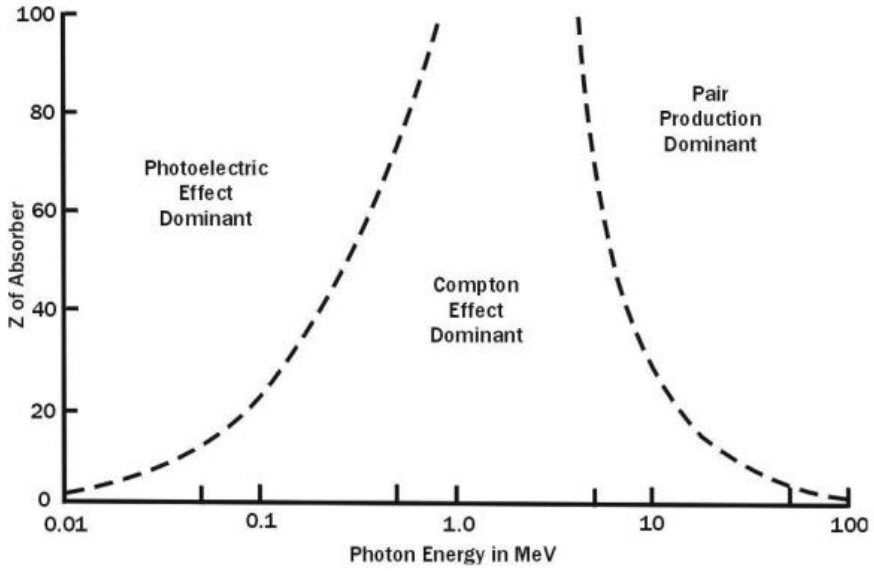

Figure 2.1: Regions of dominance of each effect as a function of the photon energy. The dashed lines show the values of Z and E for which the two neighbouring effects are equal [4].

The photoelectric effect, first understood by Einstein [5], is predominant for lower energies (below 0.5 MeV) and for absorber materials with higher atomic number. This effect is a quantum process that happens when the energy of the incident photon, $h\upsilon$, is larger than the biding energy of the electron in the shell, E_b. Its energy is totally transferred to the electron originating ionization. Some of the photon energy is used to remove the electron from the shell and the remainder is converted into electron kinetic energy. The energy of the outgoing electron is then:

$$E_e = h\upsilon - E_b \tag{2.2}$$

After an electron has been removed, the interaction leaves the atom in an ionized state, with a vacancy in one of its bound shells (typically K or L). Right after, an electron moves to fill in the gap resulting in a release of energy by the atom. This transition leads do the emission of a characteristic X-ray with energy equal to the difference between the two shells or to the emission of an Auger electron with an energy equal to the difference between the energy of the initial electronic transition and the ionization energy of the electron shell from which the Auger electron was ejected. Generally, the probability of the Auger effect increases with a decrease in the difference of the corresponding energy states, and it is the highest for the low-Z elements. For Argon about 15% of the photoelectric absorptions are followed by the emission of characteristic X-rays, while in 85 % an Auger electron is produced [4]. The characteristic X-ray can be reabsorbed close to the original site through photoelectric effect, or they can also escape from the sensitive volume of the detector and influence their response, giving origin to Escape Peaks.

At energies above 0.5 MeV, Compton scattering starts to dominate the interactions. This effect occurs when a photon interacts with an outer orbital electron (called free electrons, because their energy is much lower than the energy of the photon), which receives kinetic energy and recoils from the point of impact. The incident photon is then deflected by its interaction and is scattered from the site of the collision with an angle θ.

The energy of the recoil electron, E_e , and the energy of the scattered photon, $h\nu'$, can be obtained from the equations:

$$E_e = h\nu - h\nu' = h\nu\left(\frac{\left(h\nu/m_0c^2(1-cos\theta)\right)}{\left(1+(h\nu/m_0c^2)\,(1-cos\theta)\right)}\right) \tag{2.3}$$

$$h\nu' = \frac{h\nu}{1+(h\nu/m_0c^2)\,(1-cos\theta)} \tag{2.4}$$

where m_0c^2 is the rest-mass energy of the electron (0.511 MeV).

For energies above 1.02 MeV (the double of the rest mass of one electron) another process dominates – the *pair production*. This process involves the transformation of a photon into an electron-positron pair. If the photon has energy greater than necessary, 1.02 MeV, the excess of energy is converted into kinetic energy, which is shared

between the positron and the electron. This process is, however, non-existent for the energies used on this work (under 25 keV).

In cases where the materials are not sufficiently thick, some of the incident radiation is transmitted. For certain energy, this transmitted radiation is a function of the probability per unit path length that the photon is removed from the initial beam:

$$I = I_0 e^{-\mu x} \tag{2.5}$$

where I and I_0 are the transmitted and incident X-ray intensities, μ is the linear attenuation coefficient of the material and x is the thickness. Equation 2.5 shows that the transmitted X-ray intensity drops exponentially with the thickness of a given material.

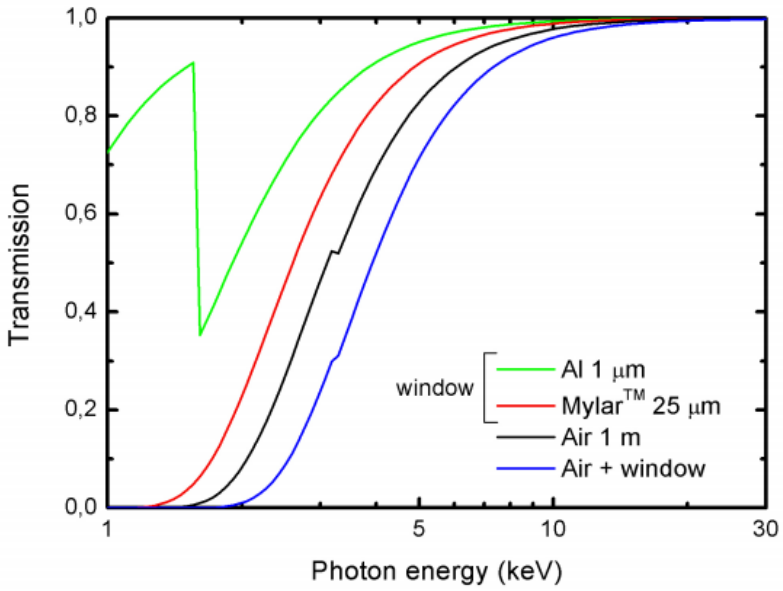

Figure 2.2: X-rays transmission as a function of photon energy through 25 μm thick aluminised Mylar™ window, 1 m of Air and both [6].

From equation 2.5 it is also possible to derive the transmission of X-rays through a certain thickness of material. Figure 2.2 shows the transmission of X-rays as a function of its energy for 1 metre of air and for a 25 μm thick aluminised Mylar™ window, where the aluminium layer has a thickness of 1 μm. The typical experimental situation where the X-ray tube is placed at a distance of 1 m (air plus window) is also

represented in the figure. Both aluminium K-edge at 1.6 keV and argon (air curve) K-edge at 3.2 keV are perceptible in the transmission curve.

2.1.2. Electrons

Electrons lose their energy through Coulomb interactions and, because of their small mass, also through radiative processes (*bremsstrahlung).* This process arises from the acceleration of the electron when it is deviated from its straight-line course by the electrical attraction of the nucleus.

The *stopping power* appears from a theory developed by Hans Beth [7] and it is defined as the differential energy loss for the particle divided by the differential path length:

$$S = -\frac{dE}{dx} \tag{2.6}$$

The value (dE/dx) referred also as the *specific energy loss,* can be described by the Beth-Block formula [4]:

$$\left(\frac{\mathrm{dE}}{\mathrm{dx}}\right) = \frac{4\pi \mathrm{r e}^4 \mathrm{z}^2}{\mathrm{m_0 v}^2} \mathrm{NZ}\left[\ln\frac{2\mathrm{m_0 v}^2}{\mathrm{I}} - \ln(1-\beta^2) - \beta^2\right] \tag{2.7}$$

where v and ze are the velocity and charge of the primary particle, N and Z the density and atomic number of the absorber atoms, m_0 the electron rest mass and $\beta = v/c$.

For electrons, the specific energy loss due to collision interactions, per unit of distance travelled is given by [4]:

$$-\left(\frac{dE}{dx}\right)_{coll} = \frac{4\pi \mathrm{r e}^4}{\mathrm{m_0 v}^2} \mathrm{NZ}\left[\ln\frac{\mathrm{m_0 v}^2 \mathrm{E}}{2\mathrm{I}^2(1-\beta^2)} - \ln(2)\left(2\sqrt{1-\beta^2} - 1 + \beta^2\right) + (1-\beta^2) + \frac{1}{8}\left(1-\sqrt{1-\beta^2}\right)^2\right] \tag{2.8}$$

The electrons also lose energy by radiative processes. The specific energy loss due to this process is [4]:

$$-\left(\frac{dE}{dx}\right)_{rad} = \frac{NEZ(Z+1)e^4}{137m_0^2c^4}\left(4\,ln\frac{2E}{m_0c^2} - \frac{4}{3}\right) \quad (2.9)$$

The total energy loss of electrons is then composed of two parts:

$$\left(\frac{dE}{dx}\right)_{tot} = \left(\frac{dE}{dx}\right)_{rad} + \left(\frac{dE}{dx}\right)_{coll} \quad (2.10)$$

From the equations of the collisional (equation 2.8) and radiative (equation 2.9) stopping powers it is possible to obtain the ratio of the specific energy losses [4]:

$$\frac{(dE/dx)_{rad}}{(dE/dx)_{coll}} \cong \frac{EZ}{700} \quad (2.11)$$

where Z is the atomic number of the medium and E is the energy in MeV. The last equation shows that for the energy range (1-25 keV) and the gas medium (argon – Z=18) used on this work, the right term is much smaller than 1 and therefore the radiative losses are always a small fraction of the energy losses due to ionization and excitation.

A charged particle moving through a certain material loses its kinetic energy through the interactions with the material. Electrons are light particles, therefore a tortuous path through absorbing materials. This crisscross path is possible because the electron mass is equal to that of the orbital electrons with which it is interacting. Then a much larger fraction of its energy can be lost in a single interaction. As it will be described in section 3.3.3.2, the electron range is very important to find the best position resolution of a gas in an imaging system.

The path length can be obtained from equation 2.6 by integrating the inverse of the stopping power:

$$x = \int_0^E \frac{dE}{S} \quad (2.12)$$

2.1.3. Ions

When compared to electrons, ions are heavier particles. Those resulting from ionising incident radiation have a very low kinetic energy. As it was said before, the interaction of ionising radiation with matter leads to the creation of ion-electron pairs. While the electrons have a high mobility, the ions, even in the presence of high electric fields, have an extremely low mobility which makes them slower. As a consequence, their drift time is very long. This is one of the main problems of gaseous detectors.

Ions are also produced by other sources. Nuclear reactions or particle accelerators generate high energetic ions. When they penetrate a material the energetic ions lose energy through Coulomb interactions with atomic electrons and with the nuclei. The last one is negligible in terms of energy loss [4].

Figure 2.3 shows the energy loss of proton as a function of the depth of penetration in the material it interacts.

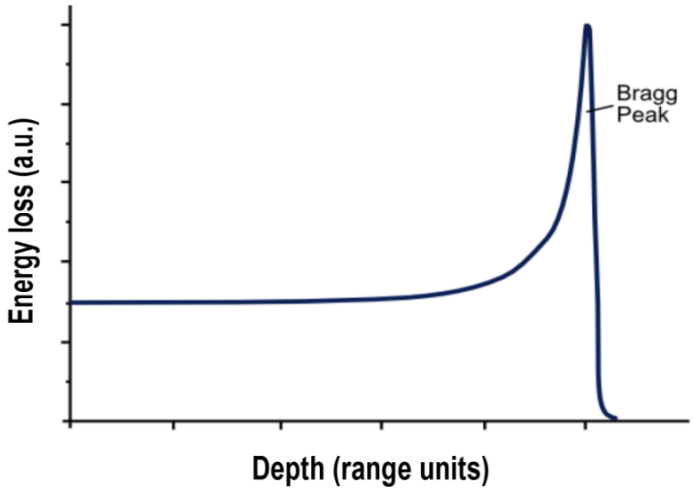

Figure 2.3: A typical Bragg curve showing the variation of the energy loss as a function of the penetration depth. The proton is more ionizing towards the end of its path.

This is known as a *Bragg curve*. At the beginning, the energy loss of the proton is small. But as it penetrates deeper in the material the energy loss rate starts to increase. At some point, the proton starts to capture electrons from the atoms of the material,

reaching a maximum of energy deposition. This maximum is known as *Bragg peak*. Here, near the end of the trajectory, the particle deposits most of its energy.
Because of this behaviour, these particles are used in medical applications since they deliver most of its energy at a precise depth. This way, the Bragg peak occurs exactly within the tumour site sparing the healthy neighbouring tissue.

2.2. Brief History of Gaseous Detectors

In 1908, in Rutherford´s laboratory, Geiger introduced the first steps on the use of gas counters for radiation detection. Most of the oldest radiation detectors are based on the effects produced when a charged particle passes through a gas and then based on the direct collection of the ionization electrons and ions produced. These electron-ion pairs created by the ionizing radiation are separated by the use of an electric field between the cathode and the anode electrodes. Because of this electric field, the electrons drift away from the positive ions. The charge flow induces a charge pulse that can be measured through appropriate electronics. However, if an electric field is not applied, the probability of recombination increases and equilibrium is reestablished with the recombination of the free electron and the positive ion.

As the electric field increases, the number of electrons that reach the anode increases as well, until all of them are collected. At this point, the increase of the electric field does not increase anymore the number of electrons that reaches the anode. It is actually the velocity reached by the electrons between collisions that keep increasing.

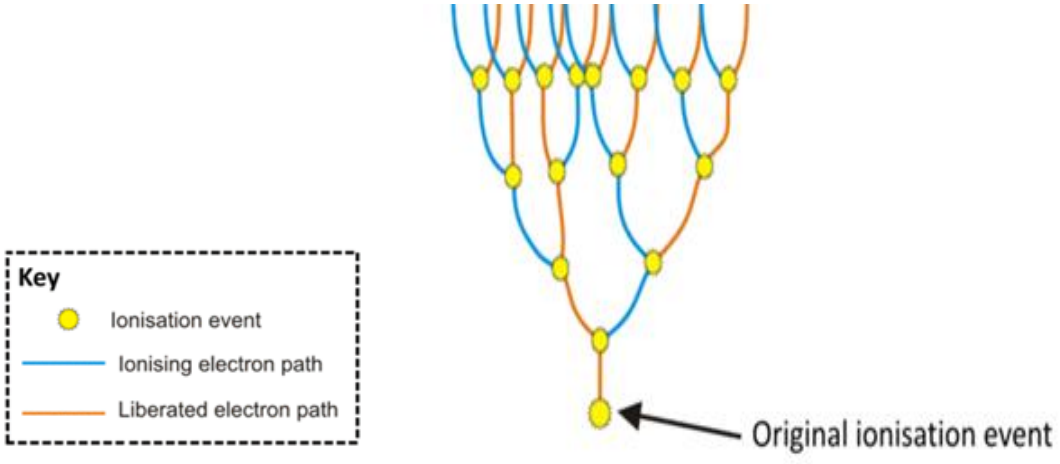

Figure 2.3: Townsend avalanche process.

At some point (threshold for gas multiplication) the electric field becomes so high that the electrons acquire enough kinetic energy to remove electrons from the atoms of the gaseous medium. These new free electrons will also feel the electric field, gain acceleration and remove more electrons giving origin to a charge avalanche – the *Townsend avalanche* (Fig. 2.3). The fractional increase in the number of electrons per unit path length is given by the Townsend equation:

$$\alpha = \frac{dn}{n}\frac{1}{dx} \tag{2.13}$$

where α is the first Townsend coefficient for the gas.

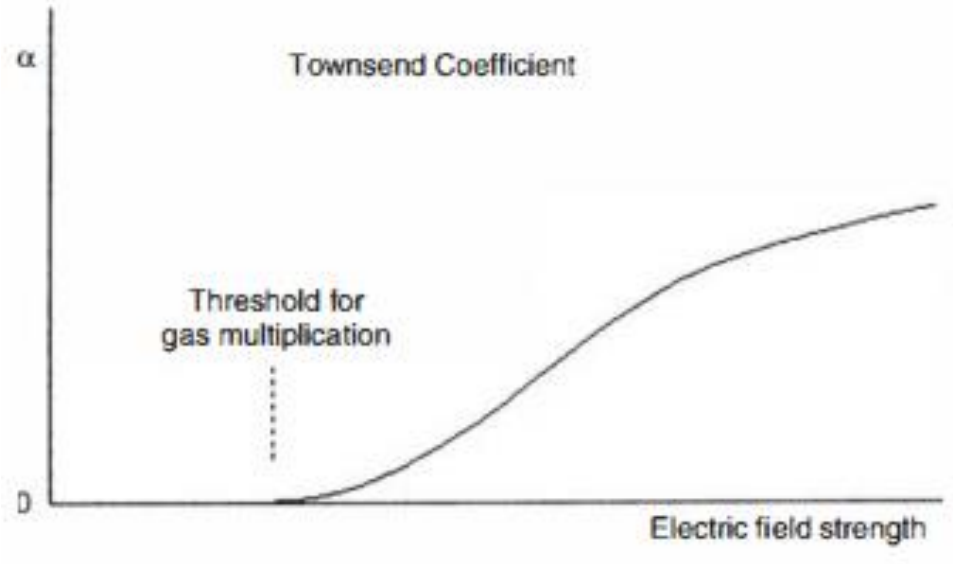

Figure 2.4: Plot of the first Townsend coefficient as a function of electric field strength [4].

As it can be seen from figure 2.4, below the threshold for gas multiplication, the Townsend coefficient value is zero. Above this point, the coefficient grows with the field strength.

The gas detectors can be classified according to their voltage region operation.

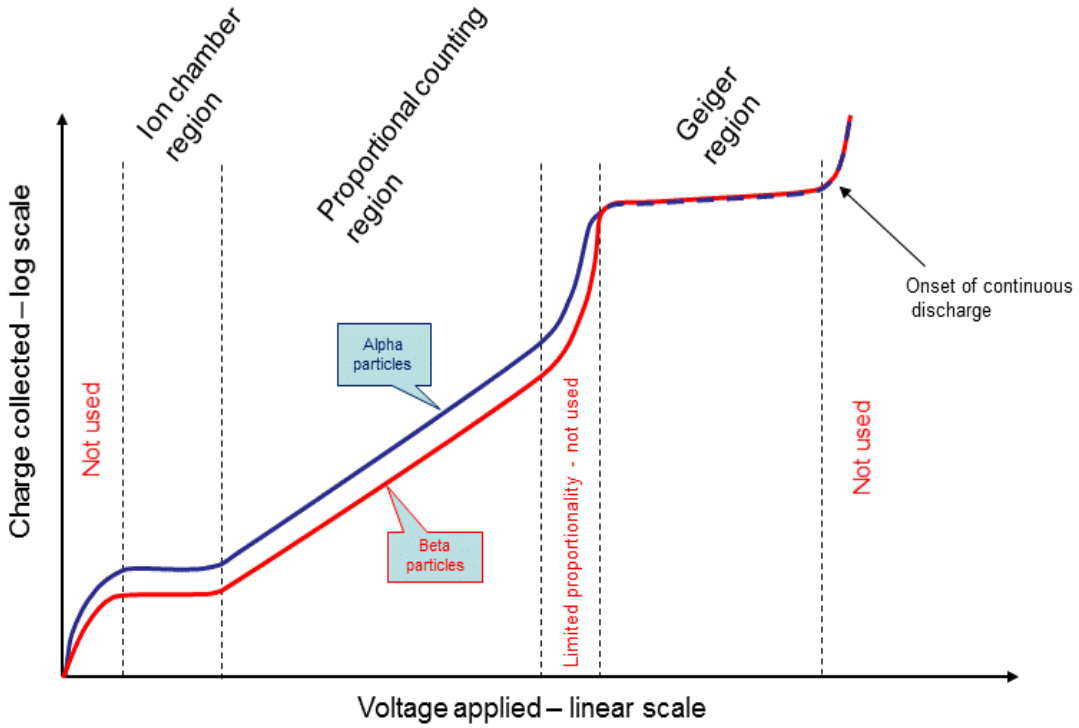

Figure 2.5: The different regions of operation of gaseous detectors [8].

At very low values of the voltage, the electric field is not enough to prevent the recombination of the ion pairs. The charge collected is less than that represented by the original ion-electron pairs. An electric field increase leads to a decrease of the recombination processes. When the *ionization region* is reached the recombination rate is zero and all charges created by the primary ionization are collected. However, the electric field strength is still not enough to induce secondary ionizations. As the electric field is increased still further, the threshold field at which gas multiplication starts is reached. This is the *proportional region*, because the total number of electrons in the avalanche is proportional to the number of primary electrons. Here the electric field is strong enough to produce additional ionizations from the primary electrons. These secondary electrons can acquire enough energy to produce an avalanche of ionizations. Here the output signal is proportional to the energy deposited in the detector by the incident radiation. The gain in charge increases with the further increase of the electric field. At some point the Geiger-Müller region is reached. Here due to positive charge accumulation, the electric field is distorted because of space charge effects and the

proportionality is lost. Figure 2.5 shows the different regions of operation described above.

Before the introduction of Micropattern Gaseous Detectors (MPGD) a long era has transpired concerning the development of electron avalanche based detectors. This brief historical review will mention only a small fraction of the work done until the development of the MPGDs.

The history of gaseous detector development is schematically depicted in Figure 2.6. The whole story began with the discovery in 1900, by Townsend, of the process of avalanche multiplication of electrons in gas under the influence of very intense electric fields. This effect led to the invention around 1905 of the single-wire detector of charged particles. Firstly these counters were operated in corona discharge mode, but subsequently they started to be operated in proportional mode.

In the early stage (1950–1965), the most intensive and successful developments of detectors with two-dimensional (2D) position capabilities regarded parallel-plate sparks and streamer chambers operated in pulsed mode and combined with optical imaging systems.

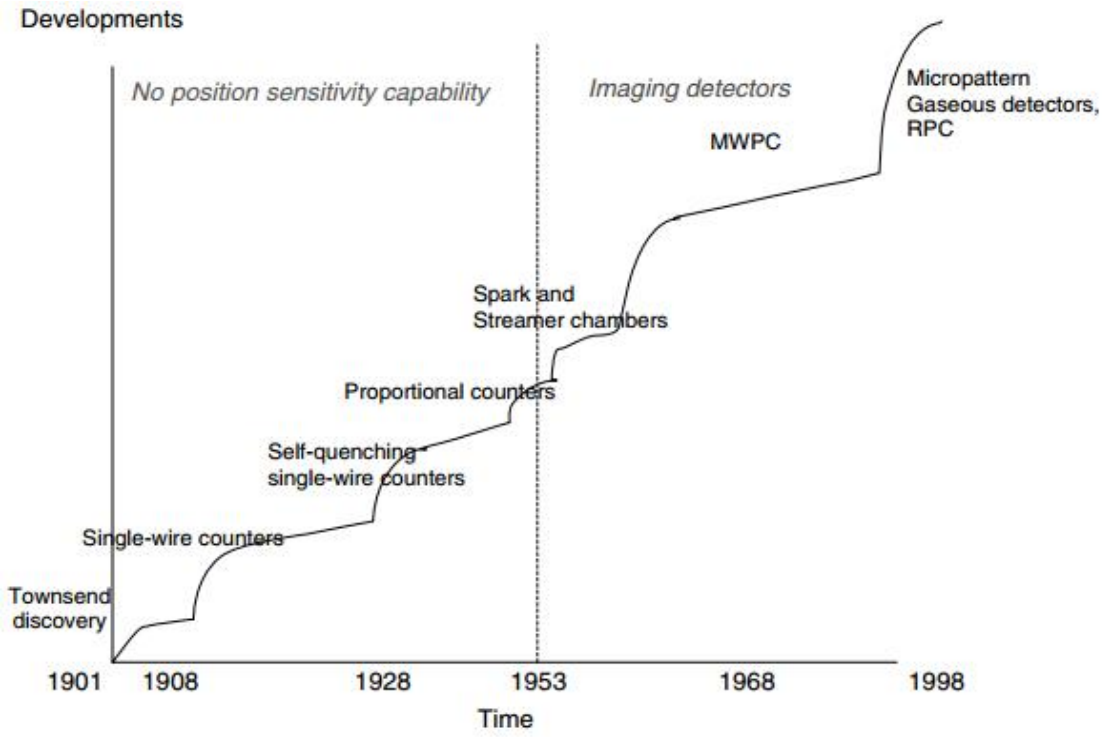

Figure 2.6: A schematic summary of gaseous-detector developments [8].

In 1967–1968, the first streamer chamber was manufactured. It was equipped with an electronic readout, which allowed the imaging of signals induced by the streamers on multiwire electrodes.

The real revolution in the development of imaging gaseous detectors started with the invention by G. Charpak [9] in 1968 of the Multiwire Proportional Chamber (MWPC). This detector was able to obtain fast electronic images of photons and tracks of elementary charged particles with a 1-D position resolution better than 100 μm. For this great invention, which really revolutionized the detection technique, Charpak was awarded in 1992 with the Nobel Prize in Physics.

In the beginning of 1990, a new breakthrough happened in the technology of gaseous detectors as a result of the efforts of several teams, the so-called *micro-pattern gaseous detectors* were developed. These novel detectors are manufactured via modern microelectronic techniques, which not only made their production easy, but, more importantly, allowed the achievement of very good position resolutions. Moreover, in some lay-outs, the microelectronic readout is integrated in the detector itself.

2.2.1. Gas Proportional Counter

The basic configuration of a gaseous proportional counter is a cylinder container with the walls working as a cathode, filled with a suitable gas (usually a noble gas) and a thin anode wire at its centre (Figure 2.7). This kind of detector works in the proportional counting region where the pulse height is proportional to the charge of the primary electron cloud which therefore is proportional to the energy of the incident radiation.

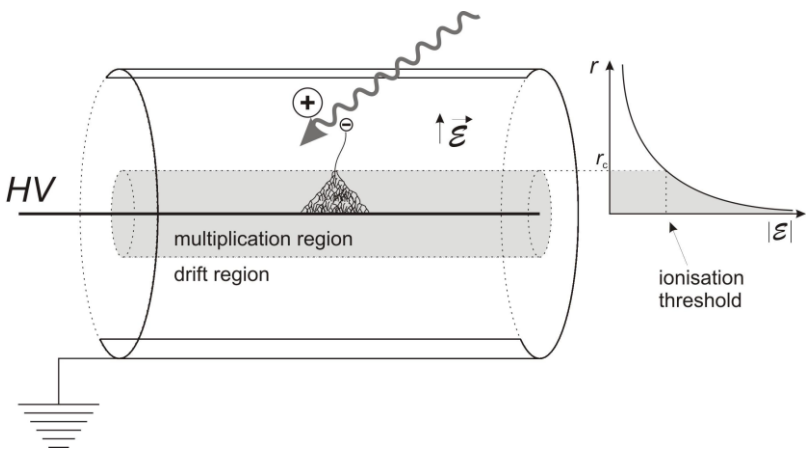

Figure 2.7: Schematic of the Gas Proportional Counter. In the drift region the radiation is absorbed and ion-electron pairs are created. Because of the electric field (graphic in the right) the electrons are multiplied in the multiplication region (region where the electric field is above the ionisation threshold – Figure 2.4) [6].

The electric field inside of the detector is given by:

$$\varepsilon(r) = \frac{V}{r \ln(b/a)} \tag{2.14}$$

where V is the voltage applied to the wire, r de distance to the axis and a and b are the anode wire and cathode radius.

As it can be seen from equation 2.14 the electric field inside the detector presents a radial dependence and near the anode the electric field reaches values way above the threshold for multiplication. The primary electrons produced simply drift through the low field regions until they reach the close vicinity of the anode where they suffer the multiplication processes described before.

2.2.2. Geiger-Müller Counter

The Geiger-Müller counter is one of the oldest radiation detector types, having been introduced by Geiger and Müller in 1928 [10]. This detector has the same geometry that the one outlined in the figure 2.6. However, the operation voltage is raised to bring the electric field to the Geiger region. In this region, the ion pairs generated by the incident particle feel a very high field. Some of them will have enough energy to ionize neighbouring atoms and molecules and others to excite them, which, upon subsequent de-excitations leads to the emission of photons. These photons can remove electrons elsewhere from the medium, creating more free electrons. Under proper conditions, an avalanche can itself trigger a second avalanche at a different position inside the counter. Within a very short period of time, an exponentially growing number of avalanches can be created and the whole tube gets ionised. As a consequence, a large charge pulse is

created and collected from the anode wire. *All pulses from a Geiger tube are of the same amplitude regardless of the number of ion pairs that initiated the process*. Because of this and since all the information on the amount of energy deposited within the detector by the incident radiation is lost, the Geiger-Müller Counter can only be used as a counter of events.

This detector is frequently used in radiation monitoring devices for security applications due to their portability and cheap electronics.

2.2.3. Gas Proportional Scintillation Counter

The Gas Proportional Scintillation Counter (GPSC) is considered a peculiar type of a Proportional Counter. The GPSC has been developed by Conde and Policarpo [11] in the Physics Department of the University of Coimbra.

When the primary electrons created by the incident radiation do not have enough energy to ionize the atoms of the medium, they can excite them by inelastic collisions. When an excited electron falls back to a state of lower energy (de-excitation processes), ultra-violet light (photons) is emitted isotropically. This light can be detected by a *photomultiplier tube* (PMT) or any other light sensor. The intensity of scintillation detected by the photocathode is proportional to the number of primary electrons produced, which are proportional to the energy of the incident particle.

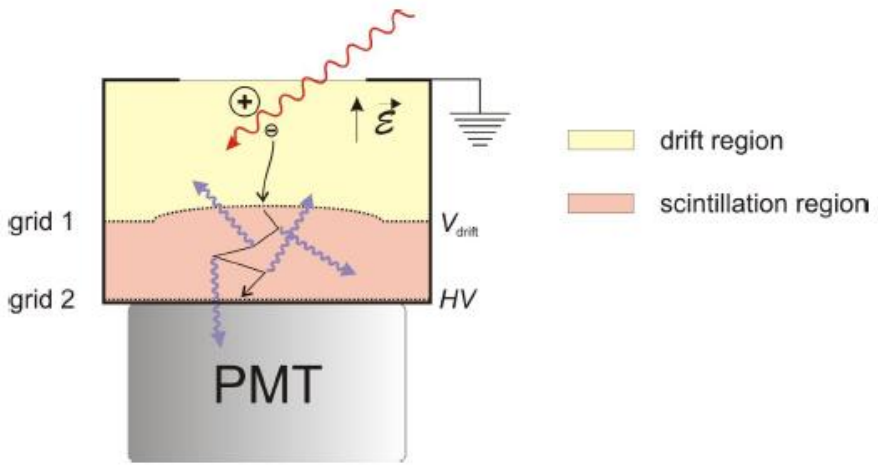

Figure 2.8: Schematic of the Gas Proportional Scintillation Counter with an ellipsoidal grid and an attached PMT (photomultiplier tube) [6].

The standard GPSC is composed of two grids and two different regions – the *drift* region and *scintillation* region. The PMT is coupled to the last one. X-rays entering the detector through the window are absorbed in the volume between the grounded detector window and a polarised grid (the drift region) where the primary electron-ion pairs are produced. Due to the influence of the electric field, the primary electrons drift to the region between the two grids (the scintillation region). Since the second grid is at a much higher potential, a more intense electric field is created and the electrons are accelerated enough to excite but not ionize the atoms or molecules of the medium, producing the scintillation light. Finally, the light readout is made with a PMT.

The great advantage of these detectors is that they are capable of being used in large detection areas with an energy resolution better that that achieved when the charge is collected (typical energy resolutions of 8% for 5.9 keV [12]).

2.2.4. Multiwire Proportional Chamber

The discovery of the Multiwire Proportional Chamber (MWPC) by Charpak [9] (Figure 2.9) was a huge step forward for the physics of radiation. Owing to its unique properties, MWPCs almost immediately took over and became the main choice for instrumenting high-energy experiments for several decades.

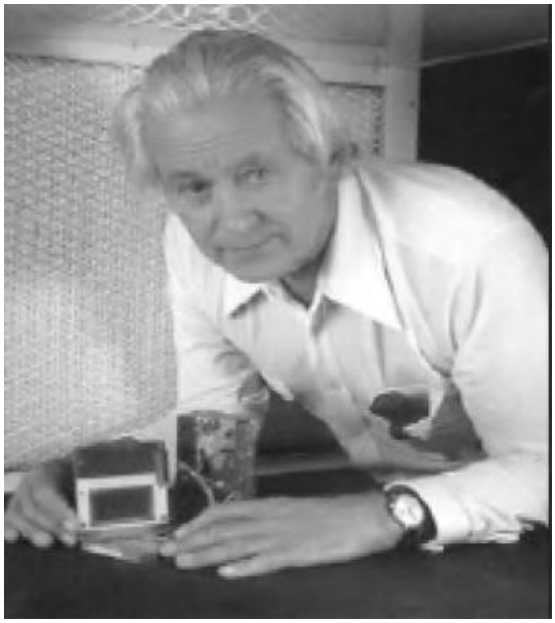

Figure 2.9: Photograph of G. Charpak with the first prototype of a wire (drift) chamber in his hands.

This detector in its simplest form essentially consists of thin parallel and equally spaced anode wires symmetrically sandwiched between two cathode planes. Cathode planes can be a set of thin equally spaced wires but also can be made of a continuous plane conductors. The gap between the plane of the anode wires and the cathode plane is normally a few millimetres. The chamber is filled with an appropriate mixture of gases depending on the desired mode of operation. With this setup it is possible to have sensitive areas of the order of square meters.

If an ionizing process occurs in the gas, the primary electrons produced will drift towards an anode wire. The primary charge is distributed over a few wires in the vicinity of the interaction point. Far away from those wires the electric field (Figure 2.10) is constant, however, near them the electric field becomes inversely proportional to the square of distance (r) to the wire, and therefore the primary electrons gain enough kinetic energy so that inelastic collisions with the gas molecules can lead to new ionizations, with the creation of secondary electrons and an electron avalanche as in the proportional counter already described in section 2.2.3.

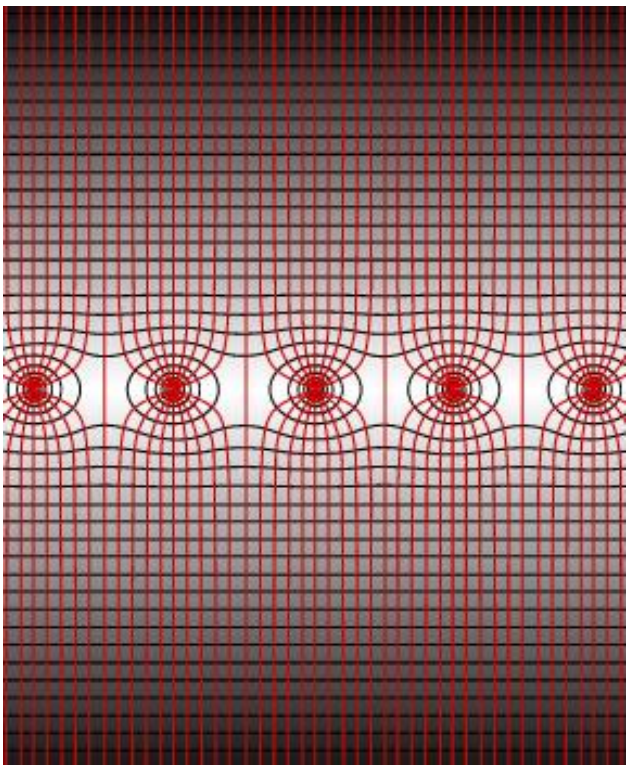

Figure 2.10: Typical Electric field and potentials lines in a MWPC.

The MWPC is also “position sensitive”. Each one of the cathode parallel strips can be connected to an amplification and shaping electronic chain and act as an individual detector. This allows to determine the position where the interaction takes place. This kind of chamber can also work as a 2D-imaging detector (figure 2.11) if the strips of one plane are oriented perpendicular to the strips of the other plane (x-coordinate independent of the orthogonal y-coordinate). Figure 2.11 shows the basic setup of the MWPC adapted for imaging applications.

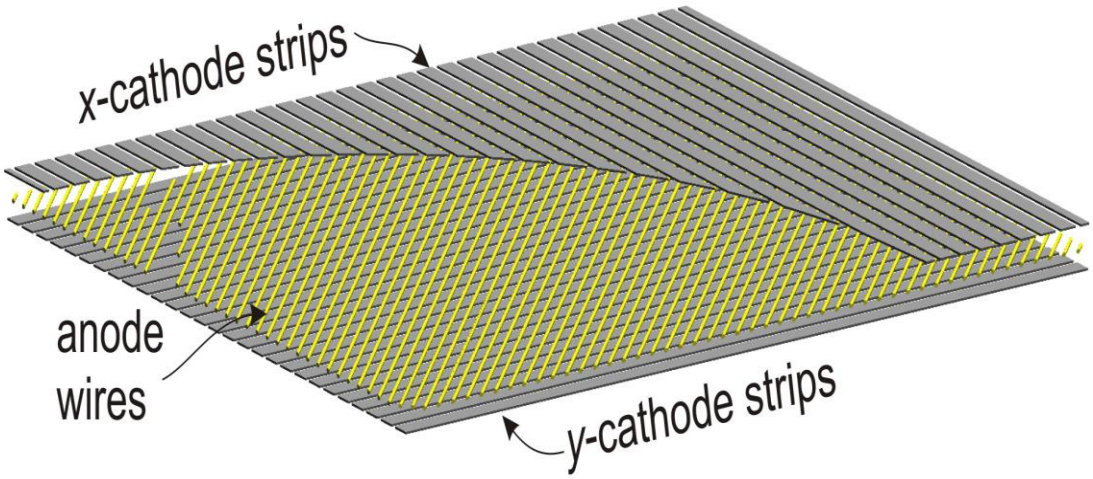

Figure 2.11: Basic setup of the MWPC used for imaging applications. The charge induced in the strips of the cathode can be used to determine the coordinates of the ionization event [6].

Very often, in order to reduce the number of electronic channels, the cathode wires are grouped by connecting several wires together through resistive or delay lines. The measured signals are treated by center of gravity algorithms and a positon resolution better than the distance between the anode wires is achieved [13][14]. The main aim of these efforts was to find a way to reduce the number of readout channels and thus the cost of the electronics.

2.2.5. Micropattern Gaseous Detectors

The invention of the MWPC was a huge step in radiation physics. However, the new challenges of the modern Physics experiments led to the development of new detection concepts. A breakthrough in this direction was achieved by Oed of the Institut Laue-Langevin, France, who suggested the application of microelectronics techniques (precision circuit board printing techniques) in the manufacturing of gaseous detectors, leading to a simplification of their construction, opening the door for the so called Micropattern Gas Detectors (MGPD) [15].

The need of detectors able to provide good energy resolutions and able to be constructed with large areas for imaging applications triggered a series of inventions and upgrades such as: The Microstrip Gas Detector [16], The Micromesh Gaseous Structure [20], and The Gas Electron Multiplier [23], just to name a few devices. This type of detectors includes a variety of electrode geometries: strips, dots, and hole-type micro-structures.

These novel detectors are characterized by two main features. First, the gap between the anode and the cathode electrodes is usually very small, sometimes smaller than 50 μm. Second, the electrode structures are manufactured via microelectronic technology allowing achieving a very high granularity and thus a position resolution much better than in the case of the MWPCs.

2.2.5.1. The Microstrip Gas Detector

The Microstrip Gas Counter (MSGC) was introduced by Oed in 1988 [16]. The MSGC is the result of a series of attempts to build a highly granular Multiwire Proportional Chamber in which the anode wires are less than 2 mm apart. The forward step when compared to the MWPC was the substitution of the wires by small metal strips printed in a thin planar insulating substrate.

The basic Microstrip Gas Chamber (Figure 2.12) consists of alternating thin metal strips laid on an insulating support with a pitch of a few hundred microns. These metal strips, anodes and cathodes, have a width of 10 and 100 μm, respectively. This means a

reduction in the electrode thickness by one order of magnitude when compared to the MWPC. An upper drift electrode (drift plane) delimits the sensitive gas volume. The insulating substrate is usually made of glass with a diamond coating and the strips are made of gold or chromium. It can also be segmented in readout strips for two-dimensional localization.

The electrons resulting of the incident radiation interactions with the medium drift to the microstrip plane, where due to the strong electric field around the anodes, experiences avalanche amplification. Therefore, the electrons are collected on the anodes while the ions are collected by the cathodes.

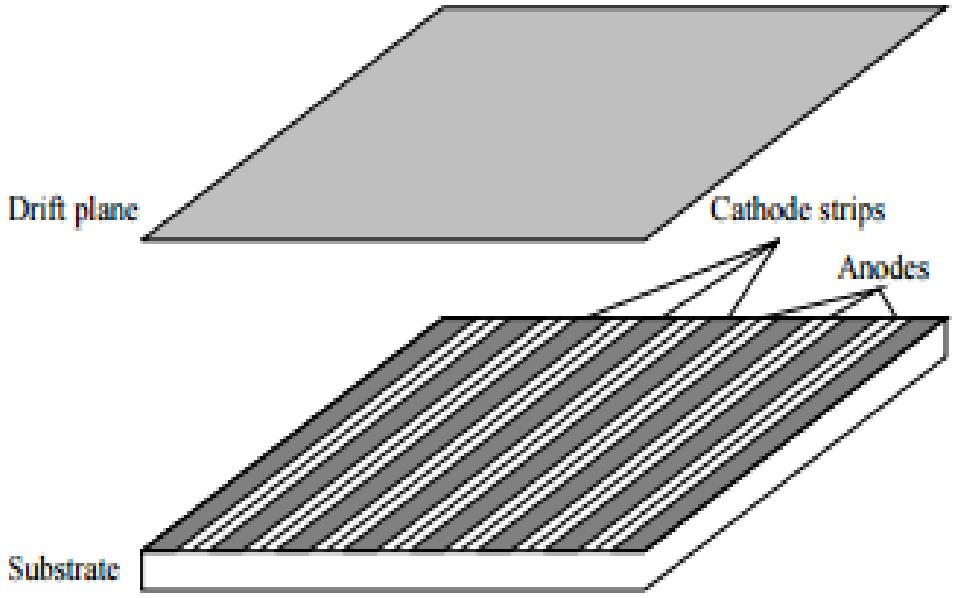

Figure 2.12: Outline of the MSGC detector: a substrate carrying conductive strips is positioned in a gas volume, covered by a conductive drift plane.

Oed's detector shows a number of advantages over the classical wire chamber. In the MWPC the ions had to drift a long way until they reach the cathode (typically a few mm). This, at some point, can lead to a space charge effects. However, in the MSGC the ions just drift to the closest cathode (typically a 50 μm) and are collected quicker. Therefore, the MSGC can reach higher count rates before the detector performance starts to suffer from space charge effects. Faster signals and better time resolution is

also achieved. Its high granularity enables an accurate position determination of the liberated charge (by identifying which of the anode strips register a signal) and hence tracking of the ionising event. The 2D capabilities of the MSGC, through resistive and delay lines methods, are explored in some papers [17][18].

The Micro Strip Gaseous Detector allowed to achieve gains of the order of 10^3. The small gain and the difficulty to cover larger areas are the main drawbacks of this device. The last one can be overcome using several microstrips planes together, as was done in some physic experiments [18]. Nowadays the microstrip pattern can be repeated indefinitely and areas of the order of $100\ cm^2$ are used as a standard. A big limitation of the MSGC is the gain it can reach. It doesn't exceed 10^3 due to breakdown of the insulator surface. The positive ions created during the avalanche processes tend to accumulate on the surface of the insulator, modifying the electric field due to space charge effects (principally at high radiation rates) and causing a drop of the gain. Due to the small gap between the anode and the cathode strips, discharges are very likely to happen specially when exposed to high fluxes and heavy ionizing particles. Usually, these discharges are fatal for this kind of structures. So the use of higher voltages is not the solution to achieve higher gains. The development of a type of glass material with the right electron conductivity for the substrate, allowed to around the accumulation of ions in the insulator [19].

In order to overcome these drawbacks and satisfy new scientific demands a new generation of Micro Pattern Gas Detectors was explored. Some examples are the MicroMegas and the Gas Electron Multiplier.

2.2.5.2. The Micromesh Gaseous Structure

The MicroMegas (for MICRO MEsh GASeous Structure) is a high gain gaseous detector that was introduced in 1996 by Giomataris [20] as an alternative to the MSGC. The device combines high accuracy, high rate capability, excellent timing properties and robustness. Figure 2.13 shows a schematic view of the layout of MicroMegas detector.

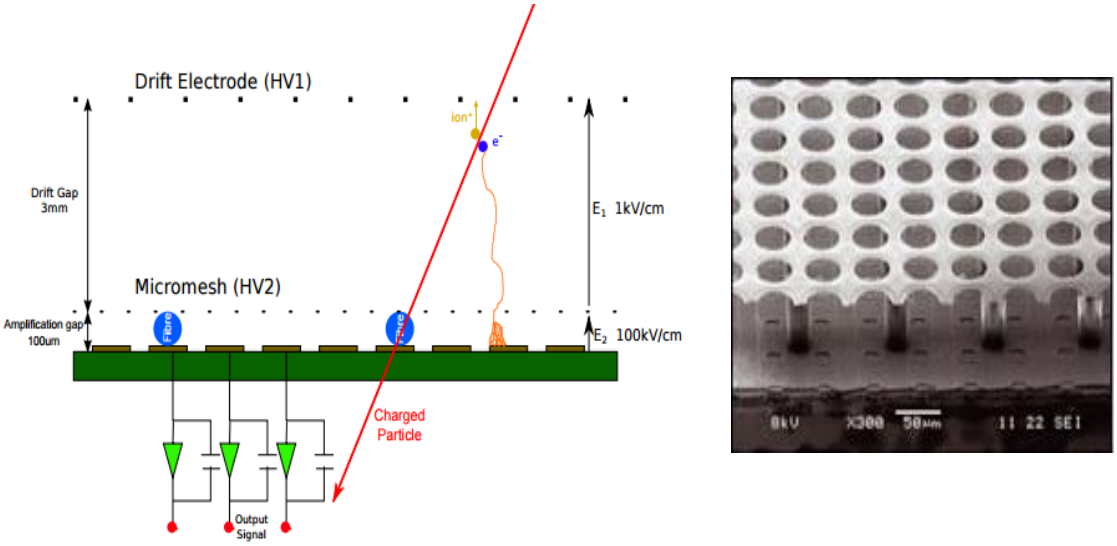

Figure 2.13: Schematic view of the layout of the MicroMegas (left) and a microscope photograph of the structure (right).

It is a two-stage parallel plate avalanche chamber characterized by a narrow amplification gap (usually smaller than 100 μm [21]) defined between the anode and the cathode. This allows reaching very high electric fields. A thin nickel made metallic micromesh with 3 μm thickness works as a cathode. The strips work as the anode and are printed on a printed circuit board (PCB). The amplification gap (cathode-anode distance) is kept via small insulating pillars as shown in the right image of figure 2.13. Usually a third electrode is kept 3mm above the micromesh delimiting the drift region. The free electrons created by the ionizing radiation feel an electric field strength of about 1 kV/cm and drift towards the cathode micromesh. The electric field in the amplification region is much stronger than the one in the drift region. Here, due to this high electric field, the free electrons have the right conditions to start multiplication by avalanche processes. The ions and the electrons travel in opposite directions. The

positive ions drift to the micromesh where are collected. The electrons are collected by the anode microstrips. Since the amplification gap is small, the collection time of the positive ions is fast, typically less than $100\,ns$ [21]. This is an important step forward because the space charge effect can be reduced allowing higher gains. Gains close to 10^5 were obtained in some studies [20]. This device can also be built with large sensitive areas and used for 2D imaging applications [22].

2.2.5.3. Gas Electron Multiplier

The Gas Electron Multiplier (GEM) was introduced by Sauli in 1996 as "a new concept for electrons amplification" [23]. The aim of the work was to supress the problem of gain loss of the Microstrip Plate detectors when operated at high counting rates. The GEM consists in a simple thin Kapton™ foil (typically $50-70\,\mu m$ thick) clad in copper (about $5\,\mu m$ thick) in both sides. The structure is perforated with a matrix of holes that typically have a diameter of $70\,\mu m$ and a pitch of $140\,\mu m$. The holes are arranged in a hexagonal pattern. Figure 2.14 shows a microscope image of a typical GEM geometry.

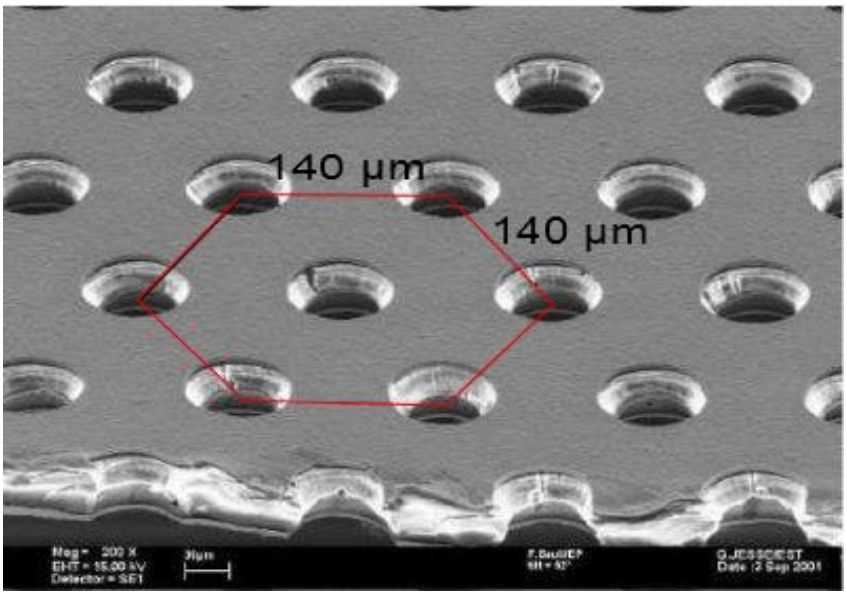

Figure 2.14: Image of the GEM structure taken with an electronic microscope. The structure is composed by a thin Kapton™ foil, metal-coated on each side and perforated by a high density of holes in a hexagonal matrix.

The free electrons, resulting from the interaction of the ionizing radiation with the medium, drift into the holes of the GEM where, due to the high field inside, the process of charge multiplication starts to occur. This happens upon the application of a proper drift field and voltage difference between the two copper electrodes (usually called Top and Bottom electrodes). The scheme of the electric field and equipotential lines inside the GEM holes is illustrated in Figure 2.15 [24]. The huge density of lines in the centre of the holes denotes how intense is the electric field there. Because of this there is an effect of focusing the drifting electrons to those holes, where avalanche multiplication takes place. The charge transmitted by the GEM proceeds to the lower region where it can be collected with position sensitive charge readouts for 2D-imaging [25][26] or carry on to another multiplier device.

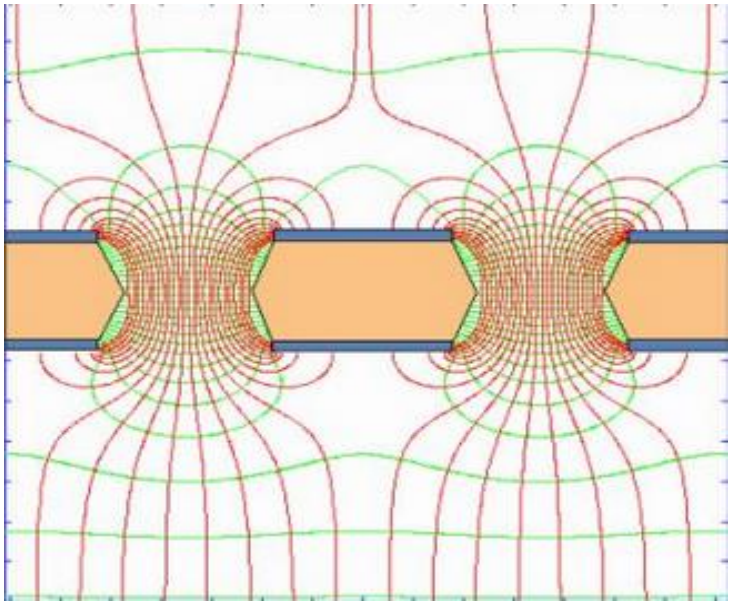

Figure 2.15: Scheme of the electric field and equipotential lines of a "standard" GEM operated at a difference of potential $\Delta V_{GEM} = 500V$, with drift and induction field of 2 and 6 $kVcm^{-1}$, respectively [24].

The GEM can be operated in single mode or, since there is transmission of charge, in a multiple cascade of several GEMs (Figure 2.16). The cascade of several GEMs allows higher gain performances. A triple-GEM detector achieves gains above 10^5 in $Ar - CO_2$ $(70 - 30)$ mixtures (Figure 2.18).

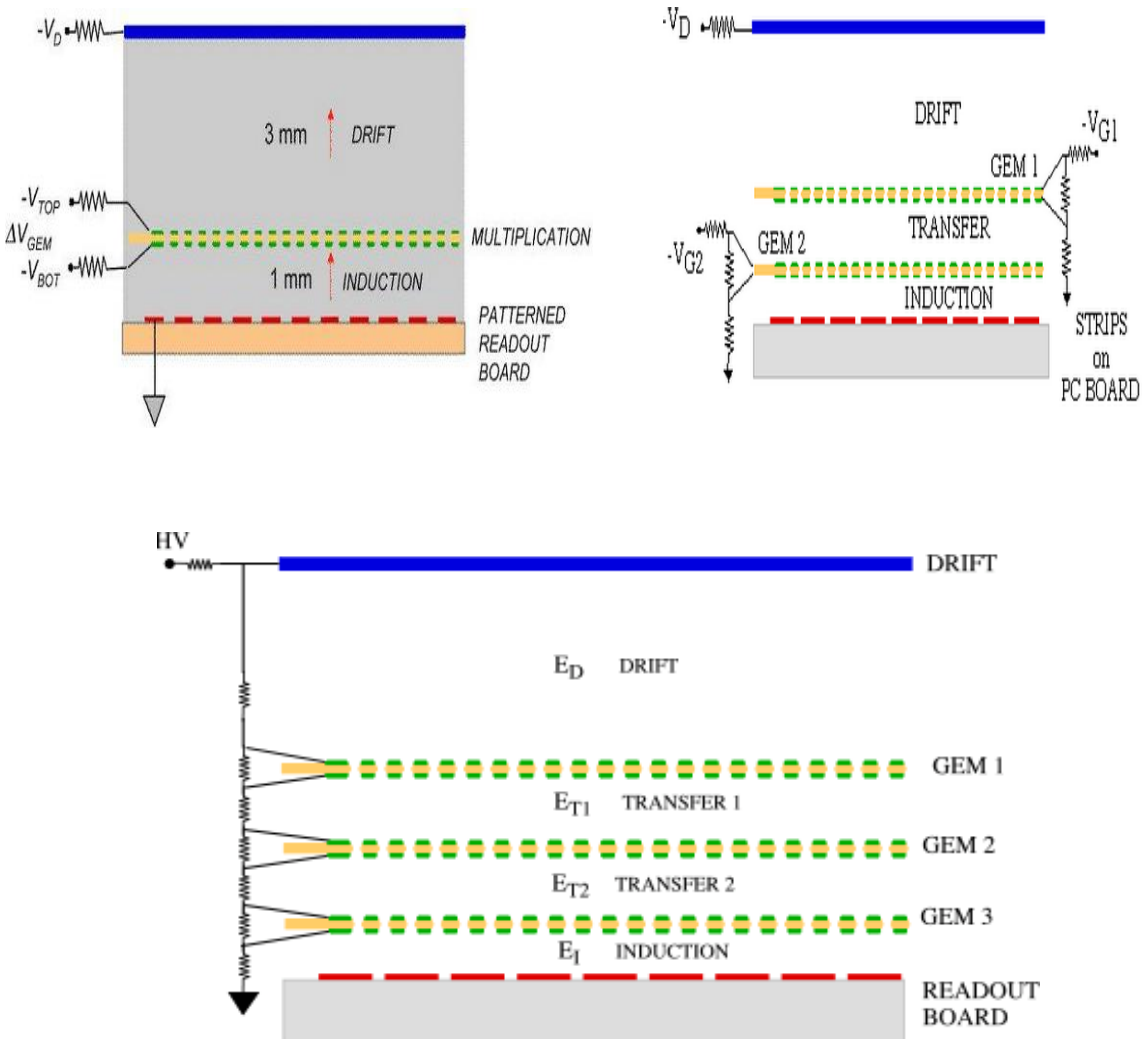

Figure 2.16: GEM operating modes: a) Single GEM configuration, b) Double-GEM configuration, c) Triple-GEM configuration [24].

Due to the small dimensions of this structure, the pulses of a GEM are just a few ns long. Another advantage of GEM detectors is that the charge multiplication and charge collection take place in separate electrodes. Because of this the signals induced on the sensitive readout are only due to electron collection. Therefore, a discharge will not affect directly the sensitive electronics. To prevent the ion back flow, which affects the detector performance, a proper choice of the applied potentials is essential.

The gain as function of the applied voltage between the electrodes in different gas mixtures and geometries can be seen in Figure 2.17 and 2.18.

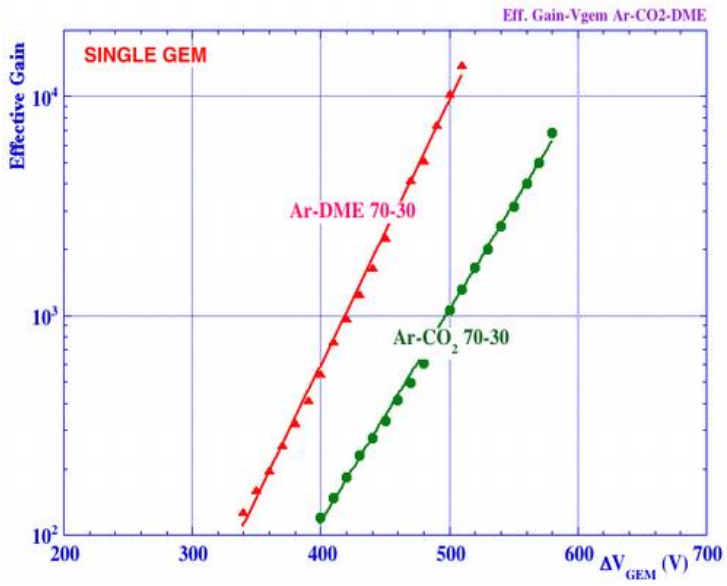

Figure 2.17: Effective gain dependence on GEM voltage for two gas mixtures [24].

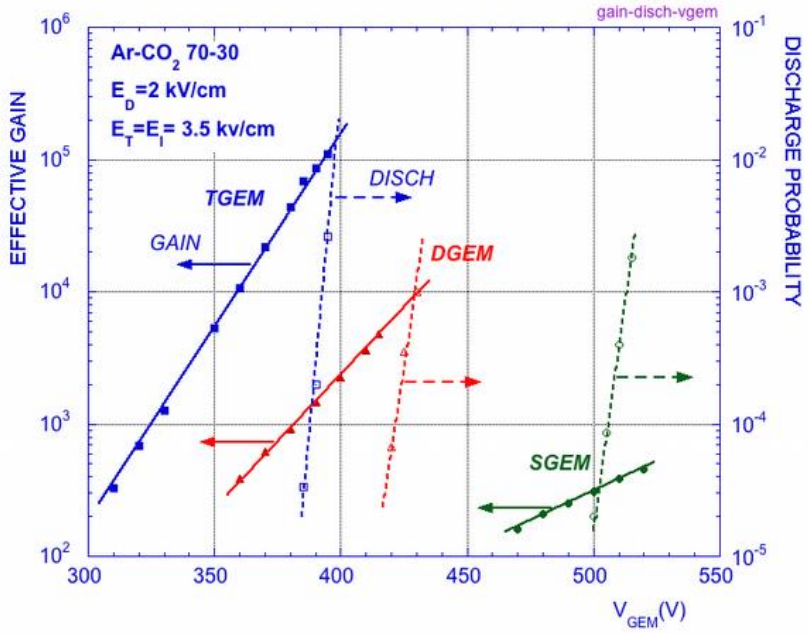

Figure 2.18: Gain and discharge probability on irradiation with alpha particles for the single, double and triple GEM [24].

The occurrence of discharges is one of the main issues of the Gas Electron Multiplier. In some cases these discharges can damage irreversibly the structure. The *Rather limit* has a crucial role in the start of a discharge. When the avalanche size exceeds this limit (10^7 ion-electron pairs) the probability of a discharge increases. This

excess of ion-electron pairs can produce a conductive channel between the anode and cathode where the discharge takes place.

Due to their prospective applications, these structures were subject of multiple studies. Their high counting rate capabilities, excellent spatial resolution, large sensitive areas and good imaging capability (Figure 2.19) are some of the characteristics that made these devices very attractive in high-energy physics experiences. Some developments were made to the “classical” GEMs. The thick-GEM (THGEM) [27] and the Micro-Induction Gap Amplifying Structure (GEM-MIGAS) [28][29] are some examples of those developments.

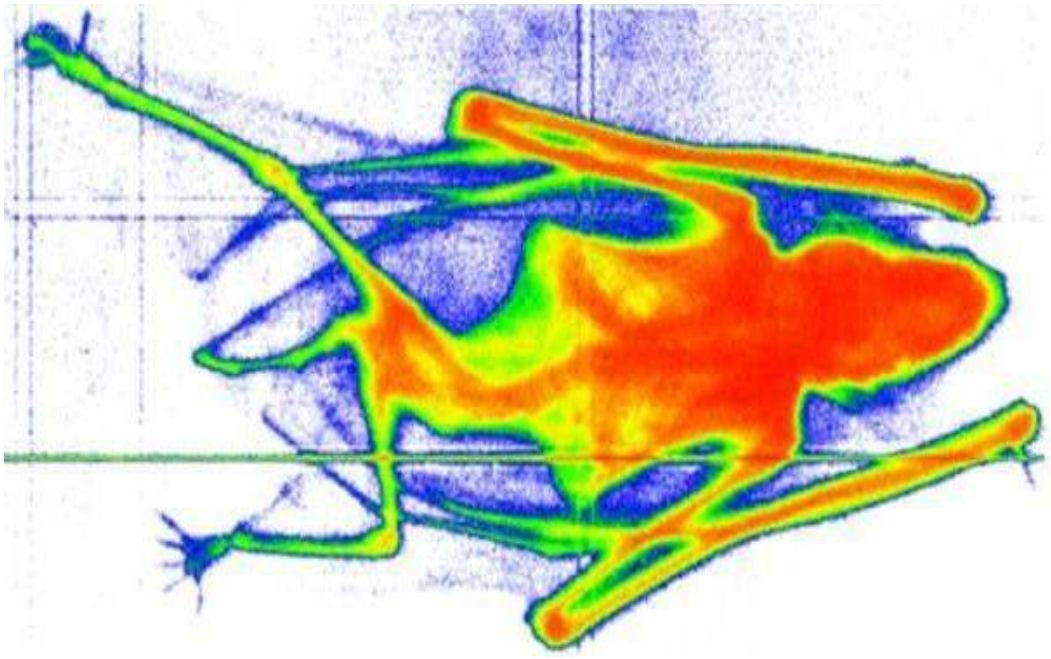

Figure 2.19: X-ray absorption radiography of a small mammal obtained with a two dimensional GEM detector [24].

3. Experimental Setup

The experimental setup used for this thesis consists of a gaseous chamber, where a double GEM cascade is assembled, with in and out gas outlets and feedthroughs for high-voltage biasing and data acquisition. An X-ray tube was used as source of x-rays to irradiate the detector.

3.1. **Detector Setup**

The gaseous chamber is made of aluminium with a volume of $25 \times 25 \times 6\ cm^3$. Figure 3.1 shows two photographs of the chamber used. The chamber has an entrance window made of aluminized Mylar™ foil with a thickness of $25\ \mu m$ (Figure 3.1 a). Inside the detector, in a square geometry, 4 teflon pillars (Figure 3.1 b) support the frames containing the GEM structures as well as the readout and the metallic mesh frame responsible to define the drift region.

The GEMs are foils with an active area of $10 \times 10\ cm^2$ and a thickness of $100\ \mu m$. A double cascade configuration was used, immersed in a mixture of $Ar: CO_2\ (70:30)$. The detector was operated at atmospheric pressure and the gas mixture was continuously flowing through the detector at a flow of $5\ l/h$, supplied from a pressurized canister.

It will be shown that the use of non-standard $100\ \mu m$ thick GEMs, which have a two-fold thicker Kapton™ when compared to the most common foils, allowed the construction of a robust detector and decreased the probability of electrical discharge across the holes. With this configuration, three different regions appear (Figure 3.2). The drift region with 9 mm gap, the transfer region with 3 mm gap and the induction region with 6 mm.

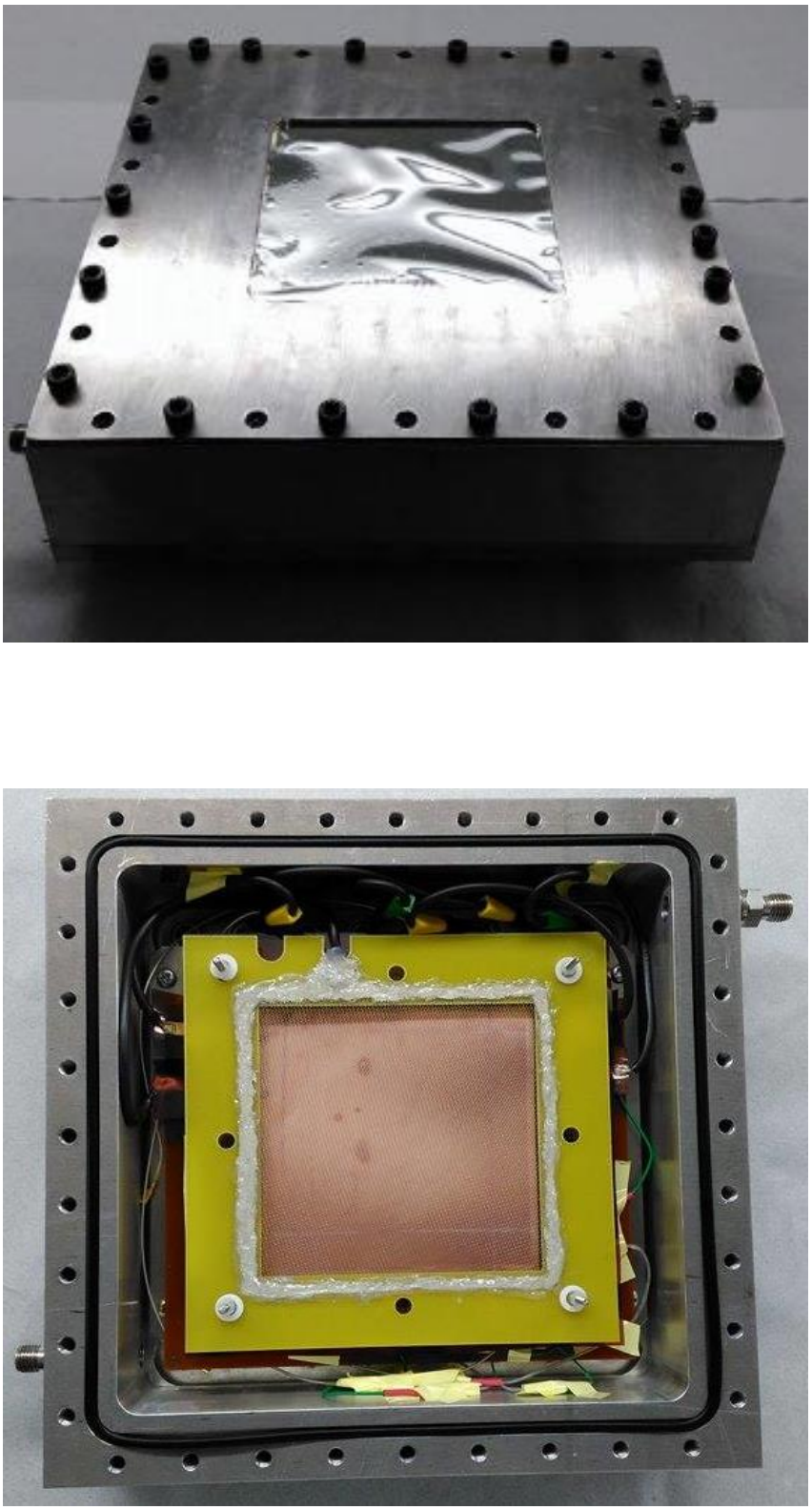

Figure 3.1: Images of the detector used in this experimental work. *a)* External view showing the window made of aluminized Mylar™ foil. *b)* Internal view of the detector with the GEMs assembled.

The drift grid, the top and bottom electrodes of the two GEMs were biased independently using VME based HV supplies from CAEN (model V6521HN). The electrodes are biased through a low pass RC filter.

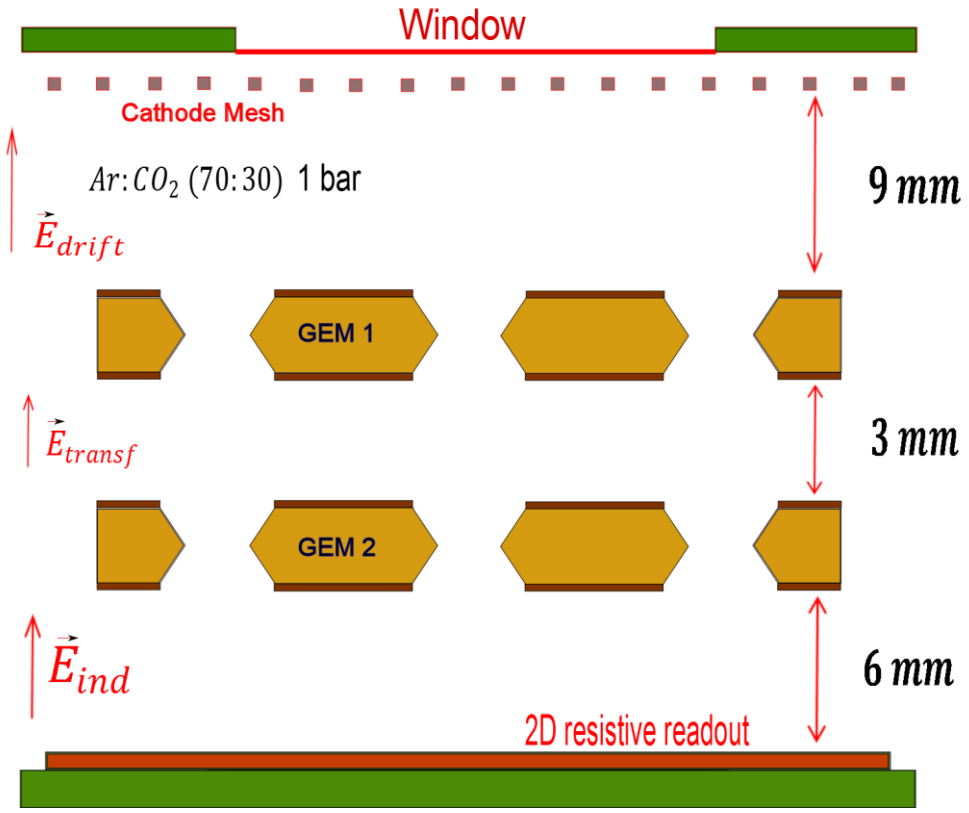

Figure 3.2: Scheme of the detector, with the drift, transfer and induction gaps. The gas mixture was $Ar:CO_2$ (70:30) at 1 bar.

The drift grid and each of the GEM electrodes were polarized with negative voltages while the 2D resistive readout was at ground potential. The low pass RC filters were used to filter the ripple of the power supply, reducing the electronic noise. They consist of a 15 $M\Omega$ resistor in parallel with a 1 nF capacitor connected to the ground.

The X-rays used in the image reconstruction were selected during the data analysis and had energies between 10 and 25 keV. An X-ray tube equipped with a copper anode was the responsible of producing these X-rays (see section 3.1.1.). The tube was placed at a distance of 1 m from the detector window and was attenuated by a aluminium sheet of 1.5 mm. Several masks made with stainless steel or lead were used to project the images in the detector.

3.1.1. X-ray Tube

As it was described in section 2.1, there are two ways for the production of X-rays. One is by the emission of *characteristic x-rays*. Here, the accelerated electrons collide with an electron in the innermost layer of an atom which results in its ejection from the orbital it occupies. The hole created by the ejected electron is immediately filled by the neighbouring electrons. This electron transition is followed by the emission of an X-ray with a very precise energy, characteristic of the atomic shell from which the electron was ejected. The other process where X-rays are produced is by *bremsstrahlung emission*. Here, the electromagnetic radiation (X-rays) is produced by a sudden slowing down or deflection of electrons passing through matter in the vicinity of the strong electric fields of atomic nuclei (Coulomb interaction). A portion or all of electron kinetic energy is lost and is converted into a photon (radiative loss), thus satisfying the law of energy conservation.

Figure 3.3 shows the main components of an X-ray tube with a tungsten anode. The *X-ray tube* provides an environment where X-rays are produced via bremsstrahlung and characteristic radiation mechanisms.

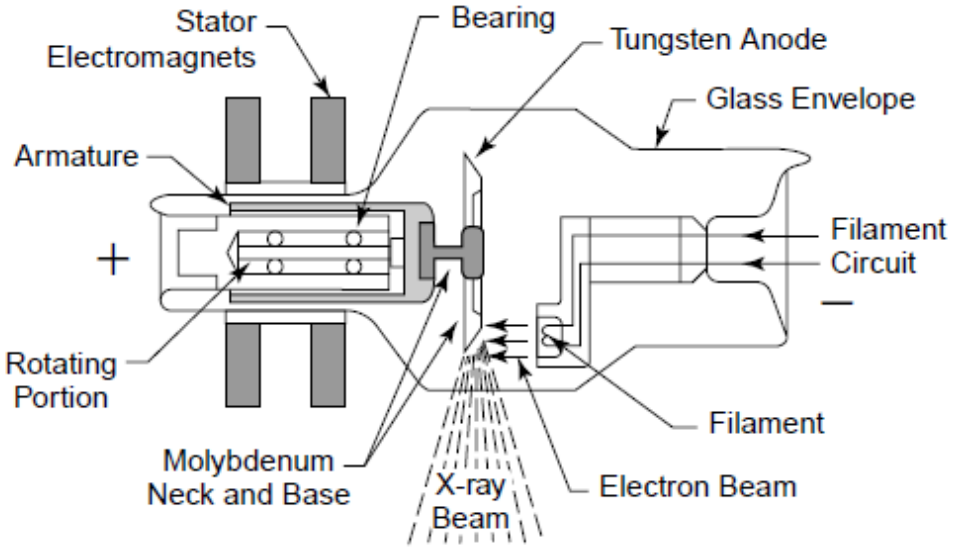

Figure 3.3: Major components of an X-ray tube.

The electrons responsible for the production of X-rays are released from a heated filament (cathode) and accelerated in vacuum towards the target (anode) by an electrostatic field supplied by the X-ray generator. This electron stream is the *tube current*. Usually the cathode is made of *tungsten* or *copper*. The filament is heated by an electric current of a few miliamperes and the electrons are released via *thermionic emission*. Since the X-rays are emitted from the target in all directions, a set of collimators turn them in a useful beam of X-rays. The intensity and energy distribution of these X-rays are influenced by the potential difference (voltage) between the filament and target. More detailed information can be found in the references [32][34].

Figure 3.4: Picture of the X-ray tube and X-ray generator used in this work.

3.2. **Electronic Calibration**

In order to obtain the absolute gain of the detector the electronic chain had to be calibrated. For that task a calibrated capacitor was used instead of the detector itself. The electronic chain setup used for calibration is depicted in figure 3.5.

As it can be seen in figure 3.5, the anode readout signal follows the sequence: pre-amplifier, amplifier and finally the multichannel analyser (MCA). If we irradiate the detector with a mono-energetic x-ray source, such as the ^{55}Fe, the amplitude of the output pulses will have a normal distribution centred at a mean value that is proportional to the energy of the x-rays emitted by the ^{55}Fe, radioactive source. The output given by the MCA is a pulse height distribution whose major feature is a Gaussian peak. Its mean value is used in the charge gain calibration. Thus, the effective gain charge (detector gain) is determined by the MCA channel and by the charge deposited in the detector by the incident radiation.

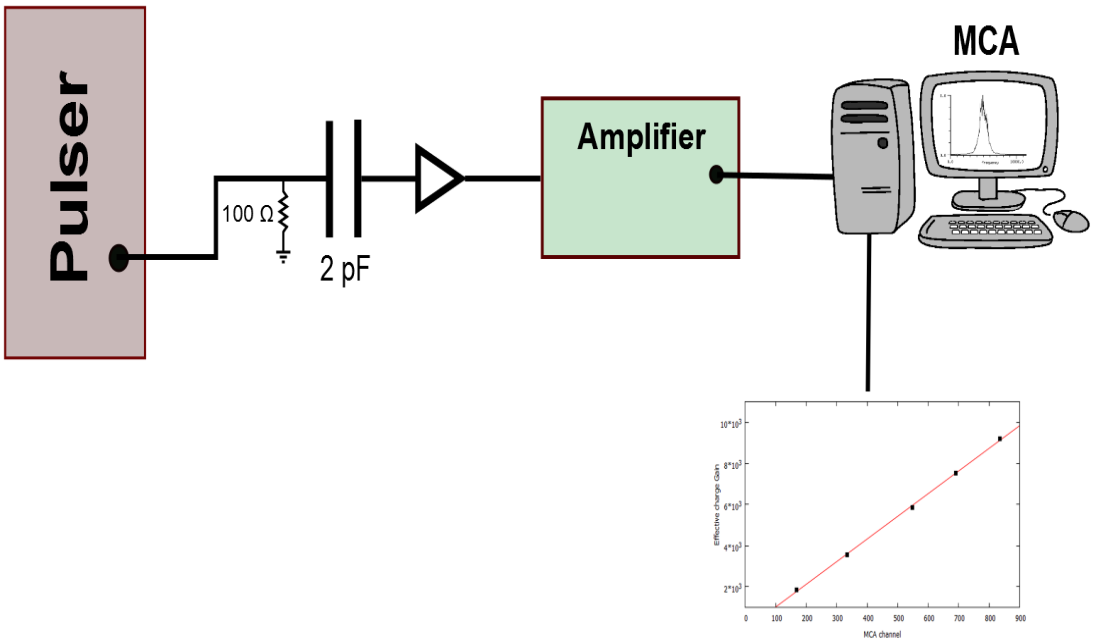

Figure 3.5: Scheme of the charge calibration setup. Consists of a precise pulse generator BNC model PB-4, a 2 pF capacitor, a Camberra model 2006 preamplifier, a TENNELEC TC 243 amplifier and a multichannel analyser Nucleus PCA II.

The calibrated capacitor ($C_0 = 2pF$) is connected to a BNC pulse generator (model PB-4) that produces an output signal with the following characteristics: rectangular pulses characterized by an amplitude V_i, rise time of 0,05 μs and a fall time of 100 μs. The charge induced in the capacitor by the pulser is given by the following equation:

$$Q_i = C_0 V_i \tag{3.1}$$

The charge signal from the capacitor is integrated by the preamplifier. The resulting Gaussian distribution in the MCA histogram has a very narrow peak corresponding to the input signal provided by the pulse generator for a given amplitude V_i. A calibration curve can be obtained by changing V_i and hence Q_i, according to equation 3.1. With this setup, keeping the settings of the electronic chain, it is possible to make a calibration curve, like the one shown in figure 3.6, with the relationship between the effective charge gain of the detector, $G_{detector}$, and the MCA channel.

The $N_{e_{total}}$ represents the total number of electrons collected at the anode readout, corresponding to the MCA channel of the centroid of the pulse height distribution.

The $N_{e_{total}}$ is given by:

$$N_{e_{total}} = \frac{Q_i}{e} = \frac{C_0}{e} V_i \tag{3.2}$$

where $\boldsymbol{e}$ is the electron charge (~$1{,}602 \times 10^{-19}$ coulombs).

The number of primary electrons, $N_{e_{X-ray}}$, produced by the X-ray interaction in the gas is given by:

$$N_{e_{X-ray}} = \frac{E}{W} \tag{3.3}$$

where E is the X-ray energy and W is the average energy necessary to create an electron-ion par.

The effective charge gain of the detector is given by:

$$G_{detector} = \frac{N_{e_{total}}}{N_{e_{X-ray}}} \tag{3.4}$$

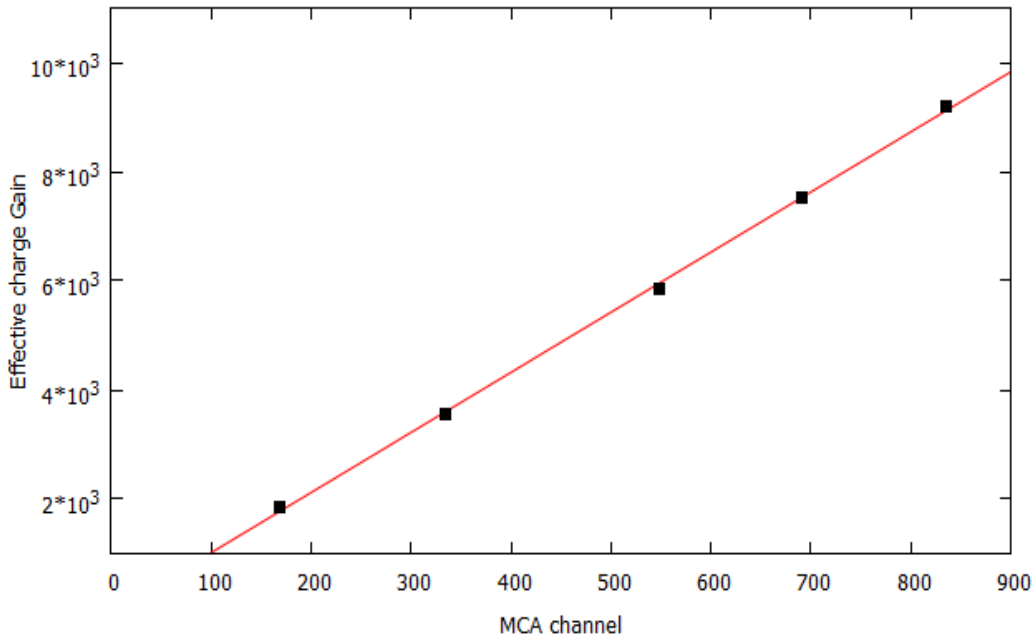

Figure 3.6: Calibration curve of the electronic chain. It is represented the effective charge gain (obtained by the equation 3.4) versus the MCA channel (centroid of the distribution obtained from the BNC pulses). A linear regression fit was made to the data (red line). The line has the parametric form: $y = mx + b$, where $m = 11{,}015$ is the slope of the line and $b = -83{,}448$ is the line's y-intercept.

According to the results exposed in figure 3.6, an equation, that states a calibration factor to calculate the detector gain, was defined:

$$G_{Detector} = m \times channel_{Det} + b$$

$$= 11{,}015 \times channel_{Det} - 83{,}448 \tag{3.5}$$

where $channel_{Det}$ corresponds to the centroid of the distributions obtained from X-ray pulses. The source of the X-rays used was the ^{55}Fe point source.

3.3. **Imaging System Setup**

3.3.1. The principle of imaging with the detector

Most of the imaging applications with MPGDs have made use of discrete channel readout. However this method requires the use of a complex electronic system due to the very large number of channels imposed. Whenever a spatial resolution of the order of mm is needed another method can be used. The method is the resistive charge division, that uses simple electronic readout and algorithms of center of mass to determine the position of the interaction. The charge readout electrode, with an area of $100 \times 100\ mm^2$, is composed by two layers of parallel strips at 400 µm pitch with 50 µm and 200 µm width for top and bottom layers, respectively, disposed orthogonally to each other. The strips of each layer are interconnected by a resistive line and the signals are collected from both ends. The signal that reaches each end is different as consequence of the resistive line (could be the same if the interaction takes place in the centre of the strip). This different amount of charge that reaches each side has information of the position of the interaction for each independent coordinate (dimension). In this work only four shaping/amplification channels were used which allowed to obtain information of the position and energy of each event produced in the detector.

The charge pulses, obtained on each of these four channels, are integrated by a charge sensitive preamplifier and digitized by a CAEN VME1724 digital pulse processor, where the shaping and amplification is done. In each channel, the amplitude and the time stamp of each pulse is logged. The data is then processed to reconstruct the image. First, the pulses that occur within a time window of a few ns are arranged in groups of four, one from each channel. When this time window is not respected, the pulses are automatically rejected. This first step outputs a collection of events with information in the coordinates x and y and, the energy and time (x, y, E, t). These events carry the necessary information required for the image reconstruction.

3.3.2. Resistive charge division

To make the resistive charge division, one resistive strip is placed along each spatial dimension. After the charge avalanche takes place, the final charge pulses are divided according to their position along each coordinate/strip. Their amplitude differences reveal where the interaction took place. Actually, the 2D readout consists in two sets of orthogonal strips with each one connected to a resistive line. Figure 3.7 illustrate the 2D readout setup used in the experimental work.

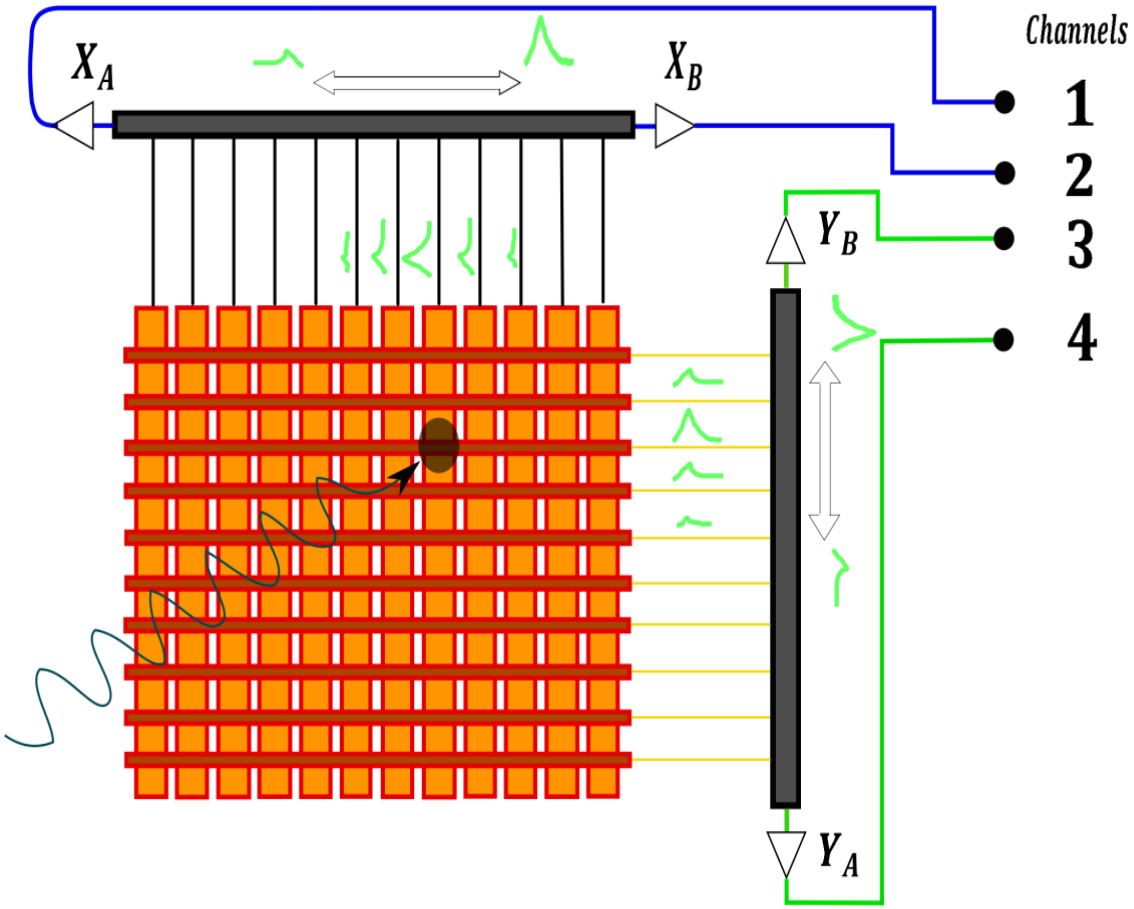

Figure 3.7: Schematic of the 2D readout with four channels connected to the end of each resistive line.

The collected charge is read from both ends of each resistive line and the interaction position can be determined according to the principle of the resistive charge division which results in the following equation:

$$y = L\frac{Y_L - Y_R}{Y_L + Y_R} \tag{3.6}$$

where y is the coordinate of interaction, L is half the length of the resistive strip, Y_R the signal amplitude from one of the edges of the resistive line and Y_L the signal amplitude of the other edge of the resistive strip.

To obtain the x-coordinate a similar equation is used. As illustrated in figure 3.7 this simple readout system requires only 4 channels to process the signals and therefore obtain the image.

3.3.3. Image characterization

There are some aspects that influence the *image quality* that need to be kept in mind. Limitations to the position resolution such as the signal-to-noise ratio and the photoelectron range will be referenced. Some concepts for characterisation of the image quality will also be described.

3.3.3.1. The signal-to-noise ratio

The resistive charge division described in section 3.3.2 works connecting each end of a resistive strip to a preamplifier. A very interesting work [35] shows the relation between the position resolution and the signal-to-noise ratio. The schematic diagram of the charge division is shown in figure 3.8. If the input impedance of the preamplifiers is not considered, the ratio of the charge collected at the end of the strips is just the inverse ratio of the strip resistances between the avalanche point and the strip ends.

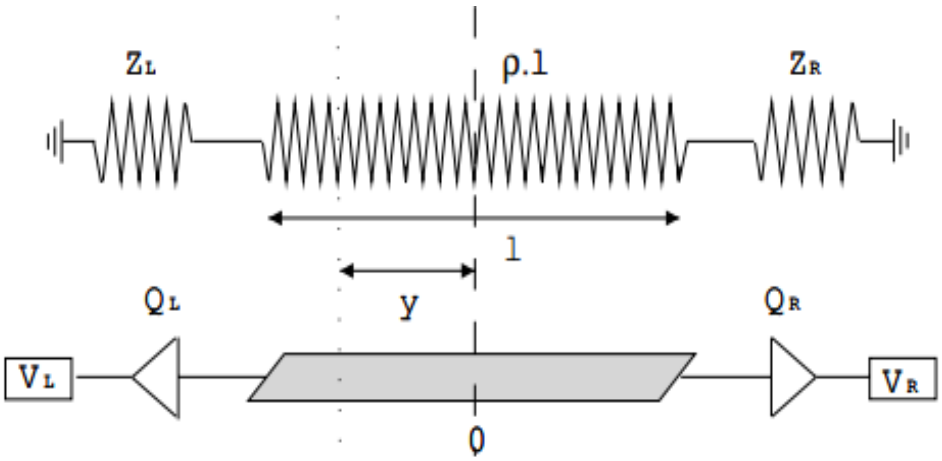

Figure 3.8: Schematic diagram of the resistive charge division [35].

When the input impedances Z_R (right) and Z_L (left) of the preamplifiers are taken in account, the ratio between the charge collected in both ends (Q_R and Q_L) is given by:

$$\frac{Q_L}{Q_R} = \frac{\left(\frac{l}{2}-y\right)\rho+Z_R}{\left(\frac{l}{2}+y\right)\rho+Z_L} \tag{3.7}$$

where l is the length of the resistive strip, y is the distance from the avalanche to the middle of the strip and ρ its resistivity. The particle position can be obtained by the following relationship:

$$y = \frac{l}{2}\left(\frac{Q_R-Q_L}{Q_R+Q_L}\right) + \frac{l}{R}\left(\frac{Q_R Z_R-Q_L Z_L}{Q_R+Q_L}\right) \tag{3.8}$$

assuming that the preamplifiers have the same input impedance Z, the last equation can be rewritten:

$$y = \frac{l}{2}\left(\frac{Q_R-Q_L}{Q_R+Q_L}\right)\left(1+\frac{2Z}{R}\right) \tag{3.9}$$

where R is the total resistance of the resistive strip.

Once the equation for the position is derived, the position resolution can be seen as its standard deviation. An error propagation study allows evaluating how the position resolution is influenced by the noise of the system:

$$\sigma_y = \sqrt{\left(\frac{\partial y}{\partial Q_L}\sigma_{Q_L}\right)^2 + \left(\frac{\partial y}{\partial Q_R}\sigma_{Q_R}\right)^2} \tag{3.10}$$

Assuming that the equivalent noise charges are equal and not correlated, $\sigma_R = \sigma_L = \sigma_Q$, follows that:

$$\sigma_y = l\frac{\sqrt{{Q_R}^2+{Q_L}^2}}{(Q_R+Q_L)^2}\left(1+\frac{2Z}{R}\right)\sigma_Q \tag{3.11}$$

Equation 3.11 can be reduced since at the centre of the resistive strip $Q_R = Q_L = Q$:

$$\sigma_y = \frac{l}{2\sqrt{2}}\left(1+\frac{2Z}{R}\right)\frac{\sigma_Q}{Q} \tag{3.12}$$

Assigning Q to the charge signal S and σ_Q to the noise N, equation 3.12 can be rewritten as:

$$\sigma_y = \frac{l}{2\sqrt{2}}\left(1+\frac{2Z}{R}\right)\frac{N}{S} \tag{3.13}$$

Equation 3.13 shows that the position resolution improves for higher signal-to-noise ratio and for higher resistance.

3.3.3.2. Photoelectron range

In the X-ray energy range used in this work, the primary absorption mechanism of an X-ray with a gas atom is the photoelectric effect. When those X-rays with energy E_x hit an argon atom and interacts with an electron shell with binding energy E_b, the result is the emission of a photoelectron of energy $E_x - E_b$. The atom is left in an excited state, and an electron from an outer shell immediately occupies the empty space originated by the emitted photoelectron. This process has as consequence the release of energy either by emitting a characteristic X-ray or by emitting an Auger electron. Since for Argon most of the electrons removed are from the K-shell whose binding energy is $\sim 3.2\ keV$, both characteristic X-ray and Auger electron have the same energy given by: $E_K - E_L \sim 2.7\ keV$.

The photoelectron and Auger electron thermalize due to the collisions with the other atoms of the gas. The range they reach limits the best resolution possible with the gas. Figure 3.9 shows the relation between the electron (photoelectron and Auger electron) energies and the X-ray energy.

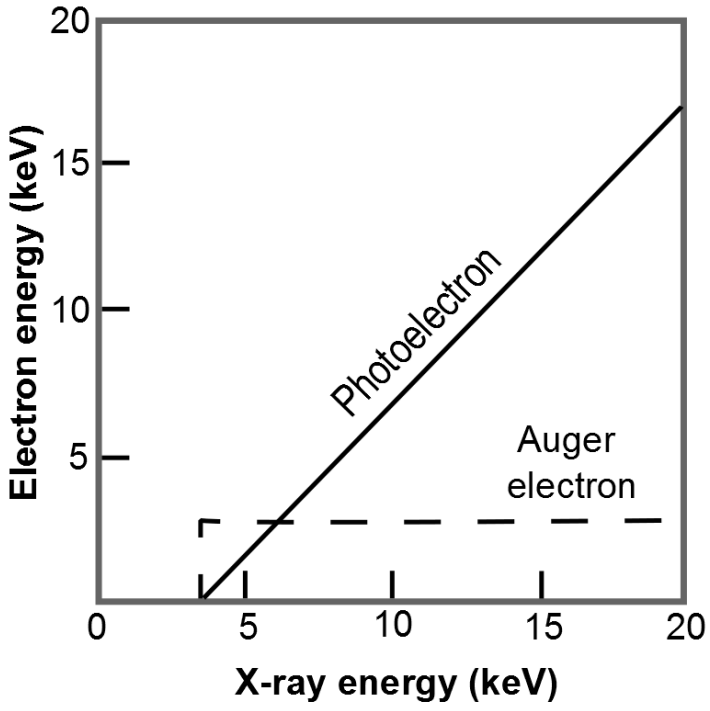

Figure 3.9: Photoelectron and Auger electron energies in argon as a function of X-ray energy. Intersection happens at 6 keV. Data adapted from [36].

The range of the photoelectron and Auger electron is proportional to their energy and longer ranges degrade the position resolution.

Some references [36][37] showed that, at a pressure of 1 bar, the best resolution achievable in argon is around $100\ \mu m$ for incident X-ray photons with an energy of 6 keV. This minimum value of the position resolution corresponds to a situation where the photoelectrons and the Auger electrons have the same energy (figure 3.9). Figure 3.10 shows the relation between the position resolution in argon and the energy of the incident X-ray.

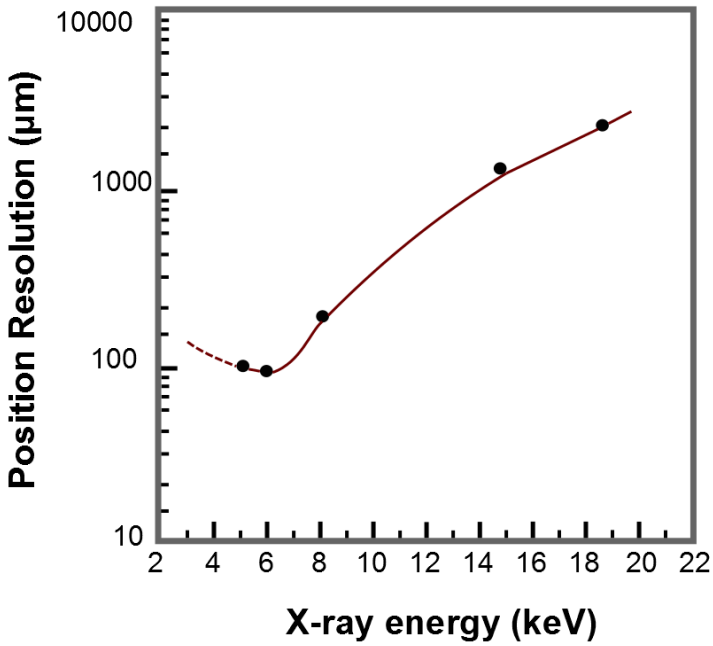

Figure 3.10: Position resolution (FWHM) in argon (1 bar) as function of the X-ray energy. The minimum reached is around $100\ \mu m$. Adapted from [37].

When one electron receives almost all the energy of the X-ray, it is known that there is a power law relationship between the position resolution and the energy of the X-ray. In the case of argon, figure 3.10 shows that the position resolution has a dependence with X-ray energy more complicated than just a simple power law. For X-ray energies between the $5.4\ keV$ and $6\ keV$ the Auger electron acquires most of the available energy and there is a slight improvement of the resolution as the energy increases. When both photoelectron and Auger electron have the same energy, the

minimum position resolution ($100\ \mu m$) is achieved. At higher energies it is the photoelectron that acquires most of the X-ray energy. Here, the position resolution gets worse and above $10\ keV$ acquires the already mentioned power law dependence with the X-ray energy.

In a more recent work, the study of the position resolution limits in pure noble gaseous detectors for X-ray energies from 1 to 60 keV was made [31]. In that work it is shown the influence of the atomic shells and the detector dimensions on the intrinsic position resolution of the noble gas used. The study and discussion of the position resolution is an important subject for gas-filled radiation detectors. However these studies focus on the device influence rather than the gas influence. In fact it isn't only the photoelectron range that contributes to the position resolution. Energy loss mechanisms that happen during the photoelectron drift also contribute. The fluorescence photon interaction within the detector volume is other process that can contribute to the degradation of the position resolution, since its absorption will shift the charge distribution centroid. Figure 3.11 shows the position resolutions calculated for different gases as function of the X-ray photon energy by using a simulation program based on Monte Carlo simulations.

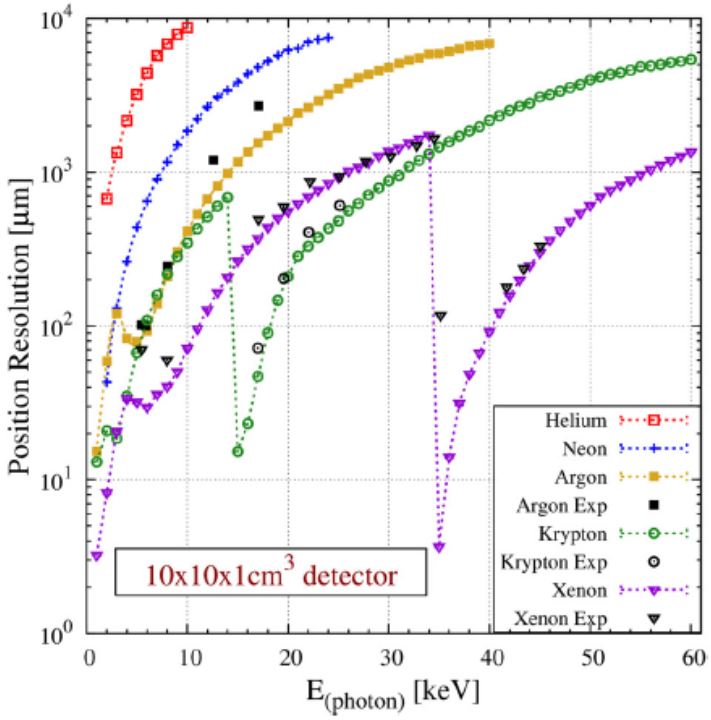

Figure 3.11: Position resolution as a function of the photon energy for a $10 \times 10 \times 1\ cm^3$ detector [31].

For argon there is improvement of the position resolution after the K shell ($K_{Ar} \approx 3\ keV$). This happens because the inner shells have greater energy which results in lower energetic photoelectrons. Lower energetic photoelectrons result in a lower charge spread. Beside this, a characteristic fluorescence photon is emitted due to the atom rearrangement. This characteristic X-ray can be absorbed elsewhere in the detector giving rise to a new primary electron cloud that will change the initial position detection. However, since the detector have a finite geometry, high energetic photoelectrons (Kr and Xe K fluorescence) will contribute more to escape peaks than to interactions with the gas, which results in better position resolution. But in the case where the fluorescent photons have less energy, for example in the Ar K shell, it can't be considered that the position resolution will be dominated by the photoelectron range. The interaction of the fluorescence photons has also to be taken in account.

3.3.3.3. Concepts on imaging

In order to evaluate its performance, the quality of an imaging system must be quantified. The quality of the image depends fundamentally on the ability of the imaging system to reproduce each single point in the object. In this subsection a short review of some concepts regarding the characterization of an image is made. Concepts such as dynamic range, point spread function, line spread function, edge spread function and modulation spread function are briefly described. This subsection does not intend to be a profound review of this subjects since there is plentiful literature on it [32][33][34].

Dynamic range

Images are defined as intensity maps. In this perspective, *dynamic range* corresponds to the number of intensity levels that compose the intensity map. Some images have a high dynamic range and it is possible to manipulate the distribution of the shades of colours or grey making possible to distinguish some characteristics among objects with low contrast. The highest possible dynamic range is required for imaging systems. However, a compromise must be taken in account since high dynamic range usually implies high radiation doses.

Point Spread Function

In real world it is impossible to obtain perfect images of an object. One way to evaluate the image quality is to place two structures close together, usually two infinitely small holes, and see how well they can be distinguished in the image. The result will be a 2D intensity distribution of the photons which passed through the holes and reached the imaging system readout. In an ideal world, the result of the intensity map would be two well defined delta functions. However, this is not the case because of the point spread function (PSF) of the imaging system.

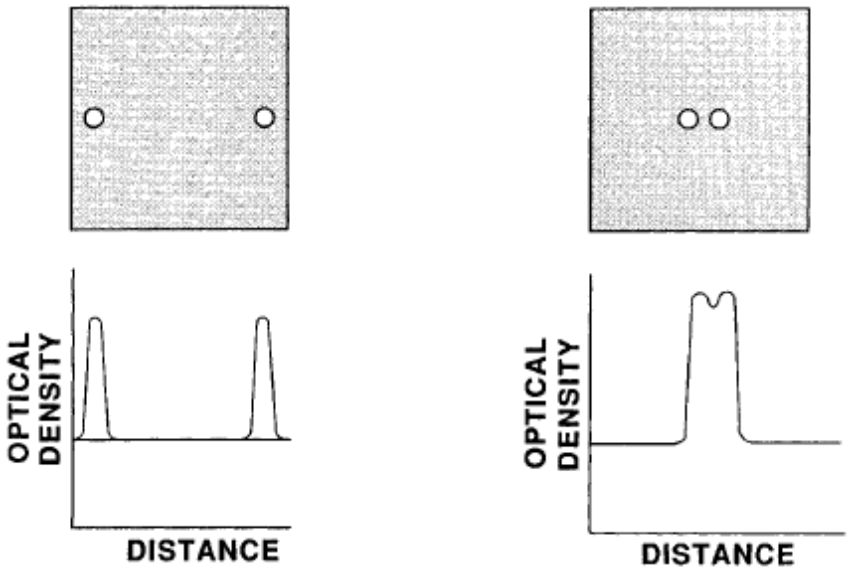

Figure 3.12: Point spread function of two infinite small holes. a) The holes are widely separated and can be seen as separate entities in the image. b) The holes are brought together and the two PSFs start to overlap.

As it can be seen from figure 3.12 a), when the point holes are widely separated, they are easily distinguishable in the image. However, when they are moved closer, at some distance the contrast decreases and the point spread functions start to overlap untill the two holes are seen as just one single wider hole (figure 3.12 b)).The position resolution of the system is usually quantified by this distance.

Line Spread Function

Since the counting can become very low for small irradiated areas (pinpoint holes transmit very few photons), the use of very small holes is not practical. Besides this, the approach is impossible in an experimental point of view because there is no such thing as infinitesimally small holes. This is the reason why lines are used instead of point holes. The great advantage of using lines is that they transmit many more X-rays than holes and therefore the information in the image is not restricted by the number of photons used to characterize it. The image of a thin slit is composed of all the PFSs along its direction. The *line spread function (LSF)* is a one dimensional representation of the two-dimensional point spread function (PSF). The width of the slit must be sufficiently narrow in a way that its finite extent does not contribute significantly to the width of the output image. A LSF is derived by integrating the point spread function along sections parallel to the direction of the line. This works because a line image is the summation of an infinite number of image points along its length. Since the line spread function is composed of overlapping point spread functions, the PSF can be mathematically derived from the LSF.

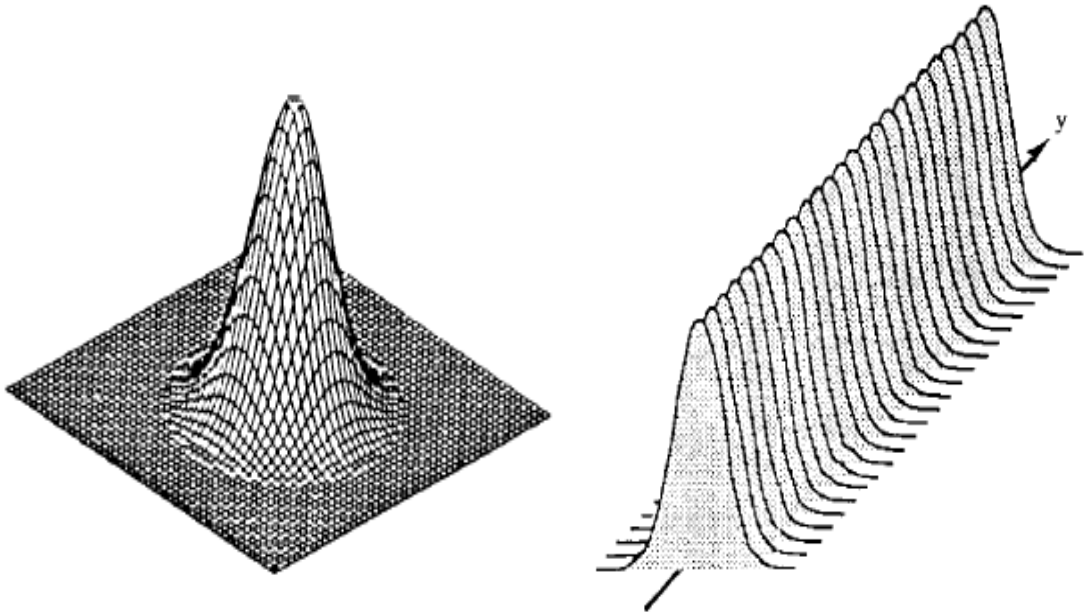

Figure 3.13: The Point spread function PSF (x, y) and the Line spread function LSF. The LSF is the PSF integrated over one dimension.

The image of the slit is the convolution of the LSF with a rectangle with a width of the slit. The Gaussian curve becomes more pronounced when the width of the slit decreases. It is possible to deconvolute the contribution of the finite width slit. Reference [39] does a very pertinent empirical study about this subject. An empirical equation that allows determining the position resolution of the system using a slit with a finite width is derived. This equation allows calculating the resolution of the system for slits with a width of the order of the resolution of the system:

$$\sigma_x = w_s \sqrt[3]{\left(\frac{w_i}{w_s}\right)^3 - 1} \tag{3.14}$$

where σ_x is the width of the LSF, w_s is the width of the slit and w_i is the width of the image. One limit can now be stated. In a situation where the width of the slit is so small that results in an image much larger than the slit, the position resolution of the imaging system is approximately given by the width of the image.

The usefulness of the concepts of point spread function and line spread function is the characterization of an imaging system by reproducing simple objects such as points and lines.

Edge Spread Function

Another concept that can be useful to characterize the imaging system is the *edge spread function* (ESF).The edge response is a concept that is closely related to the line response. The line spread function is the response of the system to a thin line across the image. Similarly, the edge spread function is the response of the system to a sharp edge (discontinuity). This is other alternative to determine the spatial resolution of the detector. In this approach the imaging system is presented with a source that transmits radiation on one side of the edge and blocks completely on the other side. Since a line is the derivative of an edge, the LSF is the first derivative of the ESF.

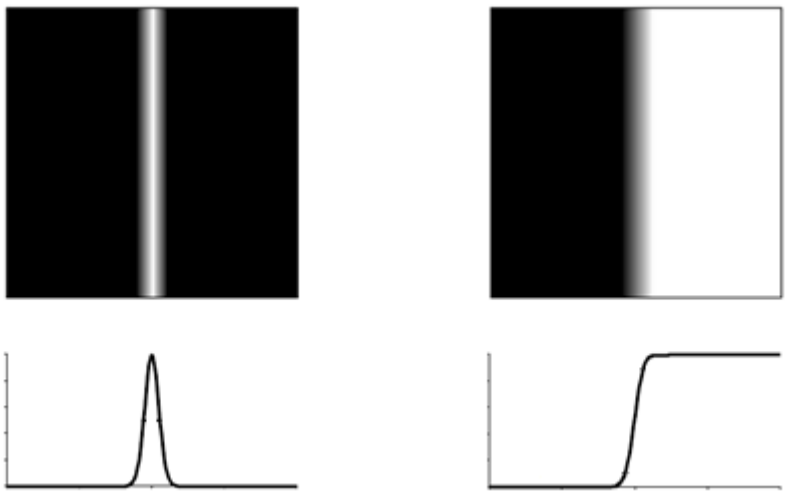

Figure 3.14: *a)* Line spread function and *b)* Edge spread function. The LSF is the first derivative of the ESF. Adapted from [38].

The intensity distribution of an ideal edge should be a step function where the maximum intensity would correspond to the illuminated area and zero intensity to the non-irradiated region. Figure 3.14 b) shows that such step is smoothed due to the finite spatial resolution of the imaging system. The width of the LSF, obtained by differentiating the ESF, is the spatial resolution of the imaging system.

Modulation transfer function

Another approach to determine the resolution characteristics of imaging systems is to use a test object containing a sequence of slits separated by X-ray opaque structures with different spatial frequencies. If the slits are imaged, there will be a difference in the obtained intensities. The intensity obtained for the wider slits (lower special frequencies) will be higher than for the thinner ones (higher special frequencies). This means that larger objects have higher contrast than smaller objects. Figure 3.15 shows the mask with different slit sizes used in this work.

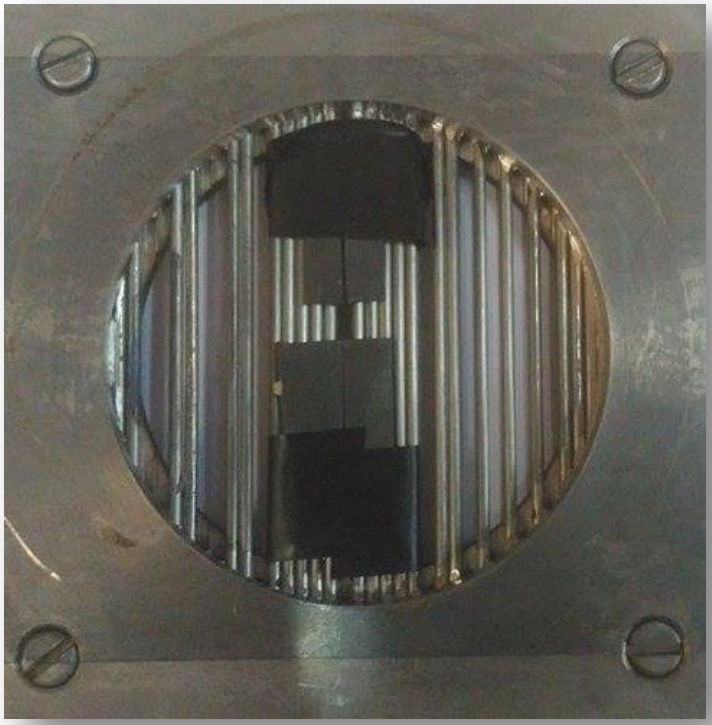

Figure 3.15: Mask with an array of slits. The profile of an image of the slits was used to measure the contrast.

Another concept can now be defined. *Modulation Transfer function* or MTF is another tool used to describe the performance of an imaging system. The MTF is, as the name suggests, a measure of the transfer of modulation (or contrast) from the object to the image. In other words, it measures how well the imaging system reproduces detail from the object to the image as a function of the spatial frequencies. The spatial frequencies are usually defined in line pairs per millimetre, lp/mm.

To quantify the contrast (modulation) the following equation can be used:

$$C(\upsilon) = \frac{I' - I}{I'} \tag{3.15}$$

In order to quantify the contrast is chosen two different regions of the image where the spatial frequencies υ are known. Their intensities are related according to equation 3.15. With increasing spatial frequency the contrast of slit profiles decreases. This can

be seen in figure 3.16 where the difference between contrast in the object and the contrast in the image is illustrated.

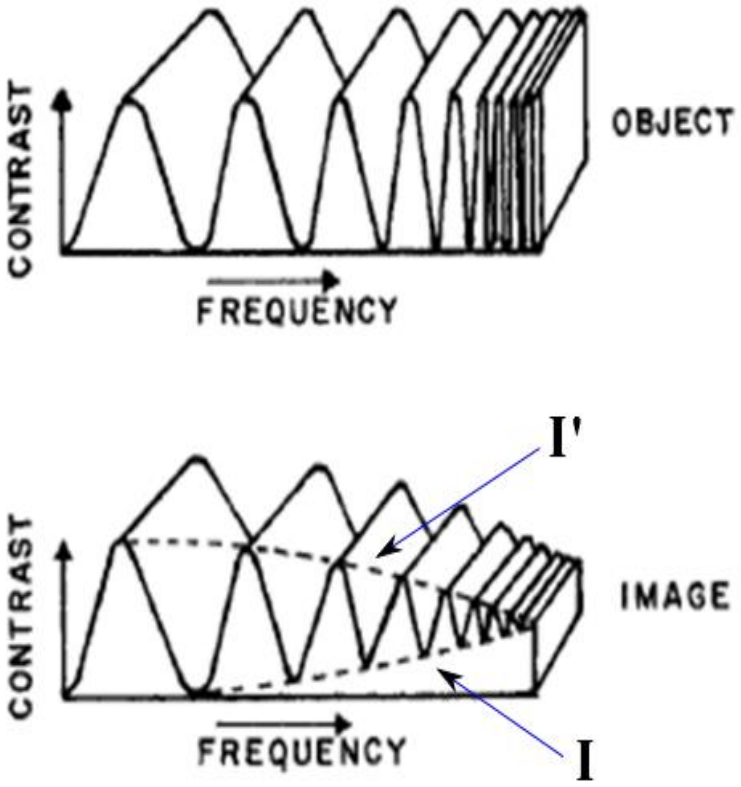

Figure 3.16: Contrast in the object versus Contrast in the image. The contrast of the slits decreases with the spatial frequency [32].

Since the image system blurs the edges it is impossible to preserve the square-wave pattern. For widely separated slits the blurring is not dramatic. But as the slits are brought together it becomes harder to distinguish them in the image. As it was said before, in the regions of higher spatial frequencies, the images of the slits begin to overlap each other and the contrast decreases. Figure 3.16 shows exactly this behaviour.

Figure 3.17 shows some experimental results that were published in one of the publications done under this master degree thesis [30]. The image presented corresponds to the mask with an array of slits shown in figure 3.15.

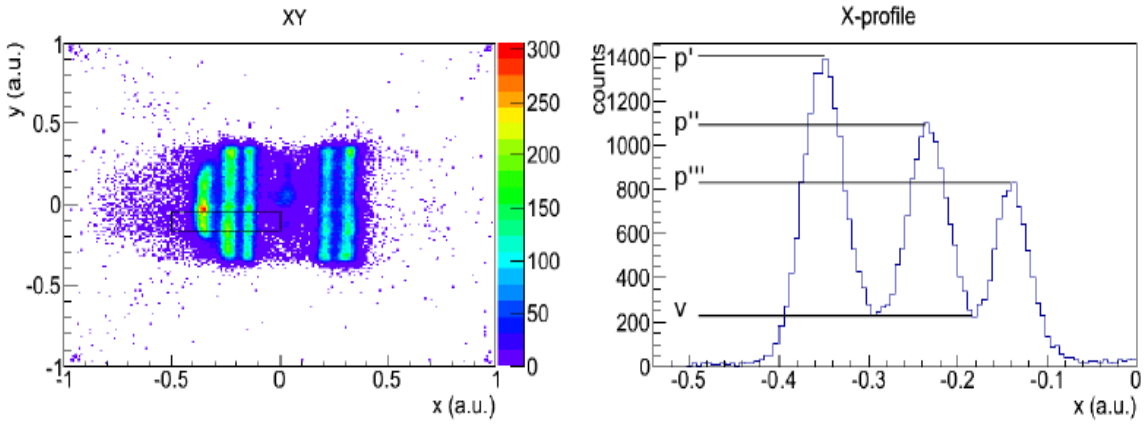

Figure 3.17: Example of the determination of the contrast. The image on the right is the profile of the region marked in the image of the left [30].

To measure the contrast, the profile of an image of the slits was made and an equation similar to the equation 3.15 was used:

$$C = \frac{p-v}{p} \tag{3.16}$$

where p is the average height of the three peaks and v the average height of the two valleys. The procedure of this simple method is illustrated in figure 3.17.

The *modulation transfer function* (MTF) is obtained by plotting the contrast as a function of the spatial frequency. This is equivalent to represent the intensity map in the spatial frequency space, instead of the coordinates space. Therefore, the modulation transfer function can also be obtained by applying the *Fourier transform* (FT) to the LSF.

For this work, algorithms of the Discrete Fourier Transform from CERN's ROOT framework libraries were used. A more detailed discussion about the FT can be found in the reference [40].

Figure 3.18 shows the behaviour of the MTF for different LSFs.

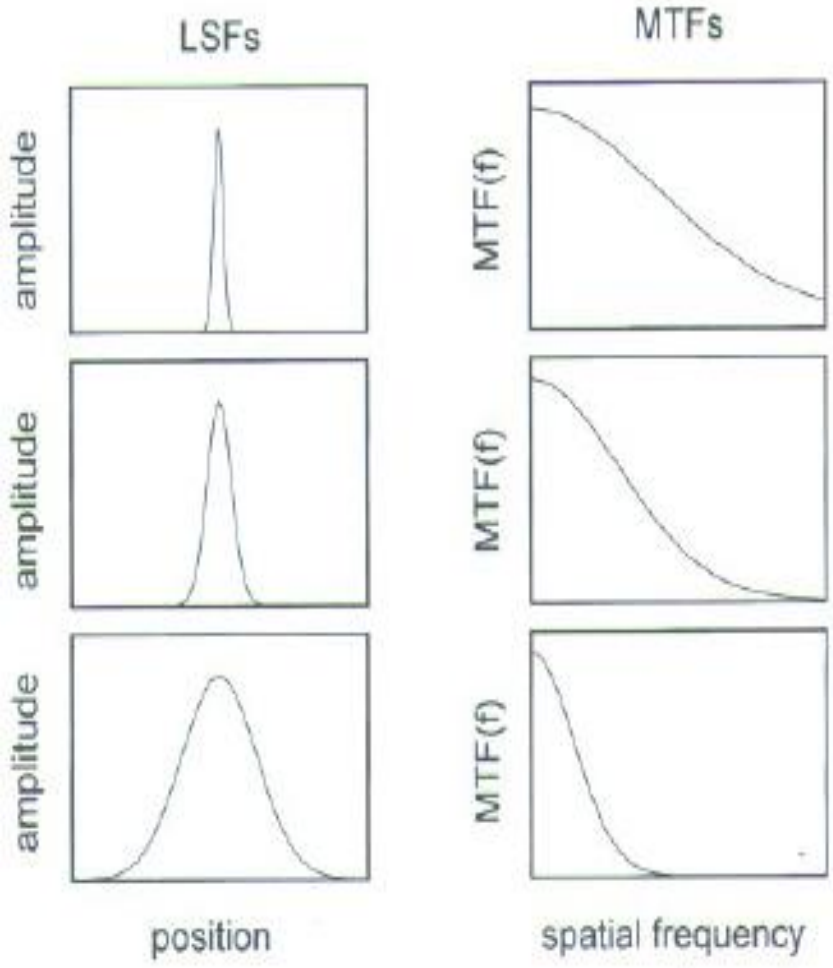

Figure 3.18: As the line spread function gets broader the corresponding MTFs become smaller for the same spatial frequency [33].

4. Results

This section reports the results obtained during the present studies accompanied by relevant discussions. As described in the preceding section, two different readout geometries were used. The associated results are discussed separately below where a comparison of the readout capabilities is carried out.

4.1. **Single and Double GEM characterization**

The performance of the detector in $Ar:CO_2$ $(70:30)$ atmosphere was studied as function of the voltage across the GEMs holes (V_{GEM}). In addition, the optimization of the drift, transfer and induction fields was carried out. All the subsequent imaging results obtained were based on this optimization study.

It is well known that an increase of V_{GEM} value leads to an exponential increase of the charge gain. This behavior was verified for both single and double GEM configurations. As expected the double GEM configuration allowed to reach higher charge gains. The absolute charge gain was calculated using the calibration method described in section 3.2. An ^{55}Fe radioactive source was used and the mean energy required to produce an electron-ion pair in a particular gas was obtained from the literature. For $Ar:CO_2$ $(70:30)$, $w = 28\ eV$ at $5.9\ keV$ was assumed [4].

In the experimental study described in this section the detector drift gap was irradiated perpendicularly to the detector plane by an $5.9\ keV$ ^{55}Fe X-ray source. The drift electrode and the GEM electrodes were operated with negative voltage with respect to the 2D resistive readout board that was held close to ground potential. The *charge gain* and the *energy resolution* were studied for both single and double GEM cascade configurations.

In the double GEM configuration the 2D readout was electrically connected to an Ortec preamplifier (model 142PC). The preamplifier output was then fed into a Tennelec shaping amplifier (model TC 243) with shaping time constants adjusted to $0.5\mu s$. The output of the shaping amplifier was finally fed into an Ortec multichannel

analyser. For the single GEM configuration the apparatus is almost identical. The difference is that the induction gap is now made between the bottom of the first GEM and the top of the second one. Thus, the Ortec preamplifier is connected to the top electrode of the second GEM.

The pulse-height distributions obtained by the MCA were fitted to Gaussian distributions in order to obtain the necessary parameters for the charge gain and energy resolution. The charge gain was obtained from the Gaussian centroid and the energy resolution from the full width at half maximum (FWHM).

4.1.1. Optimization of the Drift, Transfer and Induction Field

For the measurements described here, a detector assembly having two cascaded GEM foils between a drift electrode and a 2D resistive readout was used, as shown schematically in Figure 4.2. The drift electrode, that is made of $80\,\mu m$ diameter stainless-steel wire with $900\,\mu m$ spacing, is mounted above the GEM to establish the drift region, characterized by a drift field E_d. The gap separating the two GEM foils is referred as the transfer region. The last gap, the one between the bottom of the second GEM and the resistive readout, is the induction/collection region.

The primary electrons, resulting from the absorption of the incident X-rays in the drift region, are multiplied in avalanche inside the GEM holes due to intense fields. Due to the influence of the transfer field E_t they are transferred to the next GEM where they undergo another multiplication process. Finally they are collected by the readout due to the induction field.

The optimization of the drift, transfer and induction fields was made aiming to achieve the best overall results and represents a balance between these fields. This study was made for both 5×5 and $10 \times 10\ cm^2$ readouts, since the gaps used are different. All measurements presented on this section were done by irradiating the detector with 5.9 keV ^{55}Fe X-ray source. Figure 4.1 *a)* and 4.1 *b)* schematize the two detector setups used. The setup shown in Figure 4.1 *a)* was used to investigate single GEM performance by collecting charge at the top surface of the lower GEM. It consisted in a $50 \times 50\,mm^2$ readout where the drift electrode was mounted $11\,mm$ above the first GEM and the gaps of the transfer and the induction regions were $2.8\,mm$ and $2\,mm$

respectively. For the detector using the $100 \times 100\ mm^2$ readout, the gaps of the drift, transfer and induction regions were 9 mm, $3mm$ and 6 mm respectively.

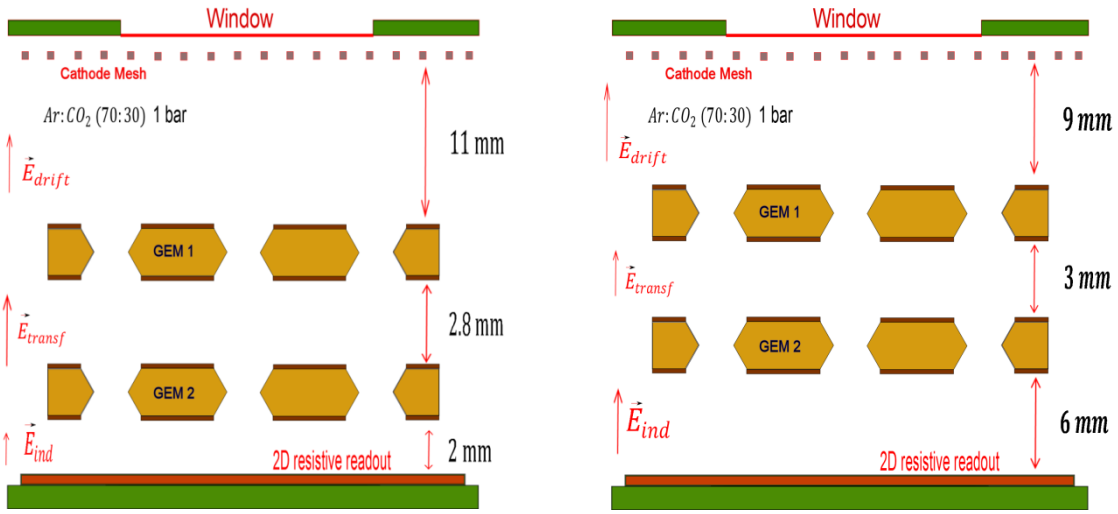

Figure 4.1: Schemes of the detector, with the drift, transfer and induction gaps: *a)* scheme of the detector using the 50×50 mm^2 readout *b)* scheme of the detector using the 100×100 mm^2 readout.

➢ Drift Field

An optimum drift field is required to transport the primary electrons created within the drift region towards the GEM multiplication stages and their subsequent collection by the readout structures. A low drift field results in signal loss due to recombination of the primary electrons and ions. If the drift field is set too high some of the primary electrons may be lost due to inefficient focusing into the holes of the first GEM in the cascade. In this part of the study the gain and the X-ray energy resolution (for 5.9 keV X-rays) were investigated as a function of the drift field for a fixed Δ_{GEM} and induction field, E_{ind}. Figure 4.2 *a)* shows the typical behaviour of these parameters using single GEM with increasing drift fields with $\Delta_{GEM} = 680V$ and $E_{ind} = 2.33\ kVcm^{-1}bar^{-1}$. Figure 4.2 *b)* shows results for the double GEM configuration with $\Delta_{GEM_{both}} = 580V$, $E_{transf} = 3.57\ kVcm^{-1}bar^{-1}$ and $E_{ind} = 1.83\ kVcm^{-1}bar^{-1}$.

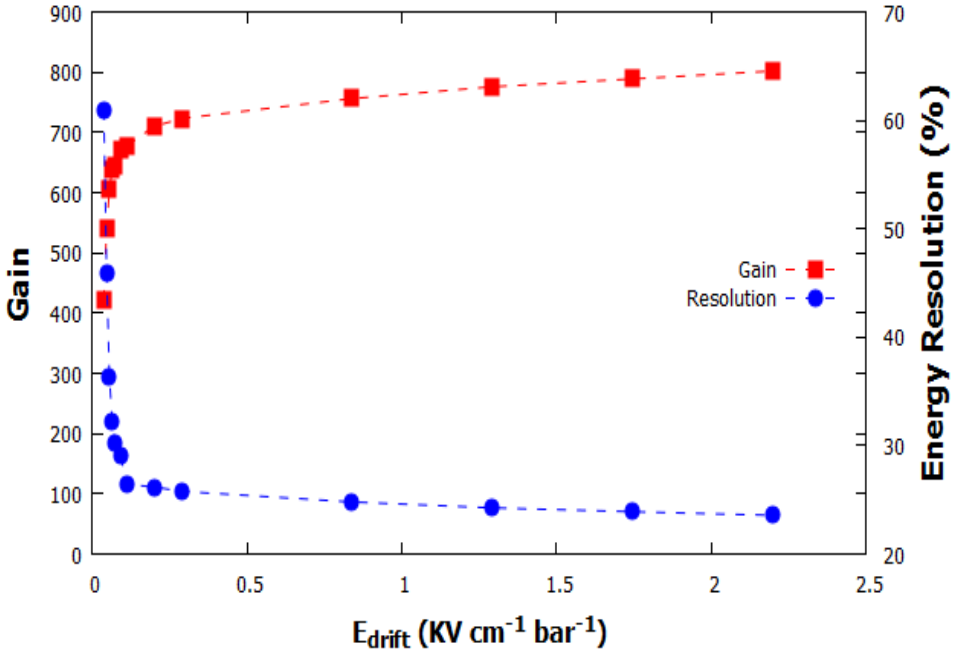

Figure 4.2 *a)*: Graph showing gain and energy resolution as a function of the electric field in the drift region for the single GEM configuration. $\Delta_{GEM} = 680V$ and $E_{ind} = 2.33\ kVcm^{-1}bar^{-1}$.

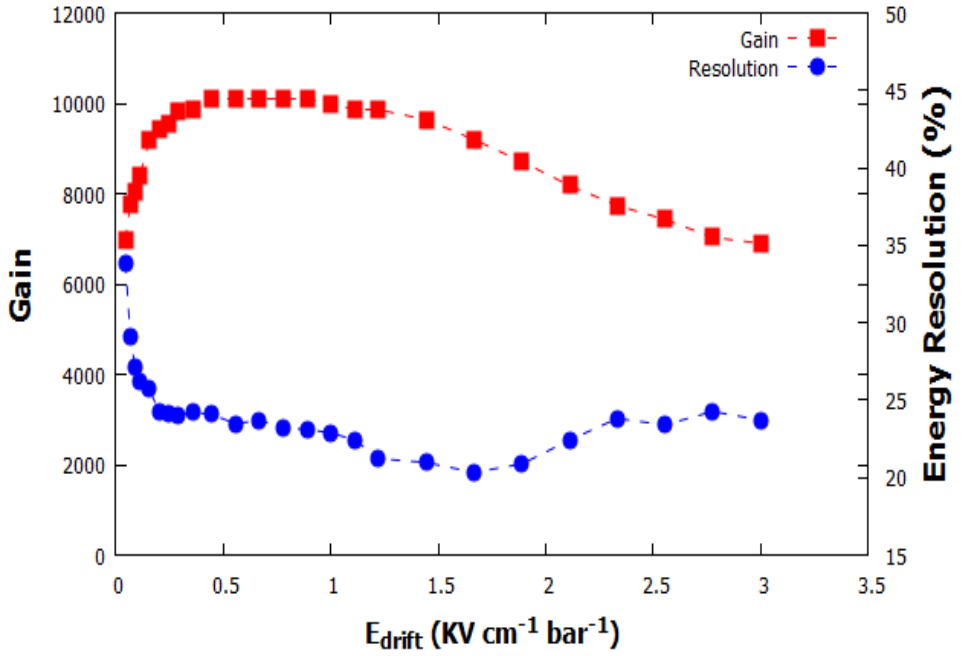

Figure 4.2 *b)*: Graph showing gain and energy resolution as a function of the drift field for the double GEM configuration. $\Delta_{GEM_{1,2}} = 580V$, $E_{transf} = 3.57kVcm^{-1}\ bar^{-1}$ and $E_{ind} = 1.83\ kVcm^{-1}bar^{-1}$.

As can be seen from figure 4.2, the gain is lower for low drift fields and also drops significantly for higher drift fields accompanied by deterioration of the X-ray energy resolution. At the lower drift fields, the gain reductions are attributed to electron losses via recombination processes. At the higher fields some drift field lines begin to terminate at the top of GEM 1 causing electrons to impinge there, resulting in the observed gain reduction.

Comparing the behaviour of the gain and energy resolution as a function of the electric drift field for the single and double GEM configurations, a slight difference is clearly visible. In the case of the single GEM the plateau zone is extended to higher values of E_{drift}, while for double GEM configuration the gain starts to drop at $E_{drift} \approx 1.5 \quad kVcm^{-1}bar^{-1}$. The reason for a gain drop as the drift field increases has already been explained above. For the double GEM configuration the gain drop starts at lower drift fields (at $1.5\, kVcm^{-1}bar^{-1}$) than in the single GEM configuration. An explanation for this behaviour may be due to a high E_{transf} used in the second setup (see Transfer Field Optimization below).

Reference [42] does a very interesting study about the operating properties of detectors based on GEMs. Figure 4.3 shows the variation of the relative transparency as a function of drift field for different Δ_{GEM} values.

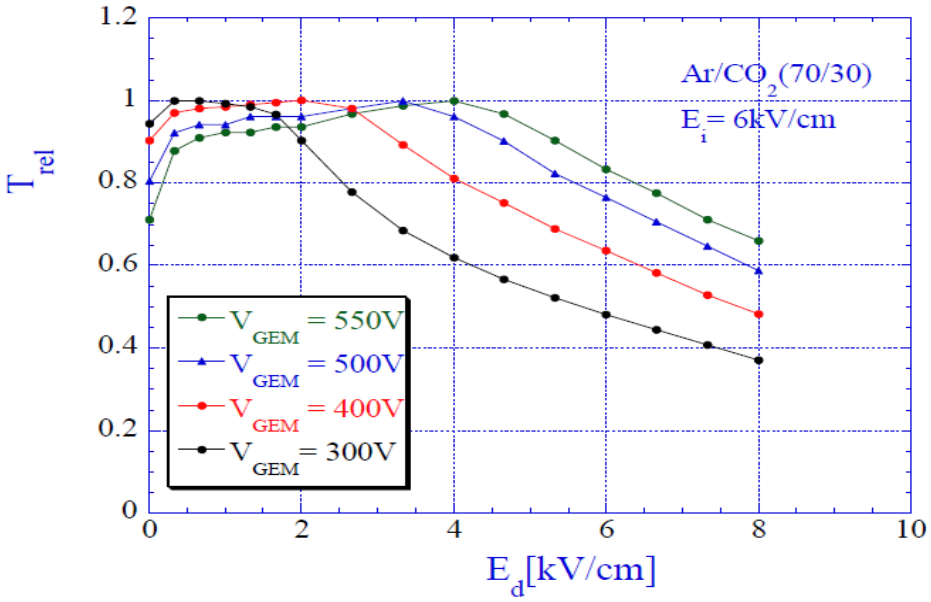

Figure 4.3: Relative transparency T_{rel} as a function of the drift field for $\Delta_{GEM} = 300V$, $\Delta_{GEM} = 400V$, $\Delta_{GEM} = 500V$ and $\Delta_{GEM} = 550V$. The induction field was fixed at $E_{ind} = 6\, kVcm^{-1}bar^{-1}$ [42].

Another reference [43] does also a study of the relative transparency as a function of drift field for a number of different induction fields, E_{ind}. Both figure 4.3 and reference [43] allowed to conclude that the plateau (region of optimum electron transparency) is unaffected by altering the induction field. Actually, the plateau is extended by applying higher voltages across the GEM holes. These results and the different Δ_{GEM} GEM we have used, explain the differences found on both graphs of figure 4.2.

➢ Transfer Field

In a double GEM configuration, the gap separating these two stages is the transfer region. This region can also be pictured as the drift region for the second GEM in the cascade.

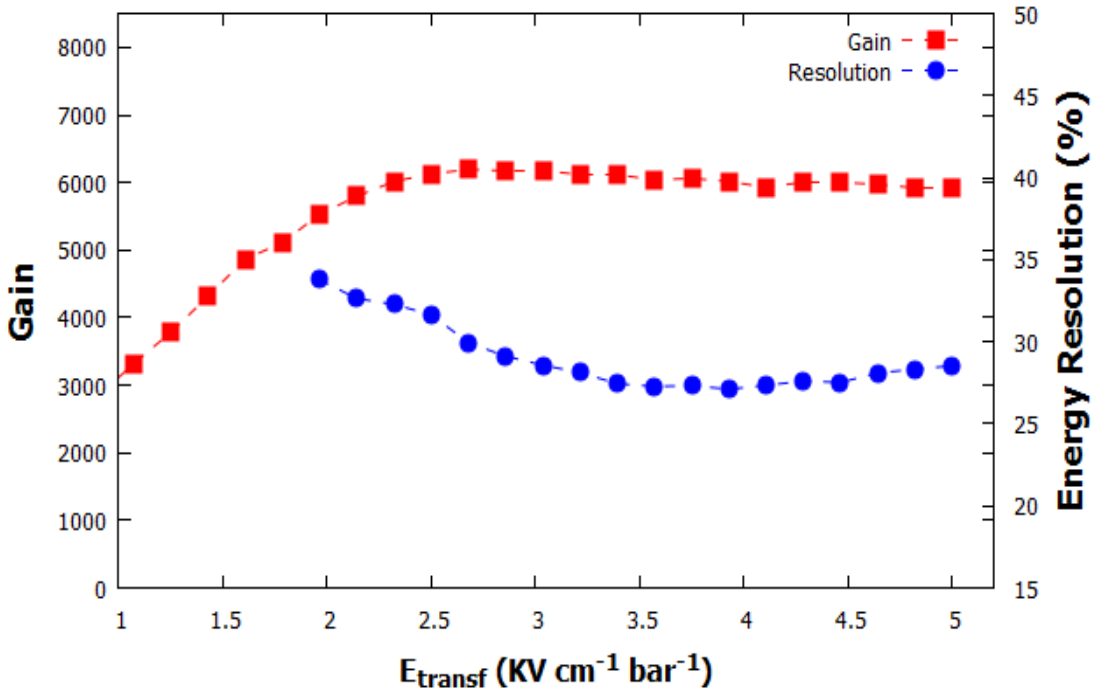

Figure 4.4: Variation of the gain and energy resolution versus the electric field in the transfer region with: $\Delta_{GEM_{both}} = 580V$, $E_{drift} = 0.77\ kVcm^{-1}bar^{-1}$ and $E_{ind} = 1.83\ kVcm^{-1}bar^{-1}$.

Figure 4.4 shows the curve behaviour of the gain and energy resolution as a function of the transfer field. The transfer gap can be seen as an induction gap from the perspective of the first GEM and as a drift gap from the perspective of the second GEM. Therefore, the variation of the signal amplitude with the electric field is a convolution of the variation of the drift field for the second GEM and an induction field for the first GEM. For lower fields, the efficiency of extraction of electrons from the holes of the first GEM increases, as the collection in the holes of the second GEM also increases. At certain point, the collection in the second GEM starts decreasing as in the study of the drift field, but the extraction from the first GEM keeps increasing (see next section). These two processes compete giving origin to a plateau.

➢ Induction Field

For a fixed drift and transfer field, electrons amplified in the second GEM holes are shared between the bottom electrode of the GEM and the 2D readout. Figure 4.5 shows the dependence of the effective gain upon the variation of the induction field, E_{induc}, for $\Delta_{GEM} = 560V$ while keeping the drift and transfer fields constant at $0.74\ kVcm^{-1}bar^{-1}$ and $1.87\ kVcm^{-1}bar^{-1}$, respectively. The variation of energy resolution for the range $E_{induc} = 0.5\ kVcm^{-1}bar^{-1}$ to $2.7\ kVcm^{-1}bar^{-1}$ is also showed. The results exposed in the figure illustrates the importance of optimising the induction field, since there is a clearly gain increase with increasing induction fields.

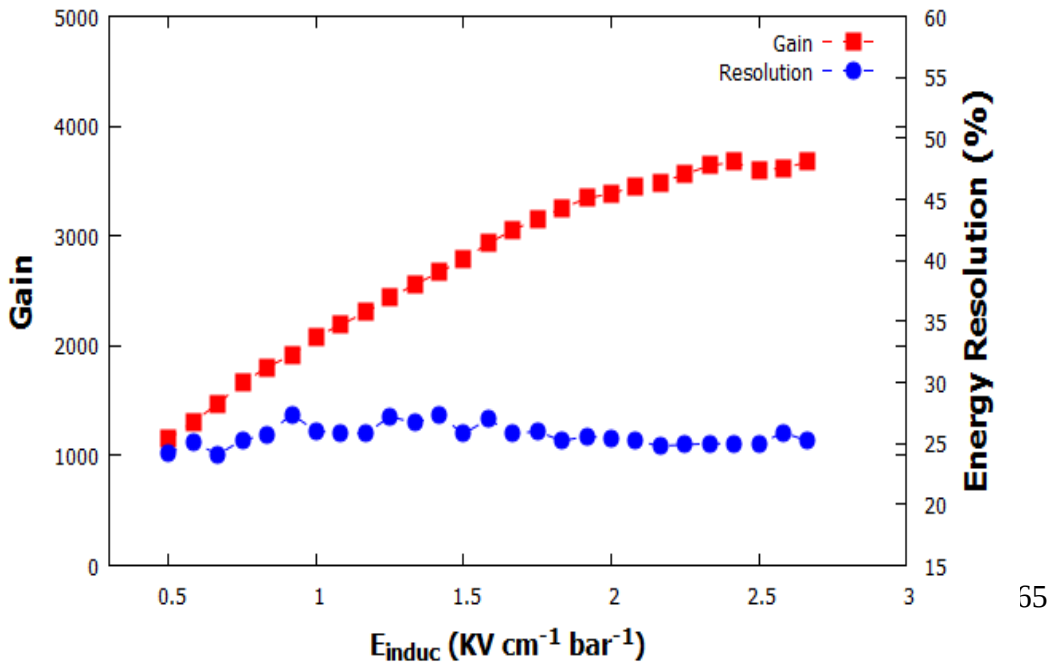

Figure 4.5: Gain versus induction field. The data was obtained considering the following parameters: $\Delta_{GEM} = 560V$, $E_{drift} = 0.74\ kVcm^{-1}bar^{-1}$ and $E_{transf} = 1.87\ kVcm^{-1}bar^{-1}$.

For the induction field range explored in this work, the effective gain increases almost linearly with the induction field. This means that the extraction of the electrons from the holes of the GEM is increasing. Above a certain value, the slope of the distribution is reduced, although the signal amplitude keeps rising. This is because some of the field lines do not start inside the GEM holes, but at the bottom surface of the GEM. These lines do not contribute to the extraction of the electrons from the holes. As a result, the amplitude of the signal keeps rising, but not as fast as when all the field lines start in the holes. For induction fields higher than $8\ kVcm^{-1}$ [44], parallel plate multiplication begins in the induction field which contributes to unstable gains.

4.1.2. Charge Gain and Energy Resolution

The effective gain and the X-ray energy resolutions were examined as a function of the voltage differences applied across the GEM holes, ΔV_{GEM}, by comparing the pulse height with that of a known charge pulse from a calibrated capacitor (see section 3.2). The drift field, E_{drift}, was maintained at approximately 1.4 $kVcm^{-1}bar^{-1}$. Figure 4.6 and 4.7 show the results obtained for the single and double GEM configuration, respectively.

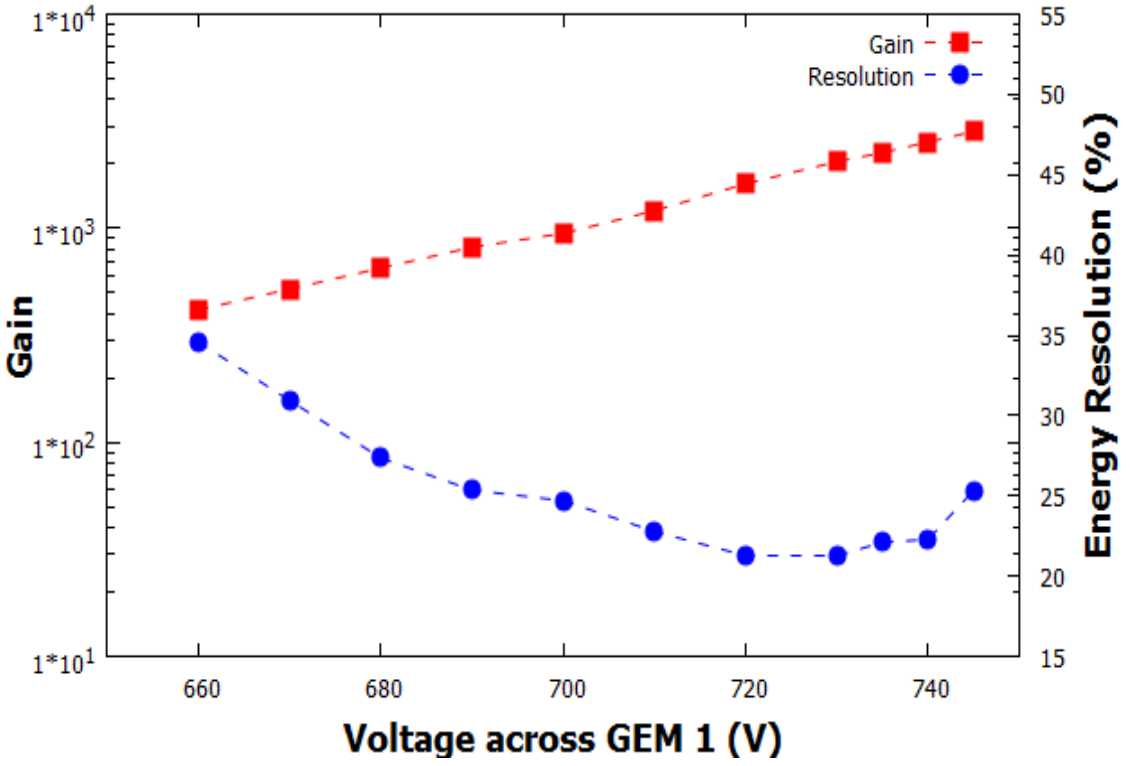

Figure 4.6: Variation of charge gain and energy resolution of a single GEM as a function of the voltage applied across the GEM holes, ΔV_{GEM}. The induction field E_{ind} was set at 5 $kVcm^{-1}bar^{-1}$ and the drift field E_{drift} at 1.4 $kVcm^{-1}bar^{-1}$.

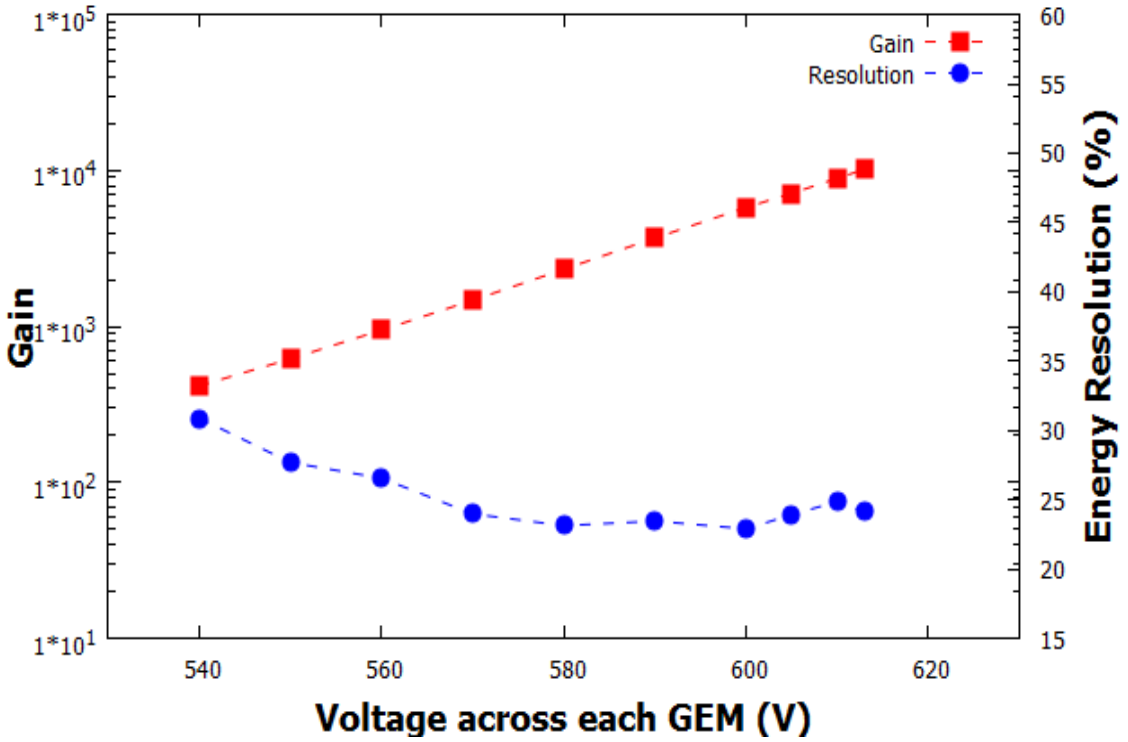

Figure 4.7: Variation of the charge gain and energy resolution for the double GEM configuration as a function of the voltage applied across the GEM holes, ΔV_{GEM}. The transfer field E_{transf} and induction field E_{ind} was set at 3.6 $kVcm^{-1}bar^{-1}$ and 2.5 $kVcm^{-1}bar^{-1}$, respectively whilst the drift field E_{drift} was at 1.4 $kVcm^{-1}bar^{-1}$

The performance of the detector was studied operating in argon and carbon dioxide (70/30%) atmosphere. For the single GEM (S-GEM) charge gain calculations, the drift and induction fields (1.4 kV/cm and 5 kV/cm, respectively) were kept constant while the voltage between the electrodes of the first GEM was gradually increased. An identical study was done to the double GEM (D-GEM). Here the drift, transfer and induction fields (1.4 kV/cm, 3.6 kV/cm and 2.5 kV/cm, respectively) were kept constant while the voltage across both GEMs was gradually increased. When the biasing voltages were too high, near the eminence of discharges, the measurements were stopped. Under these conditions the charge gain and the energy resolution were measured and plotted as seen in figs 4.5 and 4.6.

A charge gain of 3×10^3 and of 1×10^4 was achieved at stable operation for both single and double GEM configurations respectively, with best values of energy

resolution around 22 % FWHM. In S-GEM configuration for the charge gain measurements as a function of ΔV_{GEM} , the maximum GEM values applied before the onset of discharges was around $750\ V$ across the GEM, while the electric field applied to the induction was $5\ kV/cm$. In D-GEM configuration the maximum voltage reached across the GEM electrodes before the discharges was around $615\ V$. Both charge gain curves have the same expected exponential behaviour, typical of a proportional avalanche process.

The energy resolution of any gaseous detector is given by:

$$\frac{\Delta E}{E} = 2.35\left[\frac{w(F+b)}{E}\right]^{1/2} \tag{4.1}$$

where w is the average energy needed to create an ion-pair, F is the Fano factor, b is the avalanche electron multiplication variance and E is the incident X-ray energy. Typically, the value of F is approximately, 0.2 whereas the b factor is around 0.5. From this information, the best energy resolution from an ideal gaseous counter is approximately 13.6% FWHM for 5.89 keV X-rays. However, due to the imperfections in the detector construction as well as gas impurities, the best resolution is seldom achieved.

Figure 4.6 and 4.7 has also represented information about the energy resolution. The energy resolution is calculated from the Full Width at Half Maximum ($FWHM$) of the pulse-height distribution divided by the respective centroid (E_0):

$$E_{resol} = \frac{FWHM}{E_0} \tag{4.2}$$

The energy resolution was calculated for the conditions established for the charge gain measurements. Figure 4.8 *a)* shows the typical pulse-height distribution for the 5.9 keV Mn K_α line of a ^{55}Fe radioactive source where the argon escape peak is also visible. Figure 4.1 *b)* shows the detailed Gaussian fit.

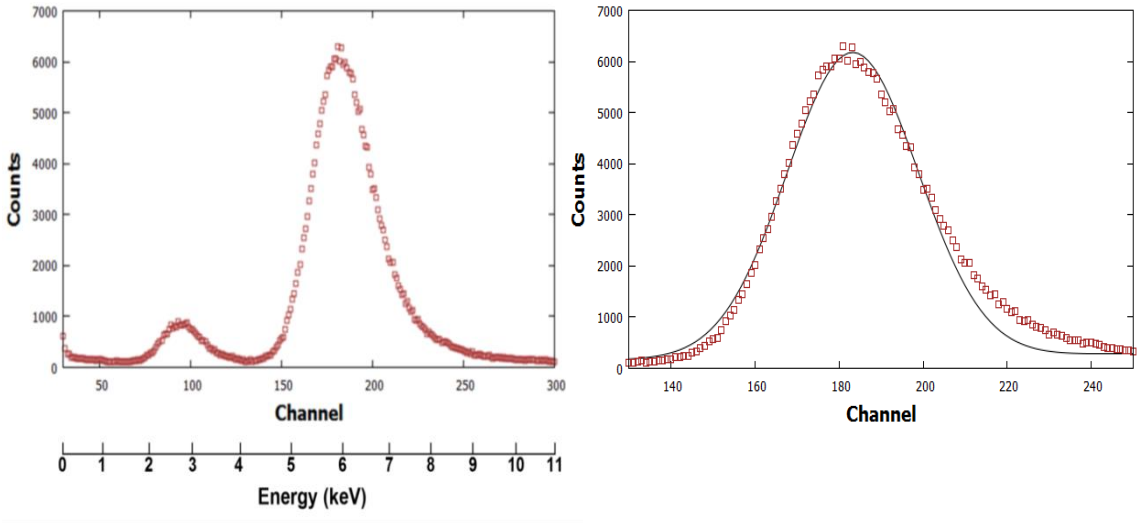

Figure 4.8: *a)* Typical pulse-height distribution for the 5.9 keV X-rays from a ^{55}Fe radioactive source. The argon escape peak is also presented (~3 keV). *b)* Gaussian fit done to the data to calculate the gain and energy resolution. Charge gain of 3×10^3 with energy resolution of 22 % was achieved.

In order to compare the gain curves of the 100 μm thick GEM in single and double mode with the 50 μm "standard" GEM ones, figure 4.9 also includes data of the gain response with 50 μm GEM taken from reference [44].

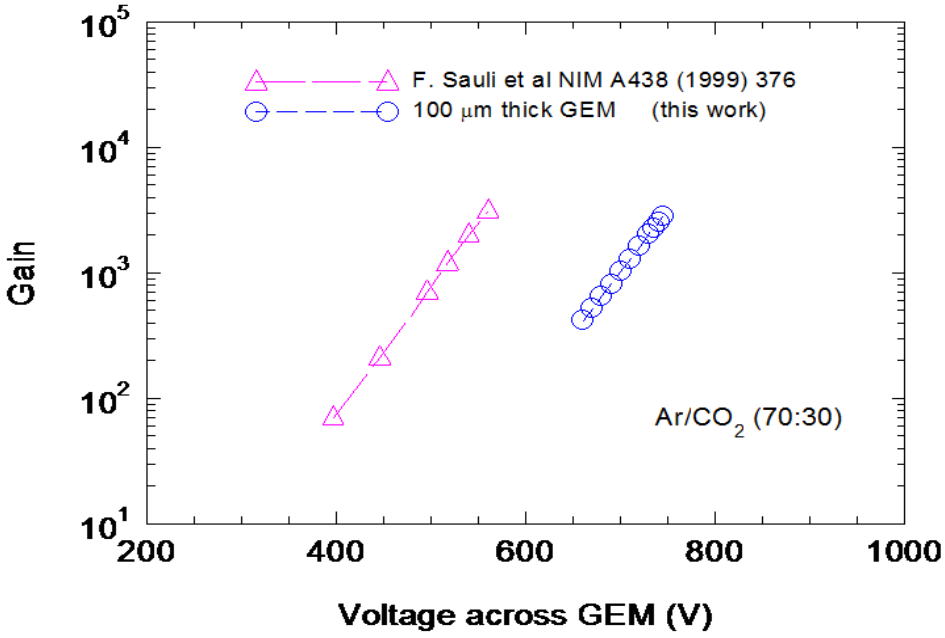

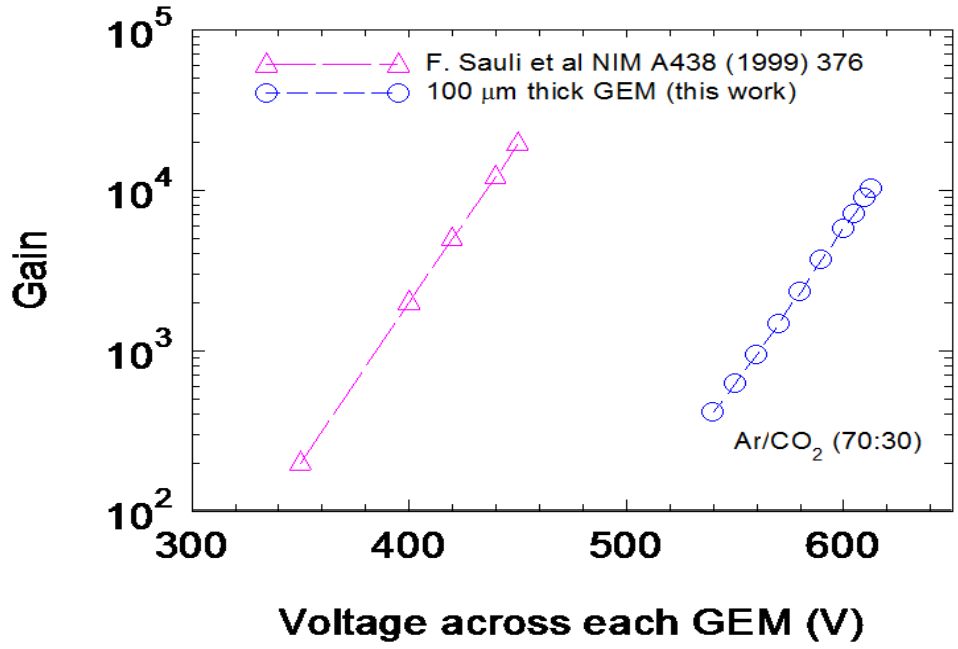

Figure 4.9: Variation of charge gain of the single *(a)* and double *(b)* GEM configurations, as a function of the voltage applied across the GEM holes, ΔV_{GEM}, using Ar(70%)-CO_2(30%).

Figure 4.9 shows the charge gain of the $100\,\mu m$ thick GEM. The charge gains obtained are comparable to those obtained with the $50\,\mu m$ thick GEM in both single and double configurations.

4.2. **Detector Gain and Energy Resolution Mapping**

Prior to the image acquisition with the X-ray tube, the detector was irradiated, point-by-point, using X-rays emitted from a ^{55}Fe radioactive source. Irradiation points were located in a 10×10 matrix (figure 4.10), with a separation of 1 cm between each hole. The source was collimated to 5 mm diameter.

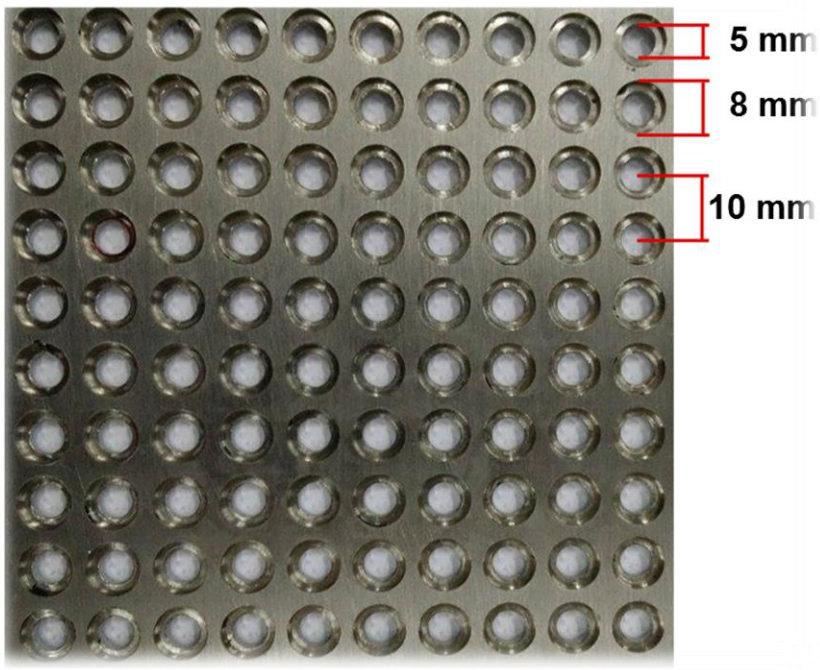

Figure 4.10: Mask that consists of a 10×10 array of 5 mm collimators with a pitch of 10 mm.

For this study the 4 output channels of the 2D resistive electrode readout were interconnected and the resulting avalanche charge was collected by a Canberra 2006 charge sensitive pre-amplifier. The output signal was then fed to a Tennelec TC 243 linear amplifier (4 μs shaping time) and a Nucleus PCA 2 multichannel analyser. The electronic chain sensitivity was calibrated by injection of a known charge into the preamplifier input, following the method described in section 3.2. Figure 4.11 shows the gain and energy resolution distribution over the whole active area of the detector. Maximum gain deviation was recorded at the edges of the detector reaching values of 10 % above the average gain (4100). Energy resolution presented maximum fluctuation of 4.9% with maximum values at the edges of the detector.

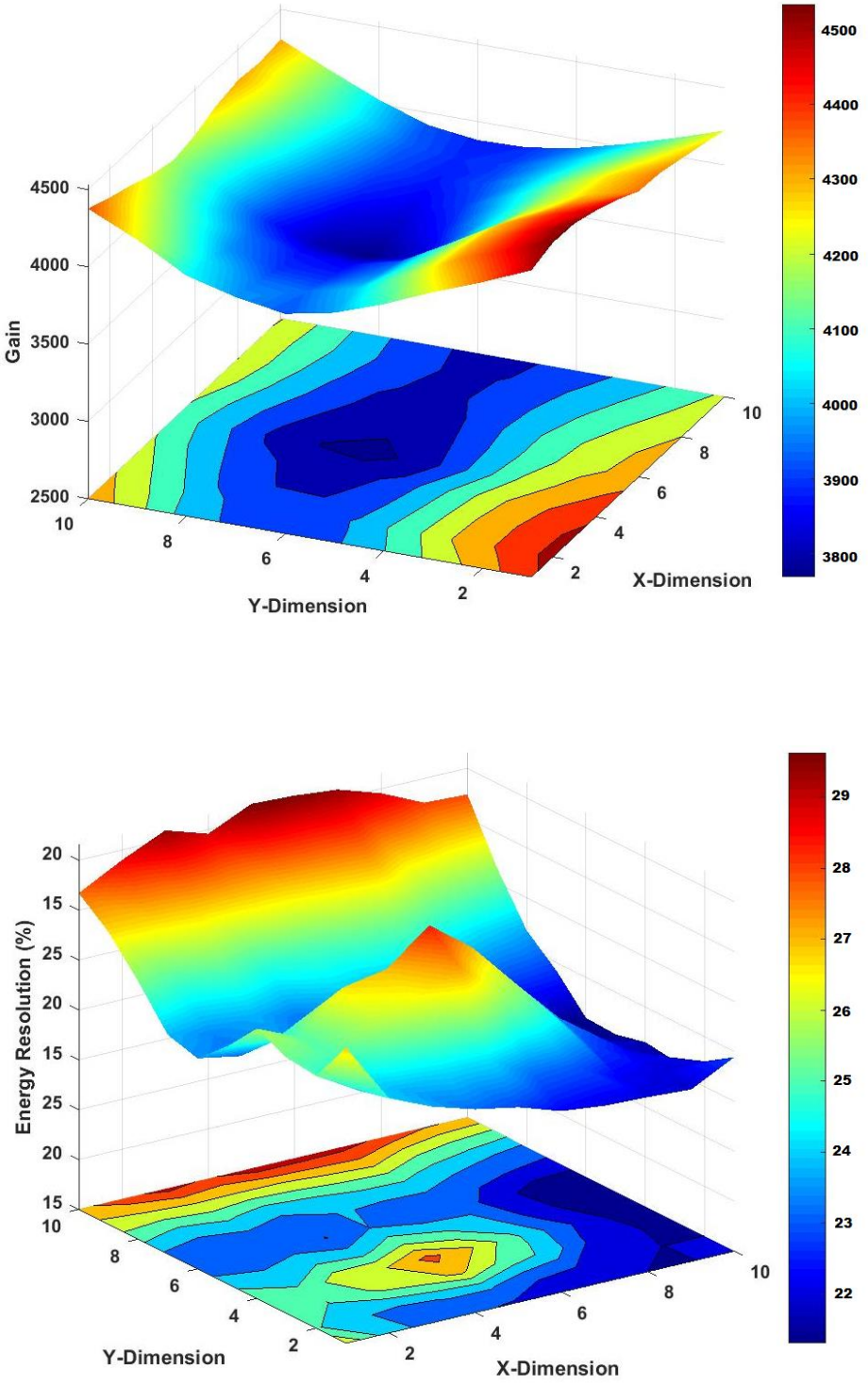

Figure 4.11: Gain and energy resolution map. Detector was irradiated by a ^{55}Fe point source. 100 irradiation points were distributed over a 10 × 10 matrix, covering the entire active surface of our detector. Average gain of 4100 and average energy resolution of 24.4% FWHM was obtained.

The electric field in the drift region, transfer and induction region was $1.44\ \mathrm{kV/cm}$, $3.33\ \mathrm{kV/cm}$ and $1.83\ \mathrm{kV/cm}$, respectively. The voltage difference across both GEMs was $580V$. An average energy resolution of 24.4% and a gain of 4×10^3 were measured, for the $5.9\ keV$ X-rays emitted from the ^{55}Fe radioactive source, over the $100\ cm^2$ of the detector. The high gains recorded at the edges are most likely induced by the resistive lines on the 2D readout: although the 4 output channels were short-circuited, each signal propagated along the resistive line. This effect of higher gains in the edge of the resistive lines is known and increases with the value of the resistance [6]. Events located away from the edges of the active area of the detector suffer more attenuation than the ones at the edges, leading to a slightly lower observable gain.

4.3. $50 \times 50\ mm^2$ VS $100 \times 100\ mm^2$ readout in imaging

One of the main conclusions mentioned in chapter 2 was the breakthrough of micropattern detectors and their intrinsic capabilities as position detectors. Their large area sensitive region made possible to use them as imaging devices by accurately determining the position of the interaction. There are many different possibilities for electronic readout, pulse height analysis and position determination. Most of the imaging applications with MPGDs have made use of discrete channel readout. Very good spatial resolutions, in the order of hundreds of μm for areas as large as $100\ cm^2$, are achieved by this approach. The use of high density electronics should be the optimal solution since each detector element works independently of the others. By doing this, the electronic noise is mitigated, since the capacitance and the output resistance of the detector is reduced, removing undesired RC components from the circuit However, the main drawback of this approach is that it involves the use of a very large number of channels increasing the complexity of the electronic system. When a spatial resolution of only a few mm is required, the electronic system can be simplified by applying the resistive charge division method (see section 3.3.2). Here, the position of the interaction is determined by applying algorithms of the center of mass to the signal amplitudes at each end of the resistive line that interconnects the readout strips. However, this method requires a good signal-to-noise ratio.

As shown in figure 4.1 two different setups were used in this work. Besides the obvious differences in the gaps thickness, the main change was in the readouts used. While the first setup used a resistive readout with an area of $50 \times 50\ mm^2$, the second setup had one with an area of $100 \times 100\ mm^2$. So, in this subsection, both readouts are characterized and their performances compared.

In order to evaluate its performance, the quality of an imaging system must be quantified. The signals from each end of the two resistive lines used for x and y determination were integrated by charge sensitive preamplifiers and digitized using four channels of a CAEN VME Mod. V1724 digitizer. This device has a 100 MHz ADC with 14 bits. The firmware in the FPGA included in the digitizer applies the Jordanov algorithm to the digitized signal from the pre-amplifier [45]. This algorithm shapes the signal in to a trapezoidal form with the height of the flat top proportional to the charge collected in the anode readout. Typical rise and fall times of the trapezoid were set to

$2\mu s$ and the flat top was set to $1\mu s$. This assured a total time of $5\mu s$ μs for each signal, meaning a maximum rate of $200\ KHz$ for the electronic system. This rate was enough for most of the measurements of this work, but can be a possible limitation when a very large area of the detector was irradiated, as will be shown later on. The height of the flat top was measured at 4 different points and the average was recorded for each of the four channels. The position was determined with equation 3.6 by off-line processing software, whenever there were signals from the four channels within a certain time window. The output was a root file with a tree containing raw information of each event and the x, y and E coordinates and some control histograms.

In order to calibrate the detector in position two slits were used. The known distance between them allowed to calculate how many bins corresponded to 1 mm. Figure 4.12 shows the image of two slits with a separation of $7\ mm$ and a width of $1\ mm$, taken with the $100\ \times 100\ mm^2$ readout.

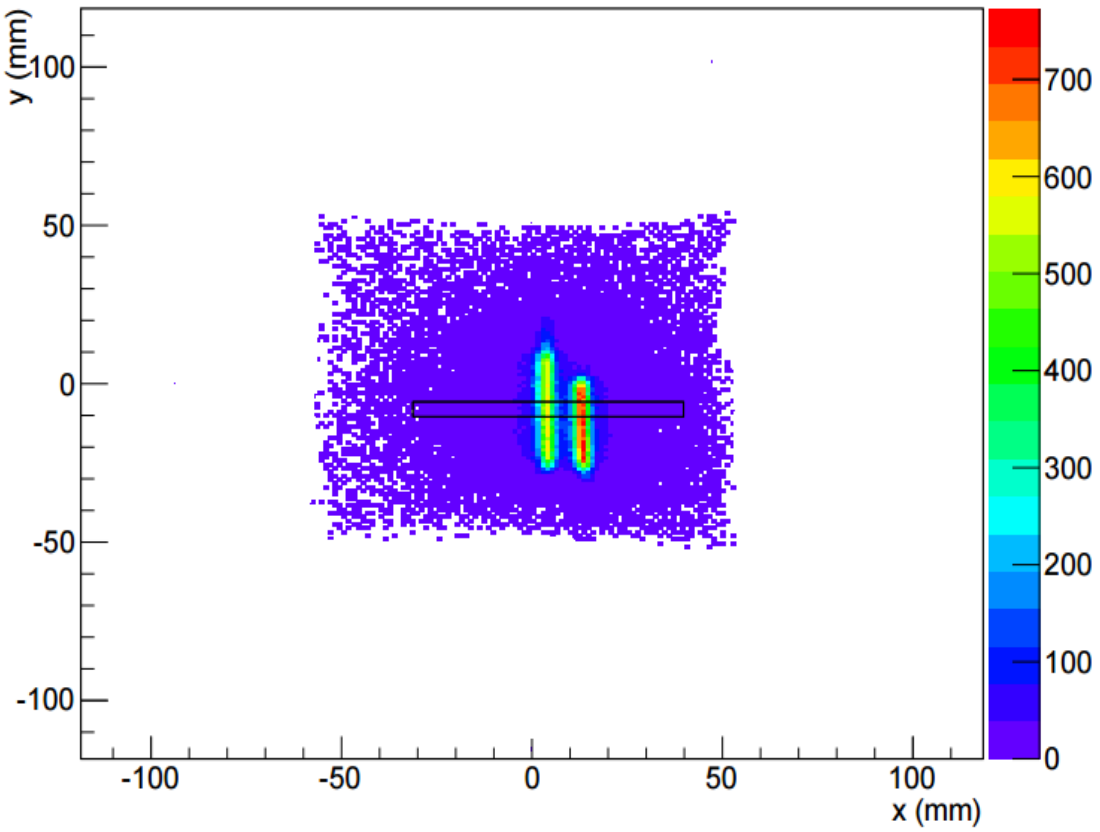

Figure 4.12: Image of two slits with a width of $1\ mm$ and separated by $7\ mm$. The setup depicted in figure 4.1 *b)* was used.

The clarity of information in an image is a measure of how well the image exposes fine features of the object. One way to evaluate this capability is to put two structures close together, usually two infinitely small holes and see how well they can be distinguished in the image. Since in the real world there is no such thing as dimensionless hole, the best approach is the use of slits. The result is a 2D intensity distribution of the photons that passed through the slits and reached the imaging system readout (figure 4.12).

One way to characterize the imaging system is to evaluate the *point spread function* (PSF) of the system at one dimension. For that, a stainless steel mask with a 1 mm wide slit was imaged. This one dimensional approach of the PSF – the *line spread function* (LSF) – is very convenient, because it is easier to image a thin slit than a very small hole. The method described here to determine the position resolution of the system was applied to the two different readouts used. This allows comparing them.

The images acquired with this system are also energy resolved, since for each event three coordinates are stored: the position (x, y) and the X-ray energy (E). The obtained image is a 'colour' X-ray image where the colour represents different X-ray energies. Actually, one of the best features of this system is that it allows selecting different energy regions and showing the image formed only by the events within that energy region. Figure 4.13 shows the energy distribution of the image of the 1 mm slit image strongly attenuated by the 1.5 mm aluminium sheet.

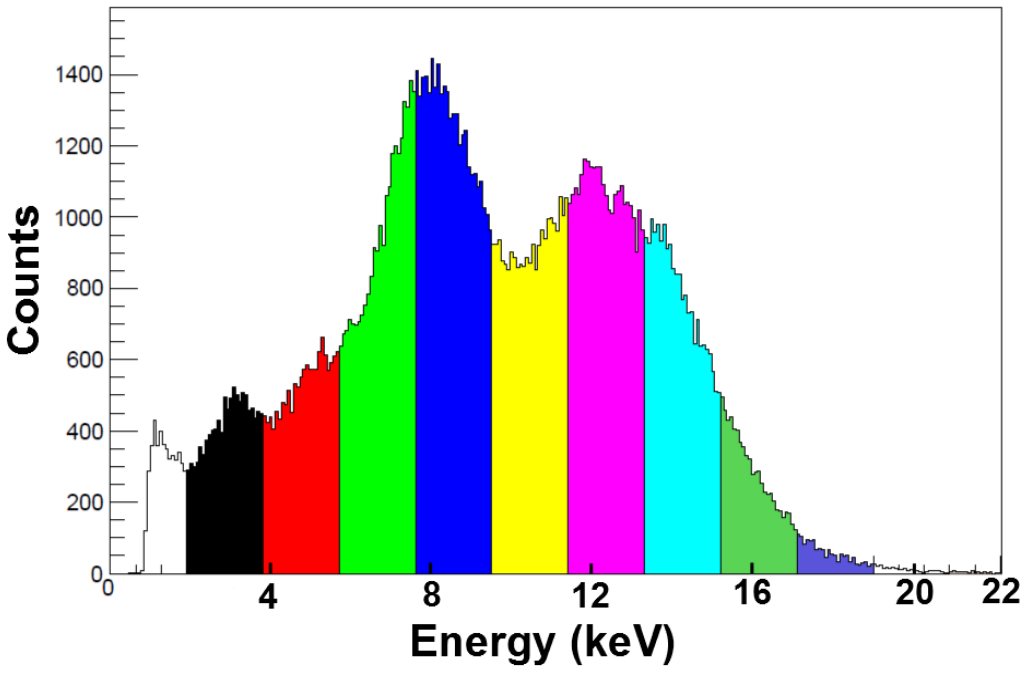

Figure 4.13: Energy spectrum of the image of the $1mm$ slit image. The spectrum is divided in various energy regions, where for each one the position resolution of the correspondent image was calculated. The copper peak is seen at $8\,keV$ being strongly attenuated by the $1.5\,mm$ aluminium sheet.

As it can be seen, different cuts in the energy distribution can applied and an image using only X-rays photons with energy in the selected region can be plotted. Figure 4.14 illustrates the plotted images for each cut done in the energy spectrum of image 4.13.

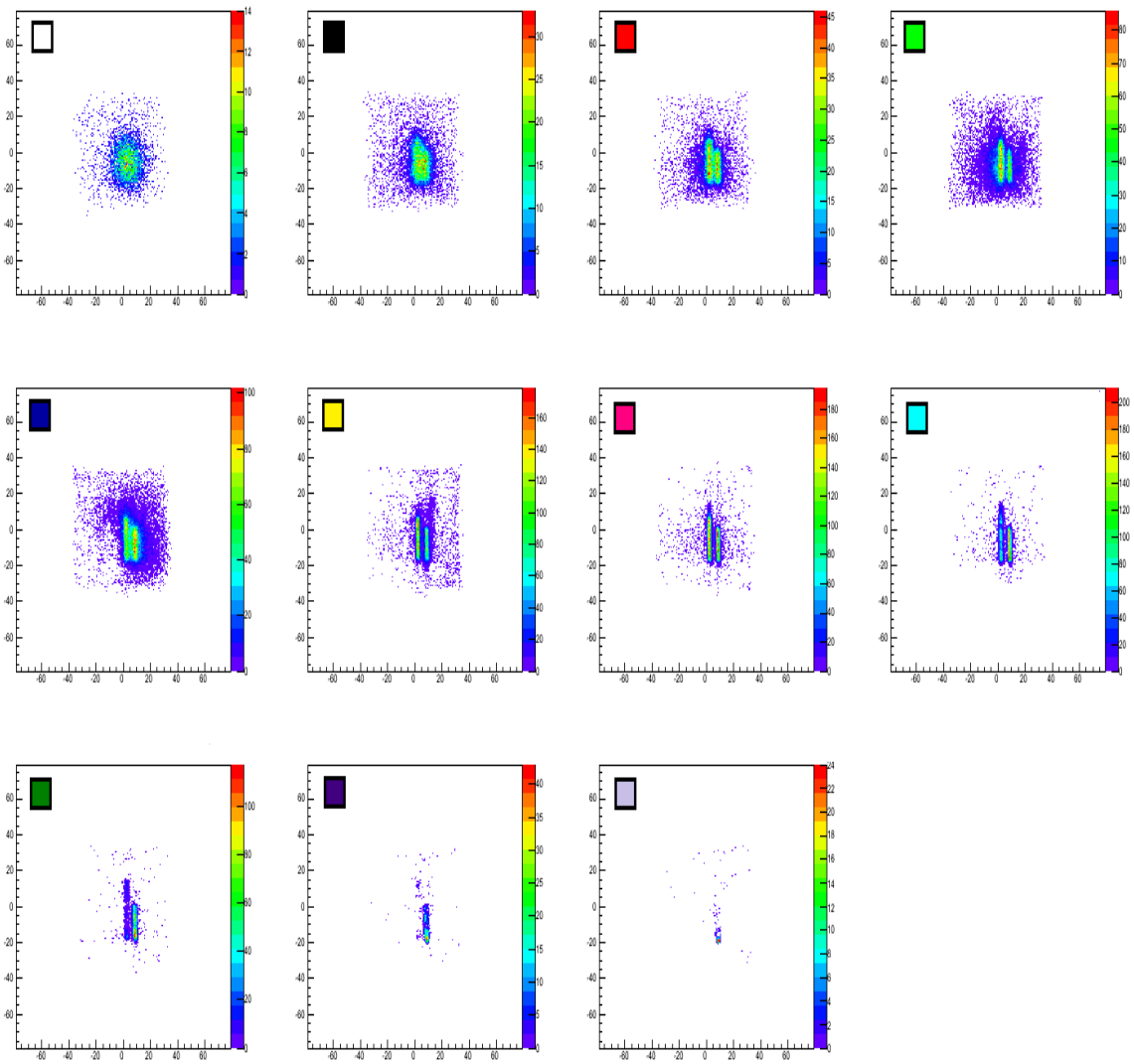

Figure 4.14: Images of the 1mm slit corresponding to each cut indicated in figure 4.13.

Once the images of each energy cut are plotted, the profile of the area delimited by the black rectangle (see figure 4.12) for the different energy is done. Figure 4.15 presents the profile of the images plotted in figure 4.14.

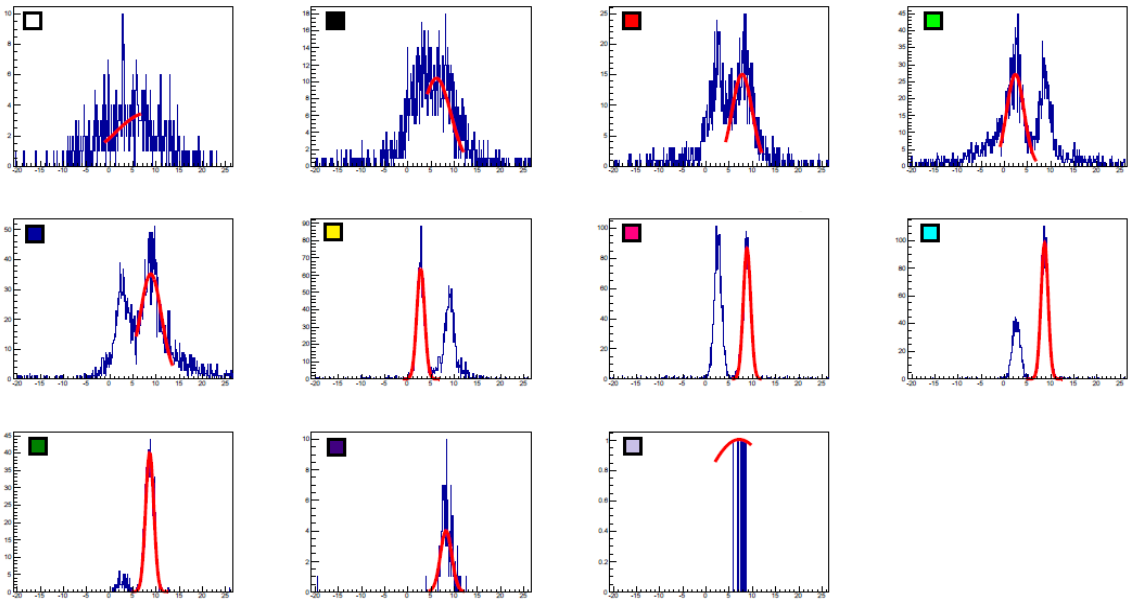

Figure 4.15: Profile of the area defined by the rectangle for each energy cut.

Once the profiles of the slit for each energy cut are plotted, a Gaussian fit can be applied to them to determine their resolution. The width of the imaged slit as function of the energy region is shown in figure 4.16.

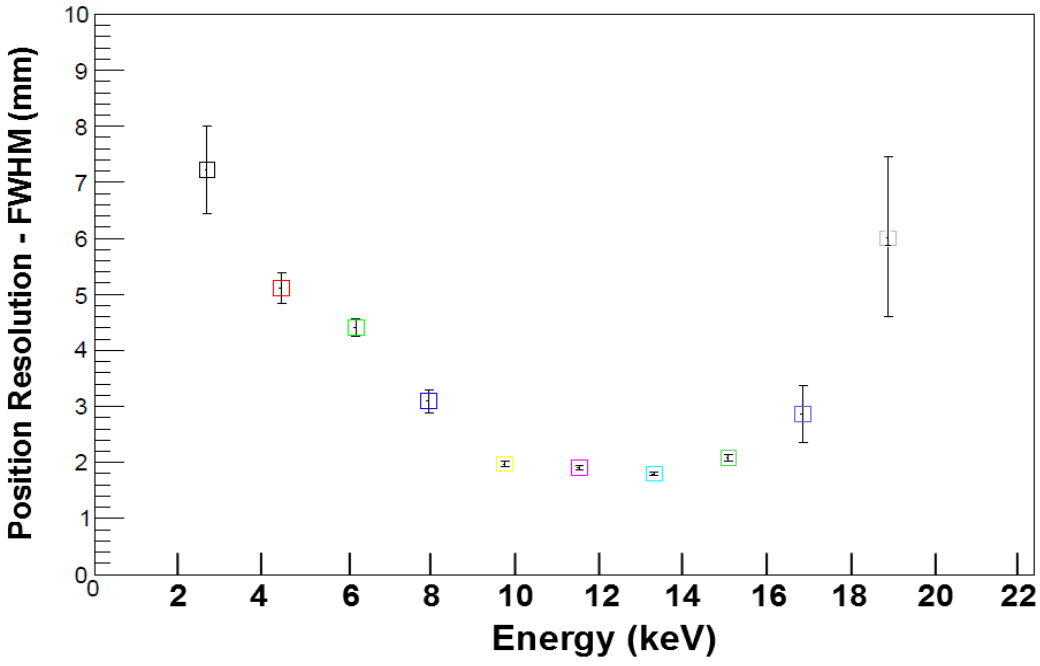

Figure 4.16: Width of the imaged slit as a function of the energy resolution. For the lower energies the lower SNR limits the position resolution. At higher energies is the range of the photoelectrons that limits the position resolution.

The error bars are the standard deviation of the width of the slit, fitted with a Gaussian curve in each line of the image with the width of one pixel/bin. They reflect the statistical fluctuations of the data for each cut. For some ranges of energy the number of events is small, which results in larger statistical variations. This has as consequence less accurate fits. For other ranges of energy the number on events is larger resulting in smaller error bars. The position resolution vs X-ray energy has the expected behaviour since it is in agreement with equation 3.13 for the signal-to-noise ratio at lower X-ray energies and in agreement with the measured photoelectron range for argon shown in figure 3.11 for higher energies.

Figure 4.16 allows to see the point with lowest position resolution, which is labelled with the cyan colour. Finally, a profile of this cut can be plotted and a Gaussian fit can be applied to the data. The profile obtained for the 1 mm slit using the readout $100 \times 100\ mm^2$ is shown in figure 4.17, again in agreement with the expected from fig. 3.11.

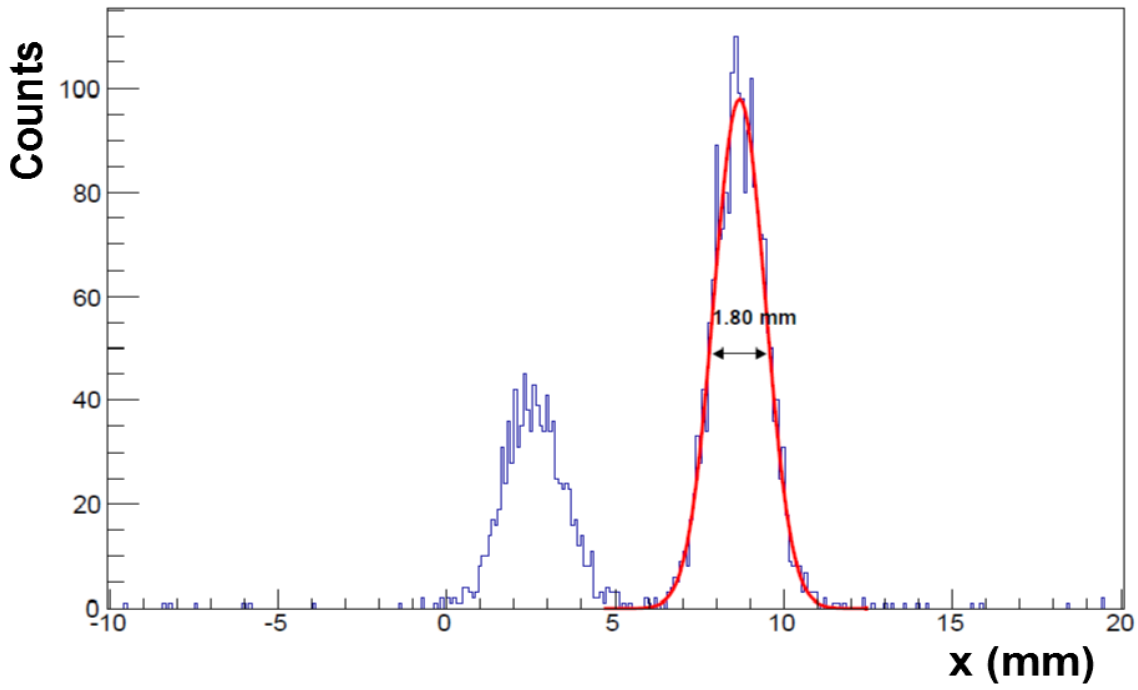

Figure 4.17: Image (1D histogram) of a 1 mm slit. Its width is 1.80 mm and gives an idea of the position resolution of the system. Line spread function obtained with the readout $100 \times 100\ mm^2$ for an energy cut with energies between $\sim 13 - 15\ keV$.

As mentioned in page 76 the figures 4.12 to 4.17 refer to the results obtained with the $100 \times 100\ mm^2$ readout. However, the method is applicable to both readouts. So, applying the same method to the readout $50 \times 50\ mm^2$ the profile of 1 mm slit was also plotted. Figure 4.18 illustrates that profile and respective width.

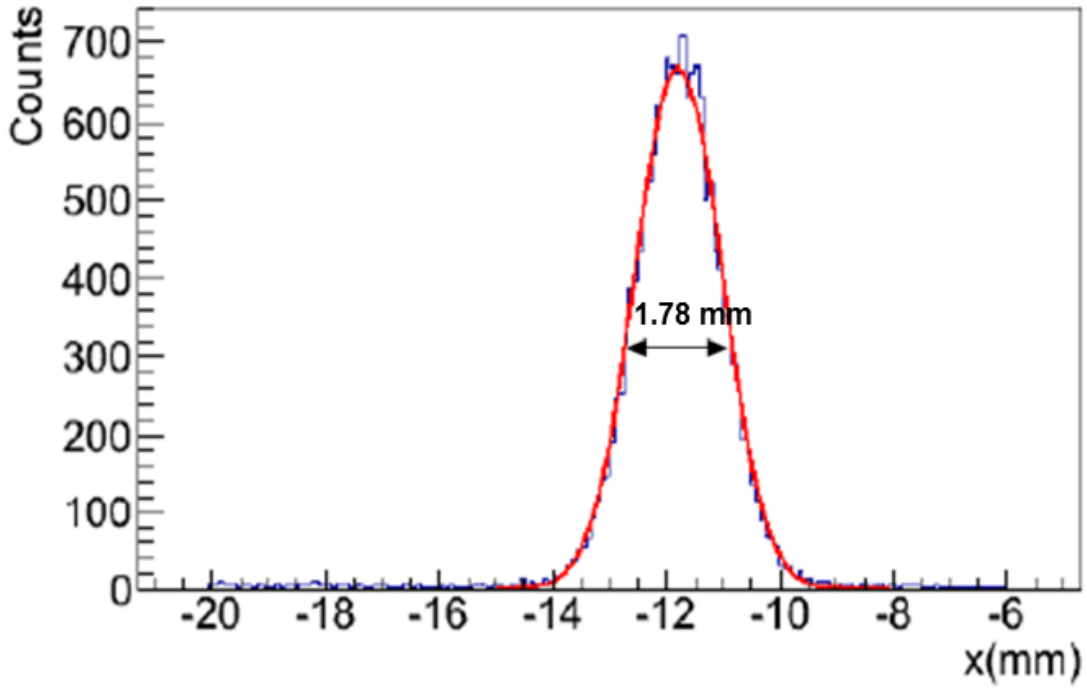

Figure 4.18: Image (1D histogram) of a 1 mm slit. The line spread function of a selected area of the slit gives a distribution with a width of $1.78\ mm$ which gives an idea of the position resolution of the system. Line spread function obtained with the readout $50 \times 50\ mm^2$ for an energy cut with energies between $\sim 13 - 15\ keV$.

The width of the distributions shown in figure 4.17 ($100 \times 100\ mm^2$ readout) and 4.18 ($50 \times 50\ mm^2$ readout) are $1.78\ mm$ (FWHM) and $1.80\ mm$ (FWHM), respectively. Both profiles are the convolution of the LSF of the detector with a rectangle with a width of $1mm$, that would be the projection of the slit. The effect of the Gaussian curve in the distribution becomes more dominant with respect to the rectangle as the width of the slit decreases. In fact, the contribution of the width of the slit to the profiles of figure 4.17 and 4.18 tends to vanish as it becomes narrower, corresponding the width of the distribution to the width of the LSF. The contribution of the width of the slit to the images can be deconvoluted making use of the equation 3.14.

Equation 3.14 must be written again and used since the resolution of the system is of the order of the slit width:

$$\sigma_x = w_s \sqrt[3]{\left(\frac{w_i}{w_s}\right)^3 - 1}$$

For both cases the width of the slit, w_s, was 1 mm and the width of the profiles, w_i, was $1.78\ mm$ and $1.80\ mm$. Applying equation 3.14, the minimum width possible to image with this system is:

$$\begin{cases} \sigma_{x_1} = 1.67\ mm \\ \\ \sigma_{x_2} = 1.69\ mm \end{cases}$$

where the subscript 1 and 2 refers to the setup 1 ($50 \times 50\ mm^2$) and setup 2 ($100 \times 100\ mm^2$) show in figure 4.1.

If the distributions were much wider than the slit, then there would be no need to use equation 3.14 since the resolution would be approximately given by the width of the peak as discussed in section 3.3.3.3. In any case, the difference between the width of the image and the derived with of the LSF is only around 6 %.

Another concept that can be useful to characterize the imaging system is the *edge spread function* (ESF). As described in section 3.3.3.3 the edge response is a method very similar to the line response. The difference is that with the ESF the system responds to a discontinuity (edge) and not to a line as in the LSF. This is other alternative to determine the spatial resolution of the detector. The edge is created by a calliper with an opening of $20\ mm$ (figure 4.19).

Figure 4.19: Calliper with 20 mm aperture used to create an edge.

As in the LSF method, where the gap between the slits served to calibrate the image in position, in the ESF the opening between the tweezers of the calliper helps to perform the calibration. Figure 4.20 illustrate an image of the calliper with an opening of *20 mm* and a rectangle that delimits the zone where a profile of the edge was made. This image was taken with the $50 \times 50\ mm^2$ readout.

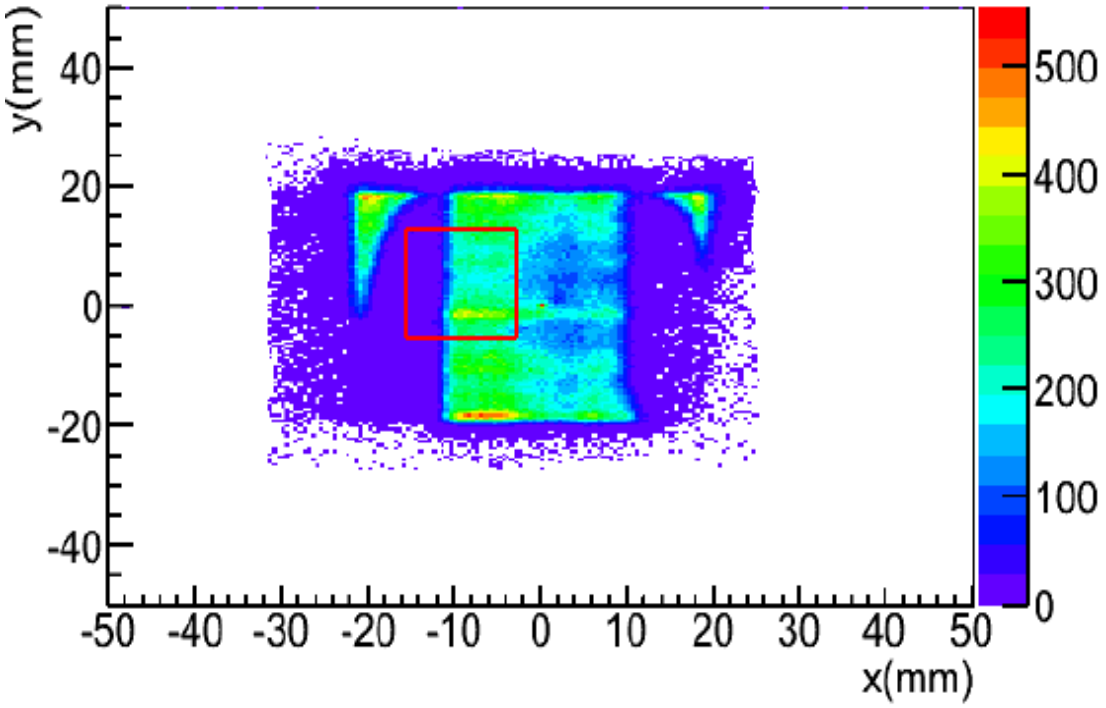

Figure 4.20: Image of a stainless steel calliper with an aperture of *20 mm*, was taken with the $50 \times 50\ mm^2$ readout. The region marked can be used to determine the Edge Spread Function.

In figure 4.20, the edge spread function (ESF) of the region delimited by the red rectangle has enough information to characterize the behaviour of the system.

Once the image is plotted and the rectangle defined, the profile of the delimited region is constructed. Figure 4.21 shows the profile of the edge.

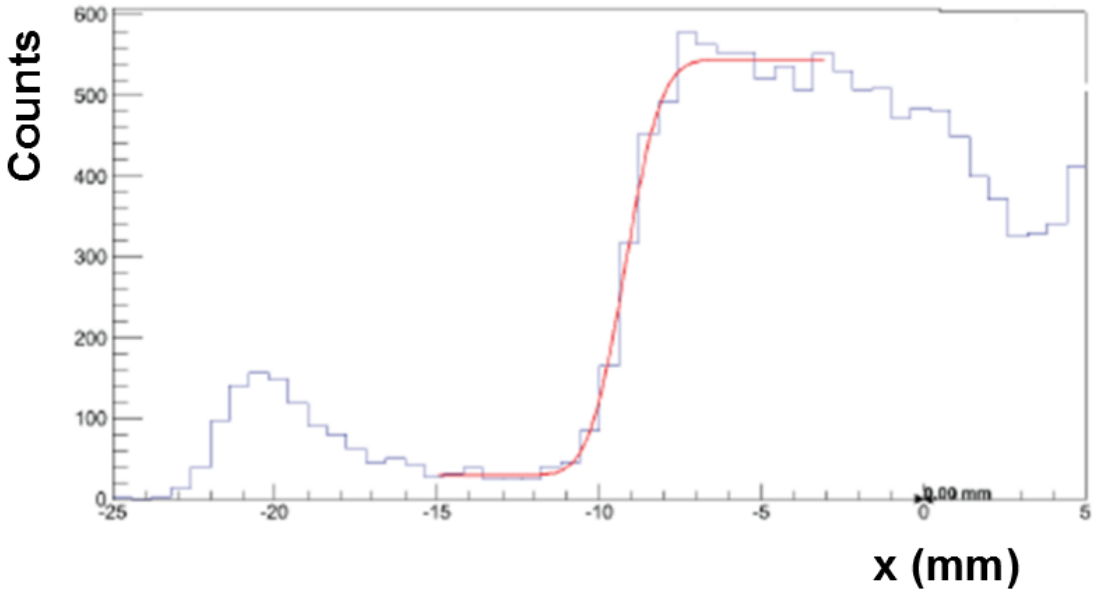

Figure 4.21: Profile of the edge (Edge spread Function) fitted with the Error Function (equation 4.3), which can be seen as the integral of a Gaussian curve.

Figure 4.21 show that the profile of the edge was fitted (red line) with the Error function which is the integral of a Gaussian curve. The Error function is given by the following equation:

$$\operatorname{erf}(x) = \frac{2}{\sqrt{\pi}} \int_0^x e^{-t^2} dt \tag{4.3}$$

By deriving the ESF, one obtains the LSF. The inflection point of the step function corresponds to the centroid of the line spread function. The LSF obtained by differentiating the edge spread function is depicted in Figure 4.22.

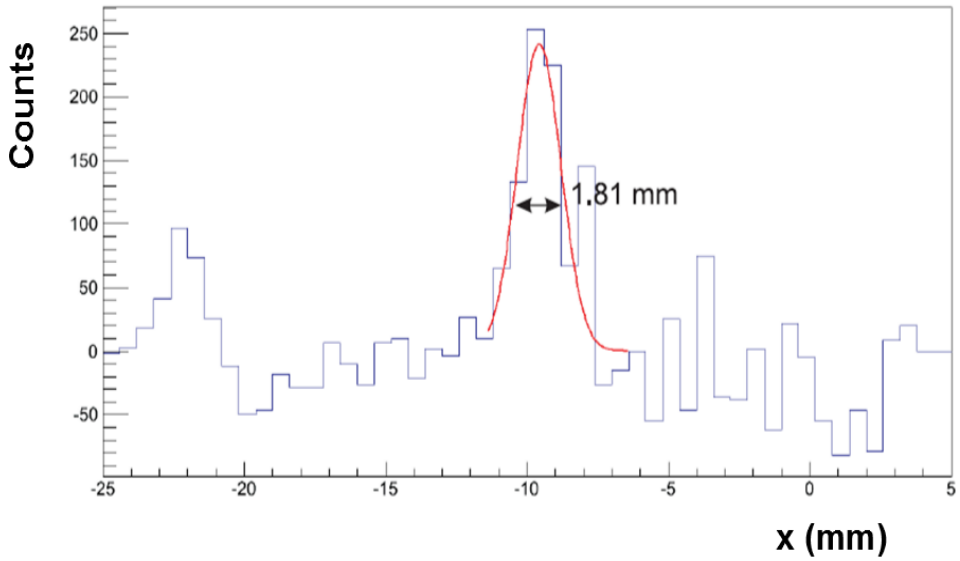

Figure 4.22: Line spread function obtained by the differentiation of the edge spread function. The width of 1.81 mm is the position resolution obtained by fitting a Gaussian curve.

The derivative of the profile (figure 4.22) gives a peak which can be fitted by a Gaussian curve, with a width equal to the position resolution. The *discrete Fourier transform* of the line spread function is the *modulation transfer function* (MTF) and is depicted in figure 4.22. The MTF gives the contrast of the imaging system as a function of the special frequency. If the system has a good resolution, the contrast will be high for higher special frequencies.

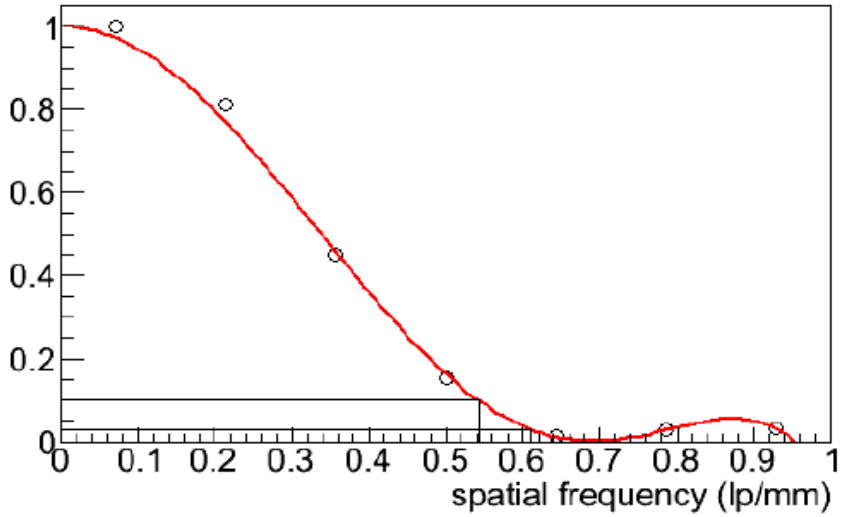

Figure 4.23: Modulation Transfer Function of the edge of figure 4.20. The MTF shows a resolution of 0.54 lp/mm at an amplitude of 10% of the MTF and 0.61 lp/mm an amplitude of 3% of the MTF.

The spatial frequency corresponding to 10 % of the MTF amplitude is around 0.54 lp/mm, which corresponds to two distinguishable slits at 1.85 mm from each other. For the 3% limit of the MTF amplitude, the correspondent spatial frequency is around 0.61 lp/mm, which corresponds to a position resolution to 1.67 mm. The MTF is in agreement with the results found, confirming the relationship between the LSF and MTF as described in section 3.3.3.3.

Once again, these results obtained with the edge response of the system were obtained using the detector setup 1 (see figure 4.1), the one with the $50 \times 50\ mm^2$ readout. The position resolution of 1.81 mm obtained with this method is comparable to the one obtained by the LSF of a $1mm$ slit. The same method was applied to the setup 2 ($100 \times 100\ mm^2$). Again, an image of a stainless steel calliper with an aperture of *20 mm* was taken. Figure 4.24 shows the image of the calliper obtained by irradiating the whole active area of the detector ($10 \times 10\ cm^2$).

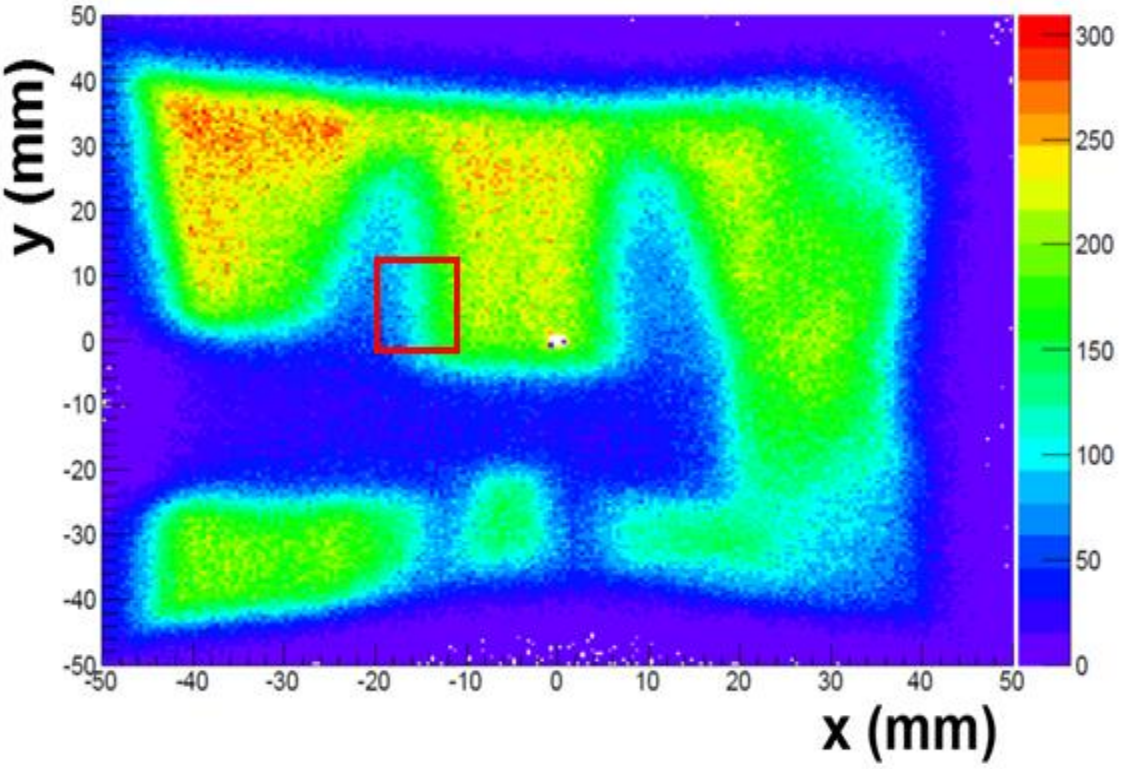

Figure 4.24: Image of a stainless steel calliper with an aperture of *20 mm*. The region marked can be used to determine the Edge Spread Function.

Figure 4.25 shows the respective edge spread function. It is clear that this image has some artifacts that resulted in a poorer definition of the edge of the calliper.

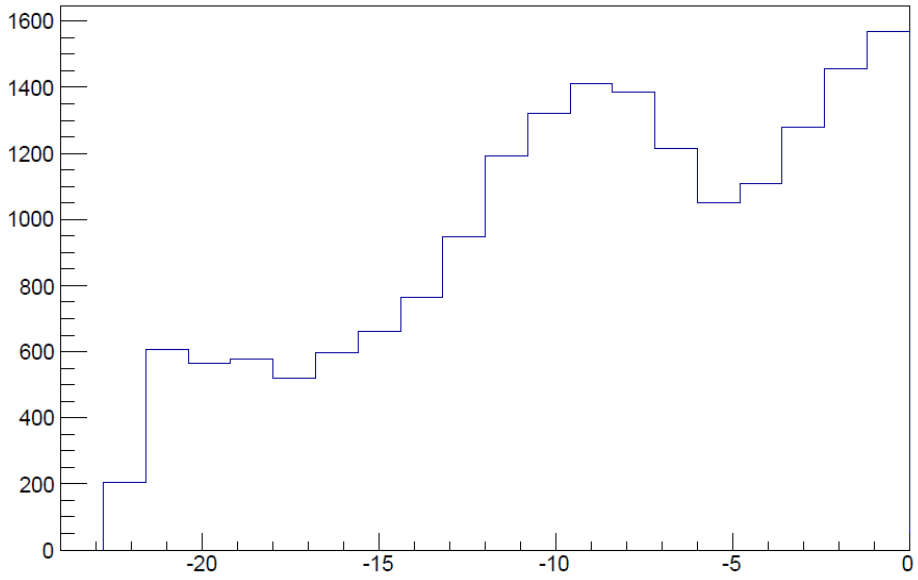

Figure 4.25: Profile of the edge (Edge spread Function).

After calculating the derivative of the ESF, a peak distribution is obtained and its width is the spatial resolution. This result is depicted in the following figure.

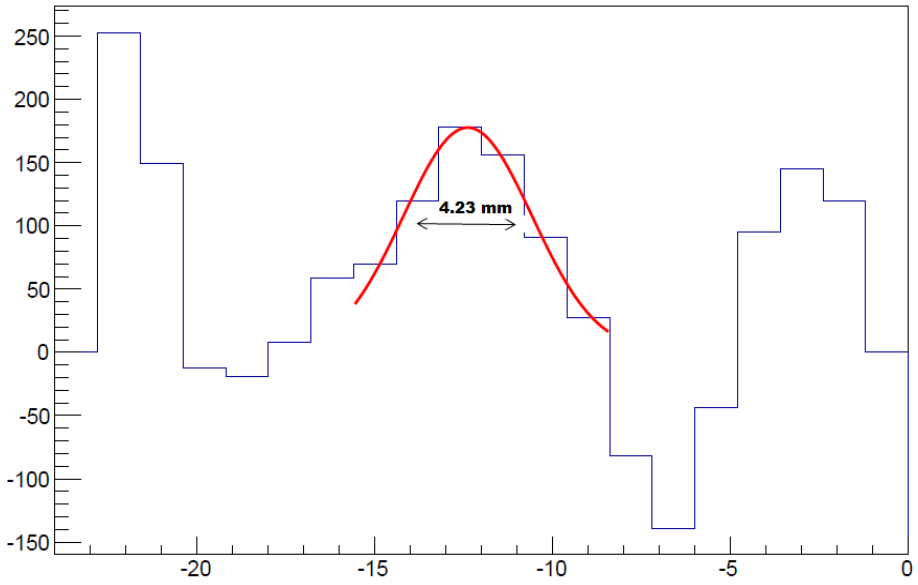

Figure 4.26: Line spread function obtained by the differentiation of the edge spread function. The width of 4.23 mm is the position resolution obtained by fitting a Gaussian curve.

The position resolution obtained with the edge response method for the setup 2 was of 4.23 mm. As it can be seen the profile of the edge in figure 4.25 does not have a well-defined step as the one depicted in figure 4.21. This leads to a broader LSF. The value 4.23 mm for the position resolution is not comparable to the one obtained by the slit method which was 1.80 mm. Therefore, this method cannot be used to determine the position resolution of the system for the second setup.

In this image, around 80% of the total sensitive area of the detector was irradiated. This results in a very high intensity of X-rays entering the detector, increasing the probability of having more than one X-ray entering the detector in the time window needed to discriminate good events, and also leading to some pile up due to the width of the Jordanov trapezoid described in pages 75 and 76. In fact, given the intensity of the X-ray source used in this work (not tunable) the total counting rate in these conditions can be close to 200 kHz. This adds big errors to the determination of the position of an interaction and hence to the step function, leading to a broader peak as depicted in figure 4.26. This pile up is a limitation of the electronics and not of the detector. A possible solution could have been to cover the area surrounding the caliper to keep the counting rate lower, allowing to correctly process all the events.

It has been demonstrated that the possibility of defining energy regions helps to improve the position resolution. For objects with internal structure, this feature can be very helpful, since harder X-rays penetrate denser matter and softer X-rays are transmitted only by softer structures. To test the dynamic range of the imaging system, an articulated wooden dummy (figure 4.27), with a metallic spring inside as "skeleton" was imaged.

Figure 4.27: Wooden dummy that as a metallic spring as "skeleton".

The possibility of using a specific range of energies allows to tune the image contrast. By doing these energy cuts, different parts of the object can be enhanced making possible to distinguish some characteristics of the object among others. Figure 4.28 shows the image delimitated by the red rectangle of figure 4.27.

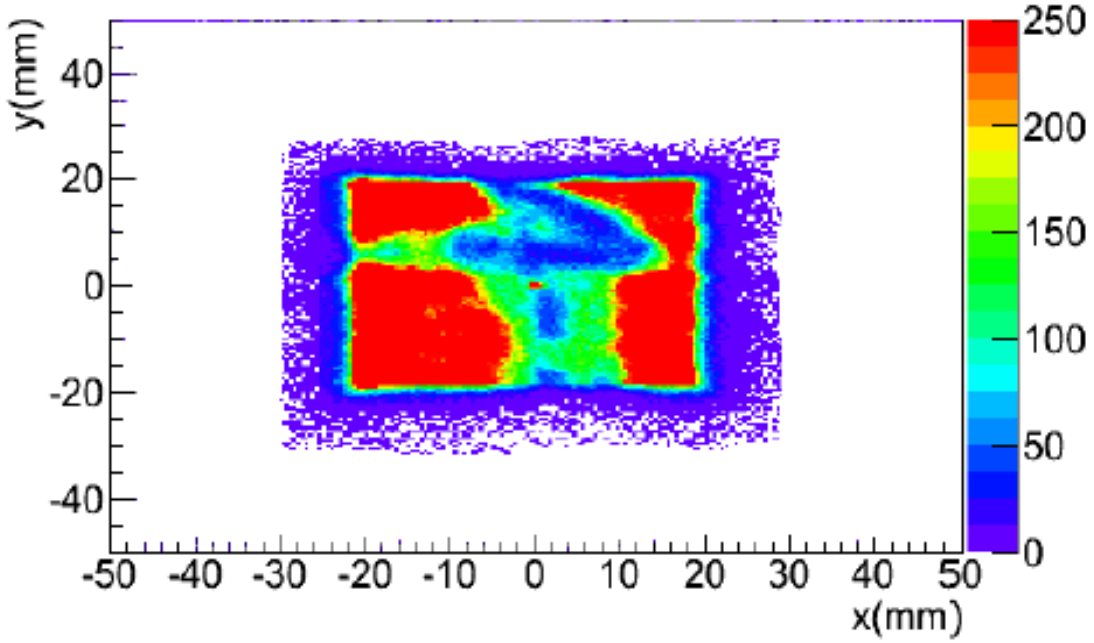

Figure 4.28: Image of the wooden dummy obtained for high energies. Both the wooden body (in tones of green) and the metallic spring (in tones of blue – less X-ray transmission) can be distinguished.

As seen in figure 4.28, both the metallic spring and the dummy's wooden body can be distinguished. The contrast can be changed by selecting different energy ranges. This is one major advantage of this kind of imaging approach, since each X-ray photon has its position recorded as well as its energy. The image of the wooden dummy was obtained by selecting high energies since this range make more suitable to visualise features in the wooden body and at the same time visualise the metallic spring. However, different regions can be selected as needed. Low energies enhance the contrast in the wooden body but losses contrast in the metallic spring. High energies are more suitable to visualize features in the "skeleton" while the contrast of the wooden body is poorer.

The wooden dummy can be compared to a person and an analogy can be done. Lower energies it will make possible to enhance soft tissue like flesh and skin and higher energies will enhance the bones.

As it has been said throughout this section, the signal-to-noise ratio is the most important limitation to the position resolution of the system for lower energies. Accordingly to equation 3.13, the position resolution improves for a higher signal-to-noise ratio. To obtain a good signal-to-noise ratio the GEMs must operate at the highest gains possible, eventually too close to the discharge limit. In a situation where the GEMs are operated at the highest gains possible, the signal-to-noise ratio would be very high and then the position resolution would be limited only by the gas itself or more precisely by the range of the photoelectrons. However, this situation was not achieved since the operation at such regimes increase the probability of discharges and therefore can result in permanent damage of the detector.

Figure 4.16 has shown the behavior of the position resolution as function of the X-ray energy which gives the idea of the performance of the imaging system. The curve is in agreement with expected limitations due to the SNR for low energies and due to the range of the photoelectron in the gas for higher energies. Once the spatial resolution of the imaging system is characterized it is important to understand how the image of the object is distorted when compared with the object. This is other factor that is important in the characterization of the performance of the detector. The distances in the image should be proportional to the distances in the object, at least for an ideal imaging system. However, in systems as the one used in this work the proportionality constant is not the same through the entire image. Figure 4.29 strongly illustrates that phenomenon. This artifact is related to the resistivity used in the resistive charge division. It has been shown in another work [6] that a higher resistance of the resistive lines results in better position resolution, but also in higher differences in the amplitude of the signal in the center of the resistive line and the edges (section 2.2 of [6]). Besides the real difference in signal amplitudes, the fact that the rise time of the charge signal at one edge becomes longer in the opposite charge sensitive preamplifier implies different shaping constants when building the Jordanov trapezoid, also leading to a systematic error in the reconstruction of the image, dependent on the position of interaction.

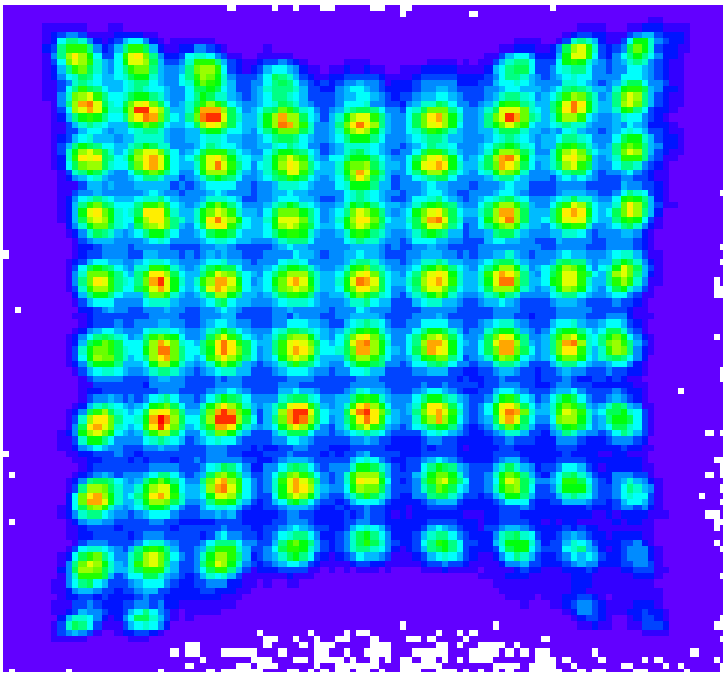

Figure 4.29: Image of the 10×10 mask depicted in figure 4.10. Distortions are visible at the borders (pincushion distortion).

Other factors that can influence the performance of the imaging system are *nonuniformities of the resistive line* and the *boarder distortions*.

The thickness of the resistive strip as well as its width does not always have the same value through all the strip length. This means that the resistance is not the same and local distortions in the image appear. These artifacts were not studied in this work. Both factors may explain the pincushion distortion illustrated in figure 4.29.

5. Conclusions

The purpose of this work was to evaluate the performance of an imaging system for X-ray detection based in a double GEM configuration. The non-standard GEMs used are made from a 100 μm thick Kapton™ foil (2-fold thicker than standard GEM's). The 100 micron thick GEM is produced using the same etching technique as the standard GEM. They already proven to be immune to the damage caused by discharges which opened the possibility of building a robust detector that can safely operate at the high gains necessary to achieve an adequate signal-to-noise ratio for imaging applications using the charge division method The fact that a higher frequency of discharges is supported by the detector without damaging it, allowed to operate at gains close to the sparking limit, helping to achieve better results.

The method of charge division was used and allowed to study the imaging capabilities of the detector. The potentialities of this method were investigated in order to obtain a two dimensional position of the ionization event. Only four charge readout channels, two for each spatial dimension, were needed allowing the use of more cost effective electronics. Two different 2D charge readouts were used: one with an area of $50 \times 50\, mm^2$ and the other one with $100 \times 100\, mm^2$. Both are made of two sets of orthogonal strips with a resistive layer in between. The area of the strips is adjusted so that the signal induced in each set of strips is similar. A resistive line connects each set of strips. The interaction position can be derived from the difference between the signal amplitude collected at each end of the resistive lines.

The performance of the detector and of the imaging system was tested with X-rays in a mixture of argon (70 %) and carbon dioxide (30%) at 1 bar. The position resolution obtained with argon and CO_2 was of $1.78\, mm$ for an active area of $50 \times 50\, mm^2$ and of $1.80\, mm$ for the $100 \times 100\, mm^2$ readout. The position resolutions achieved are in agreement with the expected range of the photoelectrons in argon mixtures for $10\, keV$ X-rays. In order to improve the position resolution, developments for reduction of the signal-to-noise ratio are ongoing, which will allow to use the lower energies of the spectrum (< 8 keV). Although the noise cannot be reduced *ad infinitum* due to the use of resistive charge division, there is still room for improvements, by better matching of the input capacitances of the charge sensitive preamplifiers.

6. References

[1] Bachmann, S. Kappler, B. Ketzer, Th. Muller, L. Ropelewski, F. Sauli, E. Schulte, *High rate X-ray imaging using multi-GEM detectors with a novel readout design*, Nucl. Instr. Meth. A 478 (2002) 104.

[2] Hugo Natal da Luz, Carlos A. B. Oliveira, Carlos D. R. Azevedo, Jamil A. Mir, Rui de Oliveira, Joaquim M. F. dos Santos, and João F. C. A. Veloso, *Single Photon Counting X-Ray Imaging System Using a Micro Hole and Strip Plate*, IEEE Trans. Nucl. Sci **55** (2008) 2341.

[3] W. C. Röntgen. Über eine neue art von strahlen. In *Aus den Sitzungsberichten der Würzburger Physik.-medic*. Gesellschaft Würzburg, pages 137 – 147, 1895. Translation into Portuguese: A. C. P. Carvalho, *Sobre uma nova espécie de raios*, Rev. Imagem, 27(4):287 – 293, 2005.

[4] G.F. Knoll, *Radiation Detection and Measurement*, John Wiley and Sons, Third Edition, Michigan U.S.A., 2010.

[5] A. Einstein. *Über einen diw erzeugung and verwandlung des litches betreffenden heuristischen gesichtspunkt*. Ann. Phys., 17:132 – 148, 1905. Translation into English: *Concerning an Heuristic Point of View Toward the Emission and Transformation of Light*, Am. J. Phys., 33 n. 5, 1965.

[6] Hugo Natal da Luz, *"Development of neutron and X-ray imaging detectors based on MHSP"*, Dissertação de Doutoramento, Departamento de Física da Universidade de Aveiro, 2009.

[7] H. Bethe. *Zur Theorie des Durchgangs schneller Korpuskularstrahlen durch Materie*. Annalen der Physik, 397:325 – 400, 1930.

[8] Eugenio Nappi and Vladimir Peskov, *Imaging Gaseous Detectors and Their Applications*, Wiley-VCH., 2013.

[9] G. Charpak, G. et al, *The use of multiwire proportional counters to select and localize charged particle*. Nucl. Instr. Methods, 62(3):262 – 268, 1968.

[10] H. Geiger and W. Müller. Elektronenzählrohr zur Messung schwächster Aktivitäten. *Naturwissenschaften*, 16(31):617, 1928. Doi:10.1007/BF01494093.

[11] C.A.N. Conde and A.J.P.L. Policarpo, *A gas proportional scintillation counter*, Nucl. Instrum. Meth. 53 (1967) 7. doi:10.1016/0029-554X(67)91323-7.

[12] H. Natal da Luz, J. F. C. A. Veloso, J. M. F. dos Santos, C. A. N. Conde, R. M. C. Silva, Pan H.-R., Lin H.-A., and Li Z.Y. *A large area gas proportional scintillation counter for solar X-ray spectrometry with a balloon born experiment*. IEEE Trans. Nucl. Sci., 49:2488 – 2491, 2002.

[13] J. E. Bateman, M. W. Waters, and R. E. Jones. *Spatial Resolution in a xenon filled MWPC X-ray imaging detector – a computing physics approach*. Nucl. Instr. Meth., 135:235 – 249, 1976.

[14] G. C. Smith, J. Fischer, and V. Radeka. *Photoelectron range limitations to the special-resolution for X-Rays in gas proportional chambers*. IWW Trans. Nucl. Sci., 31(1):111 – 115, 1984.

[15] A. Oed. *Micro pattern structures for gas detectors*, Nuclear Instruments and Methods in Physics Research A, 471:109 – 114, 2001.

[16] A. Oed. Position-sensitive detector with microstrip anode for electron multiplication with gases. Nucl. Instr. Meth. A, 263:351 – 359, 1988.

[17] J. E. Bateman, J.F. Connolly, A.B. Lodge, R. Stephenson, R. Mutikainen, I. Suni, and J. Morse. A gas microstrip detector for X-ray imaging with readout of the anode by resistive division. Nucl. Instr. Meth. A, 477:29 – 36, 2002.

[18] F. Sauli. *Micro pattern gas detectors*. Nucl. Instr. Meth. A, 477:1 – 7, 2002.

[19] F. Ortuño-Prados and C. Budtz-Jorgensen. *The electron-conducting glass SCHOTT S8900 as substrata for microstrip gas chamber*. Nucl. Instr. Meth. A, 364(2):287 – 289, 1995.

[20] Y. Giomataris, Ph. Rebougeard, J.P. Robert, and G. Charpak. *MICROMEGAS: a high-granularity position-sensitive gaseous detector for high particle-flux environments*. Nucl. Instr. Meth. A, 376(1):29 – 35, 1996.

[21] Y. Giomataris, *Development and prospects of the new gaseous detector – Micromegas*. Nucl. Instr. Meth. A, 419:239 – 250, 1998.

[22] J. P. Cussonneau, M. Labalme, P. Lautridou, L. Luquin, V. Metivier, A. Rahmani, and T. Reposeur. 2D localization using resistive strips associated to the micromegas structure. Nucl. Instr. Meth. A, 492:26 – 34, 2002.

[23] F. Sauli. *GEM: a new concept for electron amplification in gas detectors*. Nucl. Instr. Meth. A, 386:531 – 534, 1997.

[24] Gas Detectores Development-CERN. URL: http://gdd.web.cern.ch/GDD/

[25] S. Bachmann, S Kappler, B. Ketzer, Th. Müller, L. Ropelewski, F. Sauli and E. Schulte. *High rate X-ray imaging using multi-GEM detectors with a novel readout design*. Nucl. Instr. Meth. A, 478:104 – 108, 2002.

[26] G. P. Guedes, A. Breskin, R. Chechik, D. Vartsky, D. Bar, A. F. Barbosa, and P. R. B. Marinho. *Two-dimensional GEM imaging detector with delay-line readout*. Nucl. Instr. Meth. A, 513:473 – 483, 2003.

[27] R. Chechik, A. Breskin, C. Shalem, and D. Mörmann. *Thick GEM-like hole multipliers: properties and possible applications.* Nucl. Instr. Meth. A, 535(1-2):303 – 308, 2004.

[28] J. A. Mir, R. Stephenson, N. J. Rhodes, E. M. Schooneveld, J. F. C. A. Veloso, and J. M. F. Dos Santos. *Short induction gap gas electron multiplier (GEM) for X-ray spectroscopy*. Nucl. Instr. Meth. A, 573(1-2):179 – 483, 2007.

[29] J. A. Mir, R. Stephenson, N. J. Rhodes, E. M. Schooneveld, H. Natal da Luz, J. F. C. A. Veloso, and J. M. F. Dos Santos, and C. D. R. Azevedo. *Further studies on the gain properties of a gas electron multiplier with a micro-induction gap amplifying structure (GEM-MIGAS) aimed at low energy X-ray detection*. Nucl. Instr. Meth. A, 580(3):1372 – 1377, 2007.

[30] H. Natal da Luz, J. A. Mir, X. Carvalho and J.M.F. dos Santos. *X-ray imaging with GEMs using* $100\,\mu m$ *thick foils*. Journal of Instrumentation, Volume 9, C06007, JUN 2014.

[31] C. D. R. Azevedo, S. Biagi, R. Veenhof, P.M. Correira, A.L.M. Silva, L.F.N.D. Carramate, J.F.C.A. Veloso. *Position resolution limits in pure noble gaseous detectors for X-ray energies from 1 to 60 keV*. Physics Letters B 741:272-275, 2015.

[32] William R. Hendee and E. Russel Ritenour, *Medical Imaging Physics*, John Wiley and Sons, Fourth Edition, Michigan U.S.A., 2002.

[33] J. T. Bushberg, J. A. Seibert, Jr. E. M. Leidholdt, and J. M. Boone. *The essential Physics of medical imaging*. Lippincott Williams & Wilkins, 2002.

[34] *Radiation oncology physics: a handbook for teachers and students*, International Atomic Energy, Vienna, 2005.

[35] J. P. Cussonneau, M. Labalme, P. Lautridou, L. Luquin, V. Metivier, A. Rahmani, and T. Reposeur. *2D localization using resistive strips associated to the micromegas structure.* Nucl. Instr. Meth. A, 376(1):26-34, 2002.

[36] G. C. Smith, J. Fischer, and V. Radeka. *Photoelectron range limitations to the spatial-resolution for X-rays in gas proportional chambers*. IEEE Trans. Nucl. Sci., 31 (1):111-115, 1984.

[37] J. Fisher, V. Radeka, and G. C. Smith. *X-ray position detection in the region of 6 μm rms with wire proportional chambers*. Nucl. Instr. Meth. A, 252(2-3):239-245, 1986.

[38] Steven W. Smith. *The Scientist and Engineer's Guide to Digital Signal Processing*. California Technical Publishing, 2006.

[39] H. Klein, H. Brede, and B. R. L. Siebert. *Energy and angle straggling effects in a D(d,n)^{3}He neutron source using a gas target*. Nucl. Instr. Meth., 193:635-644, 1982.

[40] Bracewell, Ron N., *The Fourier Transform and Its Applications*. New York: McGrawHill Book Company, 1965.

[41] R. Bouclier, W. Dominik, M. Hoch, J.C. Labbé, G. Million, L. Ropelewski, F. Sauli, A. Sharma, and G. Manzin, *New Observations with the Gas Electron Multiplier (GEM)*, Nucl. Instr. and Meth. A396 (1997) 50.

[42] S. Bachmann, A. Bressan, L. Ropelewski, F. Sauli, *Operating Properties of Detectors based on GEM*. URL: https://gdd.web.cern.ch/GDD/publications.res/mpgd99a.pdf.

[43] J.A. Mir, G.E. Derbyshire, R. Stephenson, N.J. Rhodes, E.M. Schooneveld, J.F.C.A. Veloso, J.M.F. Dos Santos, N. Spooner, T.B. Lawson, P.K. Lightfoot, *Operational Characteristics of a GEM-MSGC System for X-ray Detection*, IEEE Trans. Nucl. Sci. 52 (2005) 2927.

[44] S. Bachmann, A. Bressan, L. Ropelewski, F. Sauli, A. Sharma, D. Mörmann, *Charge amplification and transfer processes in the gas electron multiplier*, Nucl. Instr. and Meth. A 438 (1999) 376-408.

[45] Technical Information Manual Rev.28 CAEN VME model V1724.